FLUX-WEAKENING CONTROL FOR PERMANENT-MAGNET

SYNCHRONOUS MOTORS BASED

ON Z-SOURCE INVERTERS

by

Muyang Li, B.S.

ABSTRACT
FLUX-WEAKENING CONTROL FOR PERMANENT-MAGNET
SYNCHRONOUS MOTORS BASED
ON Z-SOURCE INVERTERS

Muyang Li

Marquette University, 2014

Permanent magnet synchronous machines (PMSMs) have high efficiency, high power density, high torque-to-inertia ratio, and fast dynamic response. These features make this kind of machines very attractive for electric vehicle (EV) applications. However, because of their nature, i.e., constant magnet flux provided by magnets, these machines have a narrow constant power speed range (CPSR). This limitation is a strong drawback for application of PMSMs in electric vehicles, where high speed is the top requirement. Two different approaches can extend the maximum speed under constant power: (1) Increasing a drive's output voltage, and (2) implementing flux-weakening (FW) control methods. However, a conventional drive's output voltage is limited by its dc bus. Furthermore, FW control methods are constrained by the maximum output voltage of a drive. In this work, a new approach is demonstrated to obtain a wider CPSR range by implementing a Z-source inverter as a motor-drive. Such a Z-source inverter can provide highly boosted voltage and is immune to dead time and shoot through issues. In addition, in this thesis, a constant power FW control algorithm is developed and simulated for this new approach.

In order to state the research objective of this thesis, a basic background is presented at the beginning. Then, the mathematical models of PMSMs are deduced, where the motor model in a d-q frame is a foundation of the vector control method. With the purpose of increasing the CPSR, it is necessary to give a thorough analysis about the control principles of PMSMs for different operation conditions. Initially, the maximum torque per ampere (MTPA) control is described in detail in the constant torque region. Then, the FW control is explained in the constant power region. To simulate the control operations of PMSMs in different regions, a conventional motor-drive system model is presented with its mechanical loads. Meanwhile, a closed-loop control, which implements MTPA control at low speeds and FW control at high speeds, is implemented to operate the conventional inverter in the motor-drive system.

As recommended in many previous investigations, Z-source inverters are selected to replace conventional inverters for higher output voltages. Hence, Z-source inverters are investigated and simulated here with special control methods. In order to replace a conventional inverter in a motor-drive system, a novel control algorithm is developed to control boost voltage operation of Z-source inverters. A new motor-drive system, which implemented a Z-source inverter, is simulated with closed-loop MTPA and FW control. Comparison between the two control methods shows that a wider CPSR and better performance can be obtained by utilizing Z-source inverters

ACKNOWLEDGMENTS

Muyang Li

TABLE OF CONTENTS

LIST OF TABLES

LIST OF FIGURES

LIST OF ACRONYMS

IPMSM	Interior Permanent Magnet Synchronous Machine
PMSM	Permanent Magnet Synchronous Machine
PM	Permanent-Magnet
EV	Electric Vehicle
MTPA	Maximum Torque per Ampere
FW	Flux-Weakening
SPWM	Sinusoidal Pulse Width Modulation
SVPWM	Space Vector Pulse Width Modulation
CPSR	Constant Power Speed Range
ZSI	Z-Source Inverter
qZSI	Quasi-Z-Source Inverter
PWM	Pulse Width Modulation
MMF	Magneto-Motive Force
IPM	Interior Mounted Permanent Magnet
SPM	Surface Mounted Permanent Magnet
DTC	Direct Torque Control
FOC	Field Oriented Control
MTPA	Maximum Torque per Ampere
Back-EMF	Back-Electromotive Force
CVCP	Constant Voltage Constant Power
CCCP	Constant Current Constant Power
VCLMT	Voltage and Current Limited Maximum Torque
VSI	Voltage Source Inverter
CSI	Current Source Inverter
BVFW	Boosted-Voltage Flux-Weakening

Chapter 1

Introduction

1.1 Background of the Problem

For the last couple of decades, interior permanent magnet synchronous machines (IPMSMs) have attracted great attention in various industry applications, particularly for the electric vehicle (EV) propulsion systems. The reasons for IPMSMs' attractiveness stem from their high power density, high efficiency, wide speed range, fast torque-speed response, and decreasing price of permanent-magnet (PM) materials [1, 2]. For traction and residential drive applications, such as EVs, machines tools, and washing machines, IPMSM-drive systems normally require wide speed range as well as high efficiency and high torque to inertia ratio, especially at low speeds [3, 4]. Research on drives controlling permanent-magnet synchronous motors (PMSMs) for use in the aforementioned applications has become more and more common in recent publications [5-10].

In order to obtain satisfactory motor performance under various conditions, many studies about control strategies have been reported in the literature. One high efficiency control strategy, the maximum torque per ampere (MTPA) control [11], is widely used in industry application for its high torque output, efficient utilization of the dc bus, and minimization of copper losses. For the high speed operations in IPMSM-drives, it is necessary to have the flux-weakening (FW) control which increases a motor's speed range by reducing the flux density and flux in its air-gap [12]. For traction applications in Evs, IPMSM-drives are designed to provide a constant drive torque up to a base speed and then to provide torque which is inversely proportional to speed up to a maximum speed as shown in Figure 1.1 [13]. In the other words, IPMSM-drives are controlled by a MTPA method at low speeds and a FW method at high speeds.

$$CPSR = \frac{\omega_{max}}{\omega_{base}}$$
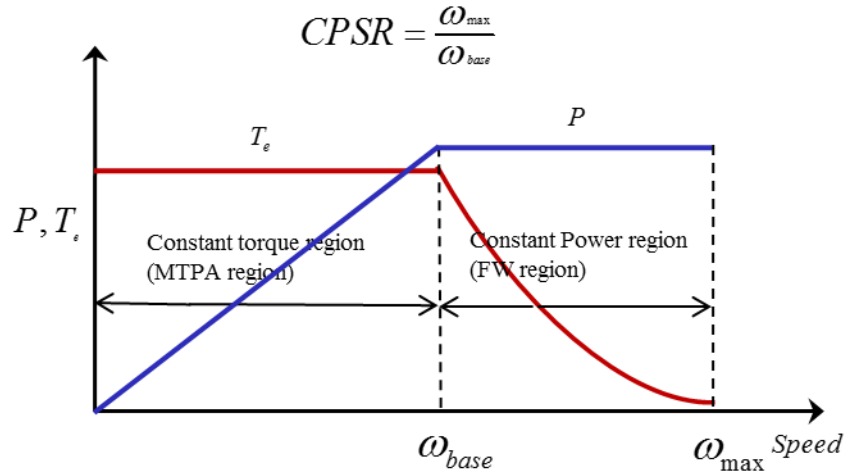
Figure 1.1: Typical characteristic curves of torque/power vs. speed of IPMSMs.

In practical applications, most drives for electric automobiles, trains, and buses require a wide constant power speed range (CPSR) as shown in Figure 1.1, which is widely used to evaluate an EV's performance. Thus, it is of great significance to enhance the FW ability for IPMSMs. The following section outlines the FW control of PMSMs in variable frequency drives, and the approach to improve the FW performance from the inverter side.

1.2 Review of Literature

1.2.1 Control of Permanent Magnet Synchronous Motors

Permanent magnet synchronous motors are brushless motors which use rotating permanent magnets and stationary phase coils. The stator of a poly-phase (or three-phase) PMSM is essentially of the same structure as that of a poly-phase induction motor or a poly-phase synchronous motor. The phase currents produces a rotating magneto-motive force (MMF) in the air gap, whose trajectory is more or less a circle in the d-q frame. However, in the rotors of PMSMs, the PM materials can be mounted on or in a rotor body, to constitute surface-mounted PMs or interior-mounted PMs. For

PM machines, there are five popular PM layouts for the rotors of such machines as shown in Figure 1.2, which include a surface-mounted PM (SPM) machine, (a), an interior-mounted PM (IPM) machine, (b), a permanent-magnet reluctance machine (c), a spoke-type PM machine (d), and a permanent-magnet-assisted synchronous reluctance machine I, [14]. The operation speed range is significantly affected by the saliency ratio of the inductances (L_d / L_q) of the different rotor types. Ultimately, the application determines the viability of a particular machine configuration. In this thesis, the discussion and analysis focuses on the flat-bar IPMs, which are widely used in industry applications.

(a) SPM machine

(b) IPM machine

(c) Permanent-magnet reluctance machine

(d) Spoke-type PM machine

(e) Permanent-magnet assistant synchronous reluctance machine
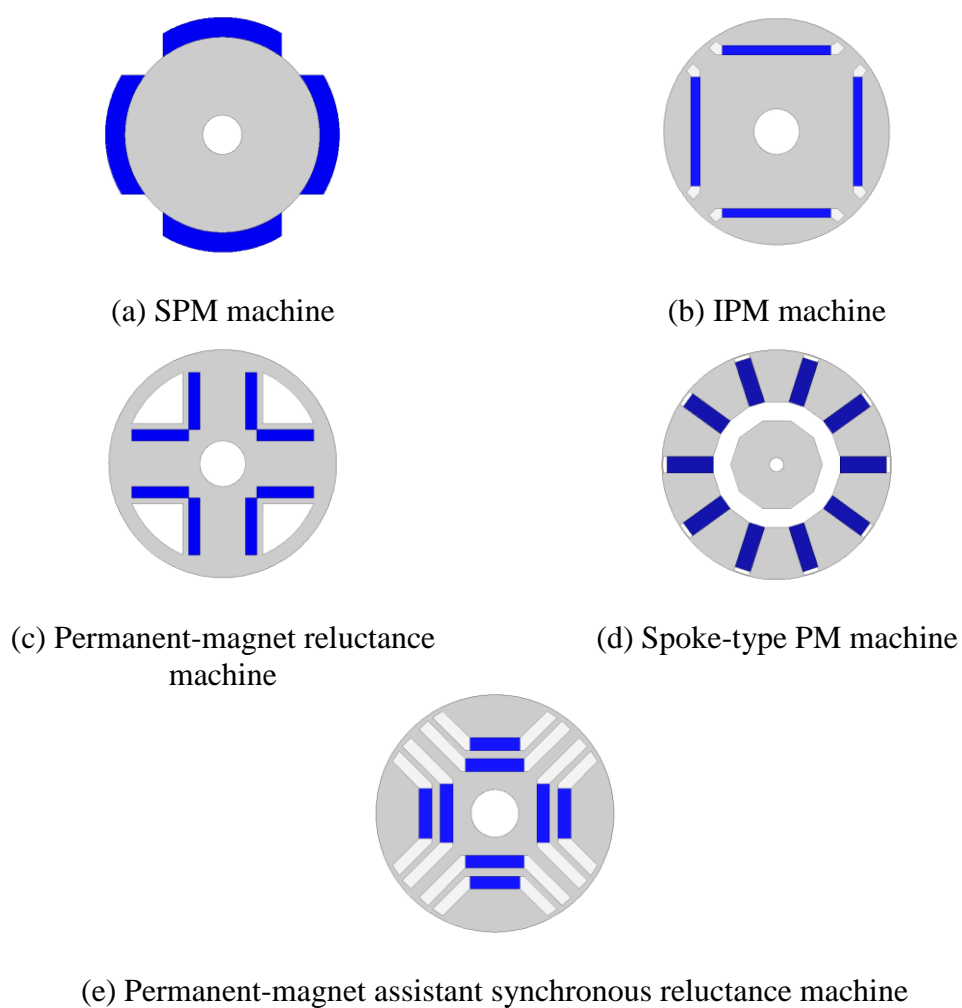
Figure 1.2: Rotor layouts for PM machines.

Generally, there are two types of motor control methods: scalar control and vector control, which have been used to control an induction machine, can also be applied to PMSMs as well [15]. More specifically, in the scalar control and vector control categories, there are three main control algorithms [16]:

- Volts/hertz control, in open loop

- Field oriented control (FOC), in closed loop

- Direct torque control (DTC), in closed loop
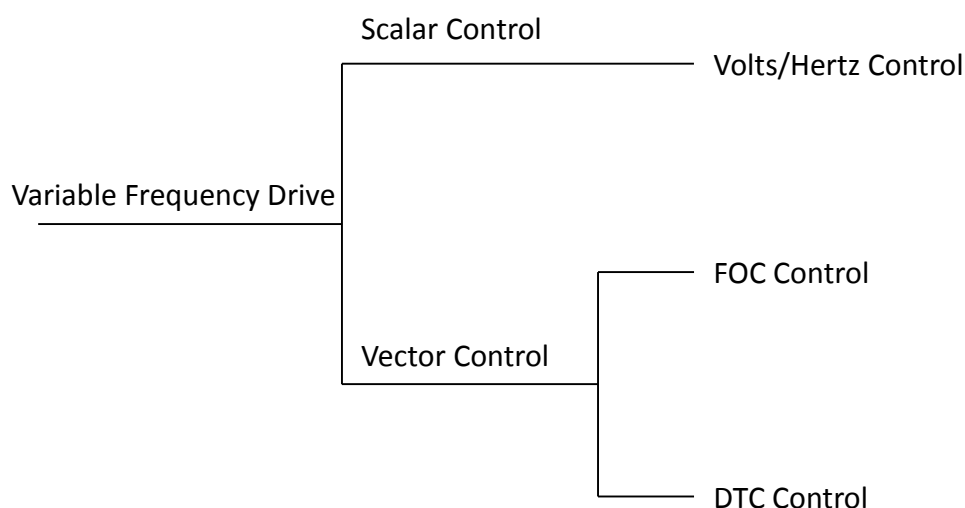
Figure 1.3: Motor control classification.

The classification of these motor control strategies is shown as Figure 1.3. The volts/hertz control, which is also called scalar control, is used in relatively simple applications such as pumps and fans. PMSMs are energized with a constant volts per hertz ratio which generates a constant airgap flux. The volts/hertz control is a cheap and well known method which is widely applied in industry. However, the dynamic performance of volts/hertz control leaves something to be desired. The reason is that this method controls the magnitude of voltage and frequency instead of the magnitude and phase of the current [15]. On the contrary to the simple scalar control, both the FOC

and DTC are complex vector controls which have fast dynamic response and high accuracy. The principle of FOC is that it transfers the three phase time variant stator currents to two equivalent dc components in which the torque and flux can be simply decoupled and separately controlled [16]. While the DTC employs the stator voltage space vectors to directly control the stator flux and the torque [17] according to the difference between the reference value and estimated results of torque and flux. Compared with the FOC, the DTC has faster dynamic response, however is more sensitive to stator resistance. It is difficult to clearly state the superiority of volts/hertz, FOC and DTC because of the balance of the merits. Ultimately, the application determines which control method should be implemented in a drive.

For different control objectives, several control strategies, which control the PMSM based on the FOC method, can be summarized as follows:

- MTPA control [18]

- FW control [18]

- Unity power factor control [19]

- Optimal efficiency control[20]

Compared with unity power factor control and optimal efficiency control, MTPA control and FW control are more practical in industrial drives. The reason stems from the maximum drive efficiency of MTPA control and wide PMSM operation speed range of FW control.

Since high power density, high efficiency PM motors have become the best replacements of internal combustion engines, the control of PM motors for EV applications has drawn much attention in recent publications [6, 21]. It is necessary for Evs as well as many other applications, to operate over both a wide speed range and

high efficiency. Therefore, a control strategy, which uses MTPA control at low speed, and FW control at high speed, was demonstrated in [22-24].
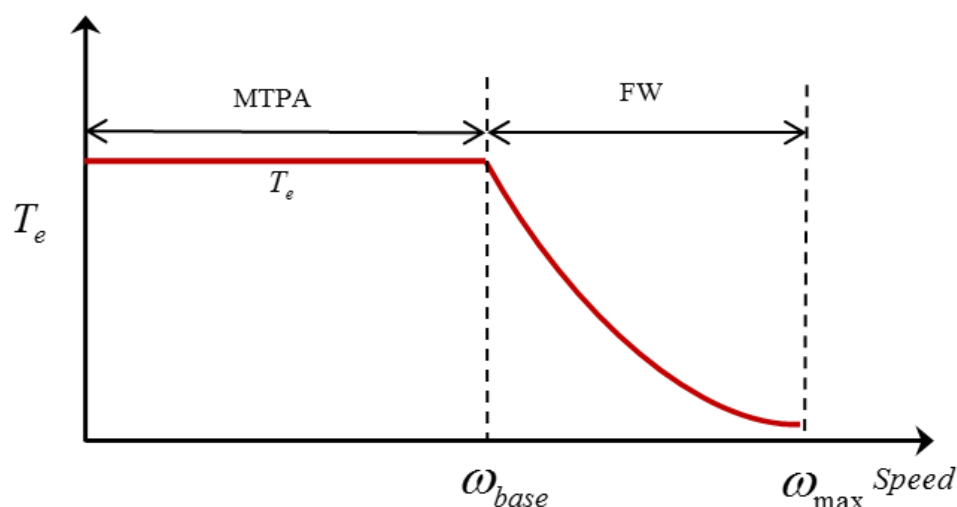
Figure 1.4: Ideal torque vs. speed characteristics for variable speed drives.

Generally, as shown in Figure 1.4, MTPA control is achieved with full field current throughout the speed range up to the base speed, which is the maximum speed that can be achieved without FW control [13]. Then, in FW control, holding-on to a constant armature current, the armature MMF space vector is re-oriented to a position that opposes the MMF of the PM, and hence reduces the total resultant flux in the air-gap. This is the basic idea of the so-called FW control in such machines. The weaker the net resultant air-gap flux the higher the motor speed. That is, in FW control the resultant air-gap flux is in inverse proportion to the motor speed.

The principle of MTPA control is that the maximum torque of a PM motor can be generated at a given phase current by keeping a particular torque angle, which is the angle between current phasor and positive d-axis direction in the d-q frame. In other words, there is a particular d-axis current and q-axis current pair that causes the minimum phase current for any torque level. As a result, the MTPA control leads to the

maximum motor-drive efficiency since the copper losses are minimized due to the minimized phase current.

The term "flux-weakening" is adopted in preference to the less precise "field-weakening," since the rotor MMF (field) of a PM motor is a fixed value dependent on PM geometry and material [12]. Precisely speaking, field-weakening can only be applied to motors under current controlled MMF (field).Hence, in FW control the objective is to reduce the output torque of a motor at speeds above the base speed. The reasons for such an objective stem from two major points. First, it is the only way to further extend a motor's speed under limited current and voltage. Second, it is reported in many publications, especially related to Evs, that a motor's load torque is in inverse proportion to such motor's speed. Thus, FW control is widely implemented for PM machines in high speed applications.

The principle of FW control in PMSMs is that the air-gap flux can only be weakened by applying a demagnetizing armature current component along the d-axis of the permanent magnets. Since the output torque is proportional to product of air-gap flux and q-axis current component, such torque can be reduced with FW control.

Work on FW control has been presented in many publications such as in [25-27]. Although the objectives are the same, various FW methods have been reported in recent years. The early feed forward torque control was modified to achieve FW operation as discussed in [12]. In [28], the author presented a six-step voltage control method for FW operation which gives the maximum utilization of the dc link voltage. Another approach was reported in [24], a voltage compensator and a current regulator with feed forward decoupling controller were proposed for the FW operation. In practical applications, the FW algorithm used in AC motor drives was first published in Kim's paper [23]. This method has two significant features which are simplicity of

implementation and robustness to the variation in the machine parameters. In [24], further improvement was achieved based on Kim's method.

As mentioned in many publications, one major drawback of all the conventional FW methods is that one must pay attention to the magnitude of the back-electromotive force (back-EMF), which is proportional to the rotor speed. Since the maximum inverter voltage is limited in conventional drives by the dc bus voltage, IPMSM motors cannot operate in speed ranges where the back-EMF is higher than the maximum output voltage of the drives, again the dc bus voltage. Thus, in EV applications where the dc bus voltage is limited, the aforementioned CPSR suffers from the constraint imposed by the drive side. The following section of this literature review discusses the limitation of conventional drives and introduced the Z-source inverter as an approach to improve FW performance and extend the CPSR.

1.2.2   Z-Source Inverters

Normally, there are two limitations for all the FW control strategies: maximum voltage and maximum current. From the design point of view, the current limitation is usually decided by the motor side in a motor-drive system, which depends on its thermal dissipation and cooling type. However, the voltage limitation is typically decided by the drive side, since the dc bus voltage is limited to given values in conventional drives. For example, the dc bus voltage in Evs is normally rated from 200 to 600 volts according to the chosen motor [29], and a three-phase input industrial drive usually has a 310 volts dc bus. As shown in Figure 1.5, where the dc bus voltage is a reference, the maximum output line-to-line voltage of a traditional/three-phase full-bridge inverter is about 0.78 of the dc bus voltage value that is 0.78 p.u. for a conventional six step inverter with 180˚ conduction cycle per switch [30]. This value is 0.612 p.u. in sinusoidal pulse width modulated (SPWM) inverters [30]. Meanwhile, it is 0.707 p.u.

for space vector pulse width modulated (SVPWM) inverters [27]. Although different modulation methods can be selected, the output voltage of conventional voltage source inverters are still limited because of the inherent step-down function in such inverters.
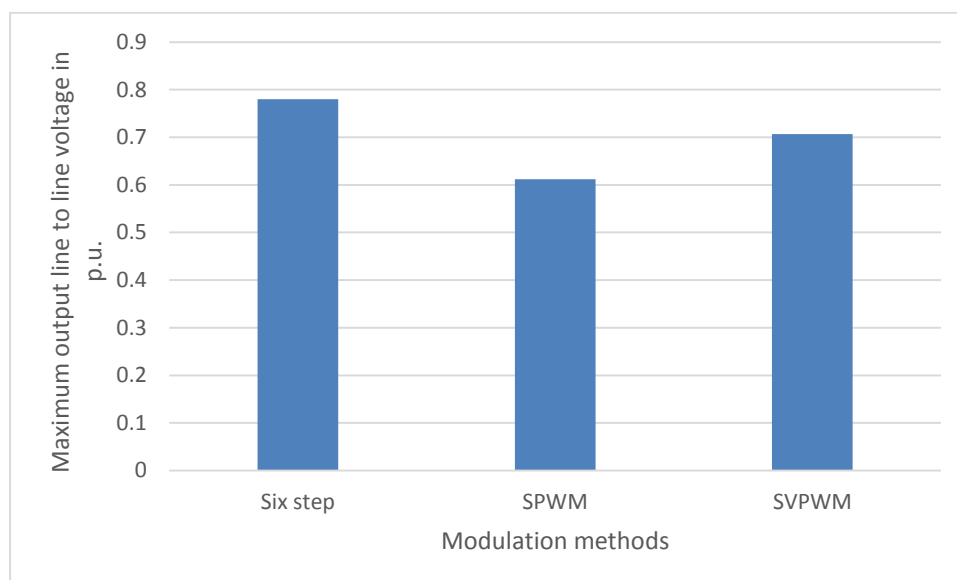
Figure 1.5: Maximum line-to-line voltage of three-phase full-bridge inverters.

In the 2004 Toyota Prius hybrid EV, as shown in Figure 1.6, the electric drive system contains a conventional inverter for powering a PMSM with a voltage-boost circuit that is helpful in both reducing the voltage stresses in the switching devices and expanding the motor's CPSR [31]. On the negative side, the dc-to-dc boosted pulse width modulation (PWM) inverter topology suffers from the excess cost and complexity associated with the two-stage power conversion.
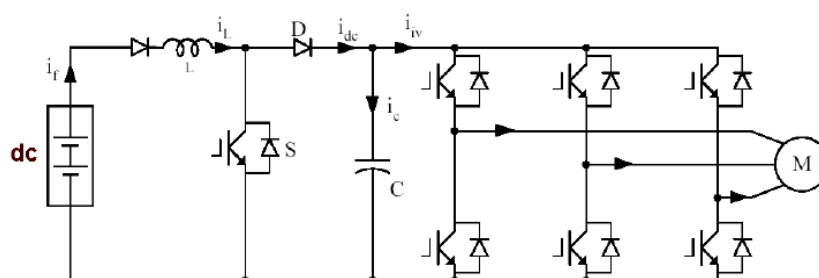
Figure 1.6: Prius drive system using dc/dc boost converter and PWM inverter.
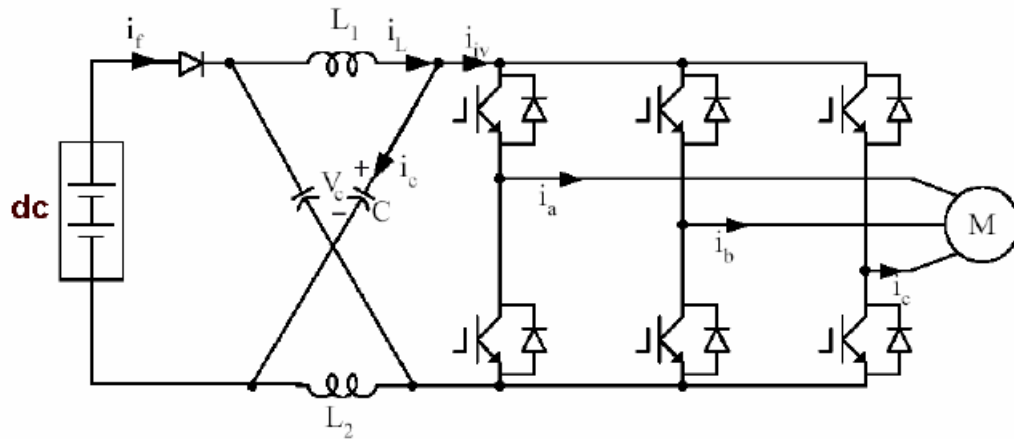
Figure 1.7: System configuration using the ZSI.

Instead of using a dc/dc boost converter, there are several topologies that can boost the output voltage of a drive. The recently presented Z-source inverter (ZSI) [32] and its' extended topologies, quasi-Z-source inverters (qZSIs) [33] are all emerging boost inverters which are very suited for many applications, including hybrid Evs and fuel-cell vehicles [34]. The dc/dc boost converter in the Prius drive can be replaced by an impedance network such as the ZSI as shown in Figure 1.7. One attractive merit of such ZSIs and qZSIs is that they can buck/boost the voltage with a single stage configuration, which indicates no requirement for any dc-dc converter to boost the dc bus voltage [35]. Such advantage can be used to overcome the output voltage constraints of conventional drives. Moreover, the ZSIs also demonstrate fault-tolerant capabilities to shoot-through faults and voltage sags. Thus, recent publications [36, 37] gave more and more attention to motor drives implementing ZSIs.

There are many classical converters which could achieve extra advantages by implementing the impedance network of ZSIs, such as Z-source multilevel inverters [38], and Z-source matrix inverters [39]. Moreover, recent publications also modified ZSIs for more merits, such as the improved Z-source inverter in [40], and switched inductor Z-source inverter in [41]. For simplicity purposes, this thesis will focus on the

original ZSIs, while other topologies will be generally discussed in Chapter 3.

Unlike the traditional PWM inverter with a modulation index as the only control degree of freedom, the ZSIs have two control degree of freedom, one using shoot-through duty cycle and the other one using the modulation index. There are three widely used control methods for ZSIs:

- Simple boost control [32]

- Maximum boost control [42]

- Maximum constant boost control [43]

Other ZSI control methods are also available, for instance, SVPWM [44]. The major difference between these methods lies in the harmonic distortion, voltage boost ability and voltage stress on switching devices.

According to the literature review, very few researchers investigated the use of FW control with a boosted voltage-source inverter for Evs and other applications. Moreover, the literature review also shows very insufficient research on control algorithms of ZSIs during the FW operation. Therefore, in order to improve CPSR and FW performance, a proper control method of ZSIs has to been developed to support the FW operation with boosted voltage.

1.3 Thesis Contributions and Organization

In this thesis, a new FW control algorithm for IPMSMs will be presented. The principal feature of the proposed algorithm is that it eliminates the dc bus voltage constraint to FW operation by implementing a boost converter which is the ZSI. Theoretical analysis and simulation will be conducted to verify the feasibility and advantages of such control strategy. Compared with the conventional FW strategies, the introduced new method can significantly extend the CPSR and corresponding torque of IPMSMs. It should be noticed that among such merits are of high importance

for traction applications, e.g. Evs.

There are five chapters in this thesis. The organization is as follows:

Chapter 1 briefly reviews the background of PMSMs, FW approaches and ZSIs.

Chapter 2 deduces the conventional FW control algorithms.

Chapter 3 presents the schematic and operation principle of the ZSIs.

Chapter 4 demonstrates the control strategies for closed-loop FW control with conventional inverters and ZSIs. A new control algorithm will be also presented here.

Chapter 5 summarizes the accomplishments of this thesis and proposes ideas for future work.

Chapter 2

Control of Permanent Magnet Synchronous Motors

Control techniques are critical to exploit the power capability of PMSMs over the entire speed range. This chapter presents details of maximum torque per ampere (MTPA) control and flux-weakening (FW) control for IPM motors. Before control algorithms are analyzed, a proper motor model is established at the beginning.

2.1 Introduction

It should be emphasized that PMSMs are attracting growing attention for a wide variety of industrial applications, from simple applications like pumps or funs to high-performance drives such as machine-tool servos [16]. Normally, most drives for the aforementioned applications are designed to achieve high efficiency and wide speed range as much as possible.

In traction applications, it is a physical phenomenon that the load torque is usually in inverse proportion to the vehicle speed. Thus, in the low speed range of such applications, the MTPA control which gives the maximum torque for a given current value is preferred. This method is widely used in control of both induction motors and PMSMs. However, in the high speed range of traction applications such as EVs, to keep a high drive torque is not as important as that in the low speed region. As the desired objective changes to increasing the motor speed, the FW control which extends the speed range of the aforementioned applications becomes not only more desired but necessary.

In general, large speed ranges are possible either with SPM machines which exhibit little or no saliency because they have surface mounted PMs, even with concentrated winding configurations, or with IPM machines which have high saliencies

and inset PMs [45]. However, with respect to SPM motors, IPM motors offer the advantage of higher inductance values, which implies smaller demagnetization currents for the FW operation [46]. Moreover, the mechanical structure of IPM motors is more rugged/robust overcoming the centrifugal forces on their rotors at high speeds. Thus, IPM motors have become more and more popular for high performance applications, i.e. Evs. Since IPM motors are more suited for FW control as explained above, the analysis of FW algorithms will focus on such IPM motors. However, in order to give a full account of FW control, FW methods used for SPM motors will be introduced as well.

At the beginning of this chapter, a mathematical model of the PMSM is introduced in section 2.2. Then, theoretical analysis of steady state controls for the entire speed range which include MTPA and FW algorithms are analyzed in section 2.3.

2.2 The Mathematical model of PMSMs

In term of phase variables, the electric circuit equations of PMSMs, based on Faraday's law, can be written as follows:

$$v_a = R_s i_a + \frac{d\lambda_a}{dt} \tag{2.1}$$

$$v_b = R_s i_b + \frac{d\lambda_b}{dt} \tag{2.2}$$

$$v_c = R_s i_c + \frac{d\lambda_c}{dt} \tag{2.3}$$

where (v_a, v_b, v_c), (i_a, i_b, i_c) and R_s refer to the phase voltages, phase currents and resistance per phase, respectively. Here, the a, b and c phase flux linkage equations are [26]:

$$\lambda_a = L_{aa} i_a + L_{ab} i_b + L_{ac} i_c + \lambda_{ma} \tag{2.4}$$

$$\lambda_b = L_{ab}i_a + L_{bb}i_b + L_{bc}i_c + \lambda_{mb} \tag{2.5}$$

$$\lambda_c = L_{ca}i_a + L_{cb}i_b + L_{cc}i_c + \lambda_{mc} \tag{2.6}$$

Where, L_{aa}, L_{ab}, L_{ac}, $\cdots$, L_{cc}, represent the various phase and phase-to-phase self and mutual inductances, respectively. Meanwhile, the λ_{ma}, λ_{mb}, and λ_{mc}, refer to the components of the phase flux linkages induced by the PMs.
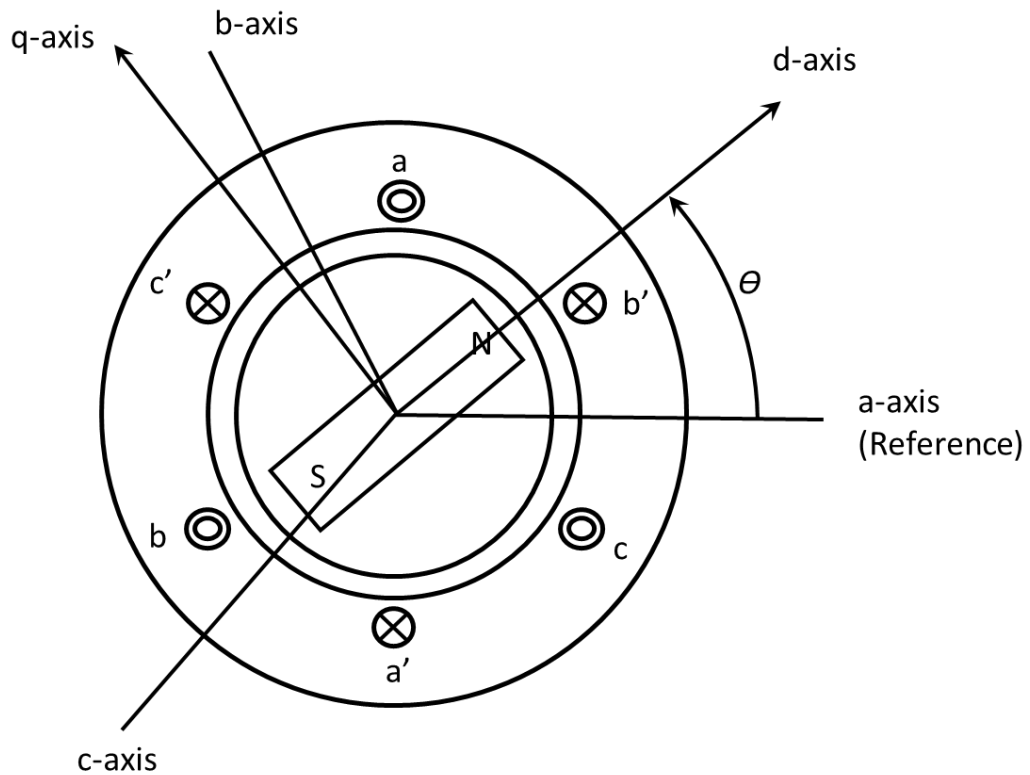
Figure 2.1: *D-q* coordinate frame of PMSMs.

In the above equations, the inductances are functions of the rotor position. Here, the rotor position angle θ is defined in term of the angle between the magnetic axis of phase (a) and the rotor q-axis as shown in Figure 2.1. Meanwhile, the flux linkages of the stator phase windings due to the PMs can hence be expressed as follows:

$$\lambda_{ma} = \lambda_{pm} \cos\theta \tag{2.7}$$

$$\lambda_{mb} = \lambda_{pm} \cos(2\pi/3 - \theta) = \lambda_{pm} \cos(\theta - 2\pi/3) \qquad (2.8)$$

$$\lambda_{mc} = \lambda_{pm} \cos(4\pi/3 - \theta) = \lambda_{pm} \cos(\theta - 4\pi/3) \qquad (2.9)$$

where, $\hat{\lambda}_{pm}$ is the amplitude of the flux produced by the PMs and the angle θ is a time-varying function of the rotor position, which can be represented as follows:

$$\theta = \int \omega_e dt + \theta_0 \qquad (2.10)$$

where ω_e is the electrical speed of the rotor magnetic field and θ_0 is the initial rotor position angle.

Basically, a PMSM machine can be looked at as a transformer with a moving secondary, where the coupling coefficients between the stator and rotor phases change continuously with the change of the rotor position [18]. As presented above, the machine model can be described by differential equations with time-varying inductances which are functions of the rotor position. However, such a model tends to be very complex because of the time varying inductance coefficients and associated inductance matrix. In the 1920s, R. H. Park [47] presented a new theory for such ac electric machine analysis to eliminate the difficulty with the time-varying parameters/inductances, which is usually called the d-q Park's transformation, or the two-reaction theory. Through this method, the variables in the three-phase stationary reference frame will be transformed to constants in the synchronously rotating reference frame, which is also called d-q reference frame. Here, that the d-axis is oriented at an θ angle ahead of the phase a-axis, as shown in Figure 2.1. The voltage transformation can be written as follows:

$$\begin{bmatrix} v_d \\ v_q \\ v_o \end{bmatrix} = \frac{2}{3} \begin{bmatrix} \cos\theta & \cos(\theta - \frac{2\pi}{3}) & \cos(\theta + \frac{2\pi}{3}) \\ \sin\theta & \sin(\theta - \frac{2\pi}{3}) & \sin(\theta + \frac{2\pi}{3}) \\ 0.5 & 0.5 & 0.5 \end{bmatrix} \begin{bmatrix} v_a \\ v_b \\ v_c \end{bmatrix} \qquad (2.11)$$

Let T represent the Park's transformation matrix, and S represent the a, b, and c vector of any of the phase variables, current, voltage, and flux linkage. Here, Park's transformation can be written in a generalized form as follows:

$$\begin{bmatrix} s_d \\ s_q \\ s_o \end{bmatrix} = \frac{2}{3} T \begin{bmatrix} s_a \\ s_b \\ s_c \end{bmatrix} \qquad (2.12)$$

where T is:

$$T = \begin{bmatrix} \cos\theta & \cos(\theta - \frac{2\pi}{3}) & \cos(\theta + \frac{2\pi}{3}) \\ \sin\theta & \sin(\theta - \frac{2\pi}{3}) & \sin(\theta + \frac{2\pi}{3}) \\ 0.5 & 0.5 & 0.5 \end{bmatrix} \qquad (2.13)$$

With Park's transformation, the stator voltage equations in d-q frame are [48]:

$$v_d = R_s i_d + \frac{d\lambda_d}{dt} - \omega_e \lambda_q \qquad (2.14)$$

$$v_q = R_s i_q + \frac{d\lambda_q}{dt} + \omega_e \lambda_d \qquad (2.15)$$

where, λ_d is the d-axis flux linkage and λ_q is the q-axis flux linkage, which can be expressed as follows:

$$\lambda_d = L_d i_d + \lambda_{pm} \qquad (2.16)$$

$$\lambda_q = L_q i_q \qquad (2.17)$$

Where, L_d is the d-axis inductance, L_q is the q-axis inductance, and $\hat{\lambda}_{pm}$ is the amplitude of flux linkage due to the permanent magnet. According to (2.14) and (2.15), a dynamic equivalent circuit of a PMSM in the d-q frame can be drawn as shown in Figure 2.2.
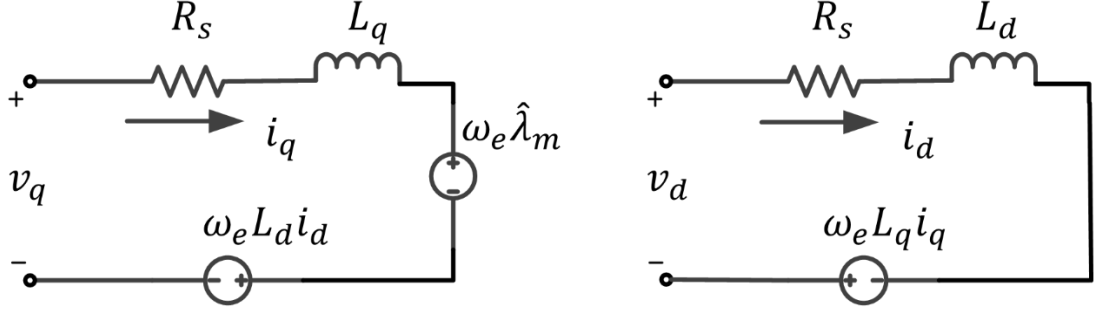
Figure 2.2: Equivalent circuit of a PMSM.

In the steady state at a constant speed λ_d and λ_q become time independent, hence, $d\lambda_d / dt$ and $d\lambda_q / dt$ can be eliminated from the formulation. If the stator resistance is negligible or neglected, it follows that the PMSM model can be represented by a standard mathematical model in the d-q frame as follows [49]:

$$v_d = -\omega_e \lambda_q \tag{2.18}$$

$$v_q = \omega_e \lambda_d \tag{2.19}$$

$$\hat{I}_s = \sqrt{i_d^2 + i_q^2} \tag{2.20}$$

$$\hat{V}_s = \sqrt{v_d^2 + v_q^2} \tag{2.21}$$

where, $\hat{I}_s$ and $\hat{V}_s$ are the amplitudes of the space vector of the currents and voltages, respectively.

Substitute (2.16) and (2.17) into the d-q voltage equations (2.18) and (2.19) above, one can obtain a model directly related to d-q current components as follows:

$$v_d = -\omega_e L_q i_q \tag{2.22}$$

$$v_q = \omega_e (L_d i_d + \lambda_{pm}) \tag{2.23}$$

In the d-q frame, the input power of a PMSM can be written as:

$$P_{in} = \begin{bmatrix} v_a & v_b & v_c \end{bmatrix} \begin{bmatrix} i_a \\ i_b \\ i_c \end{bmatrix} = \frac{3}{2} \begin{bmatrix} v_d & v_q \end{bmatrix} \begin{bmatrix} i_d \\ i_q \end{bmatrix} \tag{2.24}$$

Assuming the motor losses are negligible, then the input power equals the output power, P_{out}, of the motor, which can be represented as follows:

$$P_{out} = \frac{3}{2}(v_d i_d + v_q i_q) \tag{2.25}$$

By substituting (2.22) and (2.23) into the upper equation (2.25), one can obtain the following:

$$P_{out} = \frac{3}{2}\omega_e \left(\lambda_{pm} i_q + (L_d - L_q) i_d i_q \right) \tag{2.26}$$

From the output power equation presented above, the output torque of a PMSM can be deduced. First, the electrical speed of PMSMs is equal to the product of the mechanical speed times the number of pole pairs, which can be expressed as:

$$\omega_e = \frac{p}{2}\omega_m \tag{2.27}$$

where, p is the number of poles. Then (2.25) can be rewritten as follows:

$$P_{out} = \frac{3}{2}\frac{p}{2}\omega_m \left(\lambda_{pm} i_q + (L_d - L_q) i_d i_q \right) \tag{2.28}$$

Since the output power is a product of the motor mechanical speed time the developed/output torque, the output torque can be obtained as:

$$T_e = \frac{P_{out}}{\omega_m} = \frac{3}{2}\frac{p}{2}\left(\lambda_{pm} i_q + (L_d - L_q) i_d i_q \right) \tag{2.29}$$

The machine's dynamic equation can therefore be written as follows:

$$T_e - T_{load} - T_{friction} = J \frac{d\omega_m}{dt} \qquad (2.30)$$

where, T_{load} is the load torque, $T_{friction}$ is the motor-load system friction torque, and J is the polar moment of inertia of the rotor and the connected load.

It is apparent from the above equation (2.29) that the torque expression for PMSMs is composed of two components. The first component is called "magnet excitation torque" which is proportional to λ_{pm} and the q-axis current. The second component corresponds to "reluctance torque" due to the difference between the d and q axes reluctances (inductances). Since the reluctivity of PM materials is very close to that of the air, SPM motors are usually considered to have the same reluctance in both d-axis and q-axis, hence the reluctance torque component is zero for these types of motors. Meanwhile, IPM motors have lower reluctance along the q-axis than that along the d-axis. Therefore, this reluctance torque component has a positive value for such IPM motors with a negative d-axis current. This is also one of the merits of utilizing the IPM motors for the FW operation where the d-axis current keeps increasing in the negative direction.

2.3 Steady State Control of PMSMs

The main principle in any machine control is to obtain a desired rotating speed. In order to have such desired speed, the drive torque produced by the machine has to be controlled. For induction machines, there are three main categories of motor control methods, which are:

- Volts/hertz control [50]

- Field oriented control (FOC) [51]

- Direct torque control (DTC) [52]

There is no essential difference between the control of induction motors and the control of PMSMs. The above control methods for induction machines are also the major control methods applicable to PMSMs.

The volts/hertz control is simple and cheap in implementation. It is usually designed as an open-loop control. Thus, a resolver/encoder is not required. However, it is not an option for high performance applications because of the fact hat the torque is not controllable.

Among the three types of control methods, the FOC is the best solution for high performance drives. This type of control usually has two closed-control loops. The outer loop is the speed loop which needs a resolver/encoder for the speed feedback. The inner loop is the current loop which controls the torque indirectly. Thus, this method has fast torque response and accurate speed control. The main disadvantage of this control method is the higher cost in comparison to the volts/hertz control. It has to be noticed that the resolver/encoder is not necessary if sensorless FOC schemes/methods are applied.

Instead of controlling torque via the regulation of current, DTC attempts to integrate the control of flux and torque in a single switching algorithm, taking advantage of the fact that the voltage can be changed extremely fast when the inverter electronics switches change state [25]. This approach achieves field orientation without any speed feedback. This type of control also has the fastest torque response among all the control methods. The major drawback is that the hysteresis controller used in this kind of control causes large torque ripples distortion and variable switching frequencies.

It is difficult to state the superiority of these methods discussed above. Ultimately, the application determines which method should be implemented. For high

performance applications, the FOC is a promising method which has been widely used for a long time. Therefore, next section presents the analysis of the FOC strategies which includes MTPA control and FW control for traction and electric appliance drive applications.

2.3.1 Field Oriented Control
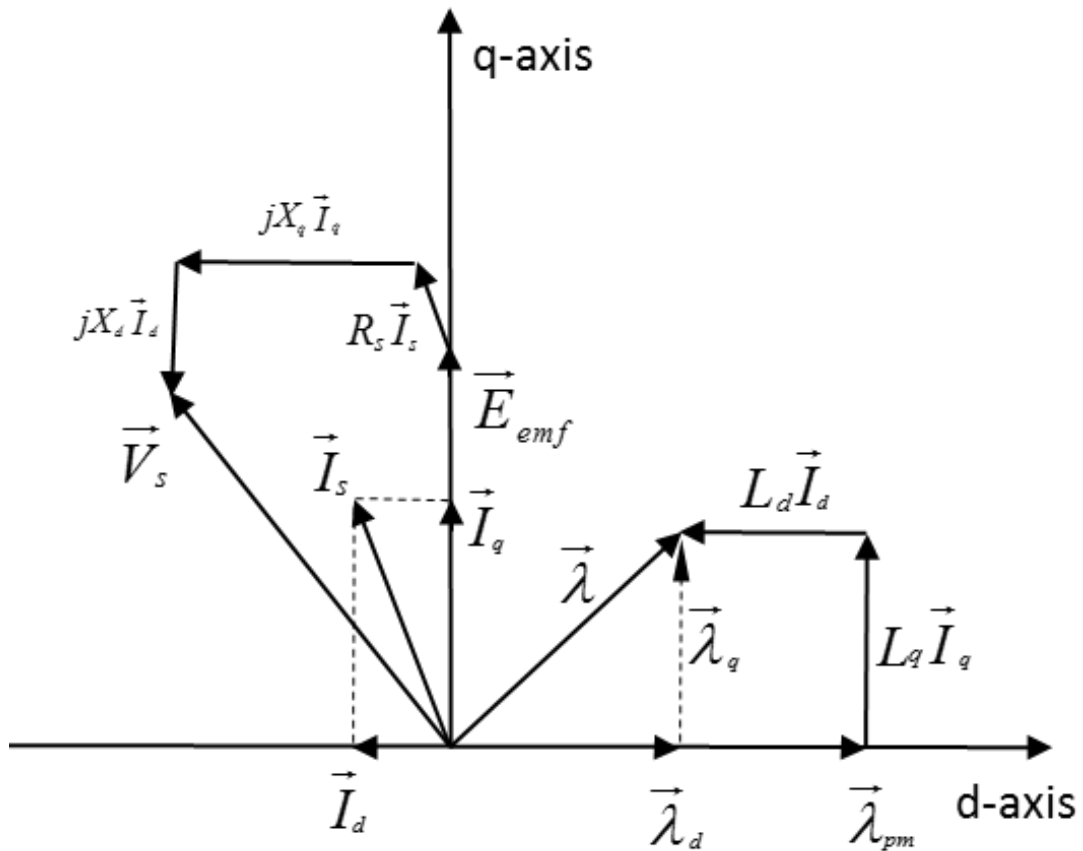
Figure 2.3: Phasor diagram of a PMSM in d-q frame.

The concept of FOC was first invented in the beginning of 1970s [53]. This method brought forward intensive efforts in investigating high performance control of ac drives because of the fact that an induction motor controlled by an FOC method/algorithm can be controlled in a similar manner to the control of a separately excited dc motor [18]. Such FOC is also known as vector control, decoupling control,

and orthogonal control [18]. In general, the principle of FOC schemes implies independent (decoupled) control of flux – current and torque – current components of a stator current through a coordinated change in the supply voltage amplitude, phase angle and frequency. As the flux variation tends to be slow, especially with current control, constancy of flux should produce a fast torque response, and consequently reasonable speed response [50].

The fundamental objective of most FOC algorithms is to control the amplitude, phase, and frequency of stator flux linkages. This objective can be achieved by controlling the stator current phasor, $\vec{I_s}$ as shown in Figure 2.3. In terms of phasor components as shown in Figure 2.3, the voltage equation can be expressed as follows:

$$\vec{V}_s = \vec{E}_{emf} + R_s\vec{I}_s + jX_d\vec{I}_d + jX_q\vec{I}_q \qquad (2.31)$$

where, $\vec{V}_s$ is the stator phase voltage, $\vec{E}_{emf}$ is the back-EMF in a PM motor, $\vec{I}_s$ is the stator current phasor, and X_d/X_q are the d/q axes reactances. The value of the back-EMF, E_{emf}, can be calculated from the flux linkage due to the permanent magnet, λ_{pm}, as follows:

$$E_{emf} = \omega_e\lambda_{pm} \qquad (2.32)$$

Notice, in the phasor diagram of Figure 2.3, voltages, currents and flux linkages are in RMS values.

To illustrate how the FOC method controls the motor in a motor-drive system, a general control structure is presented in Figure 2.4 for a better demonstration. There are two loops in the control scheme of Figure 2.4: the inner current loop and the outer speed loop. Normally, the current loop is used to obtain a desired torque. Meanwhile, the speed loop assures that the actual speed follows the commanded speed.
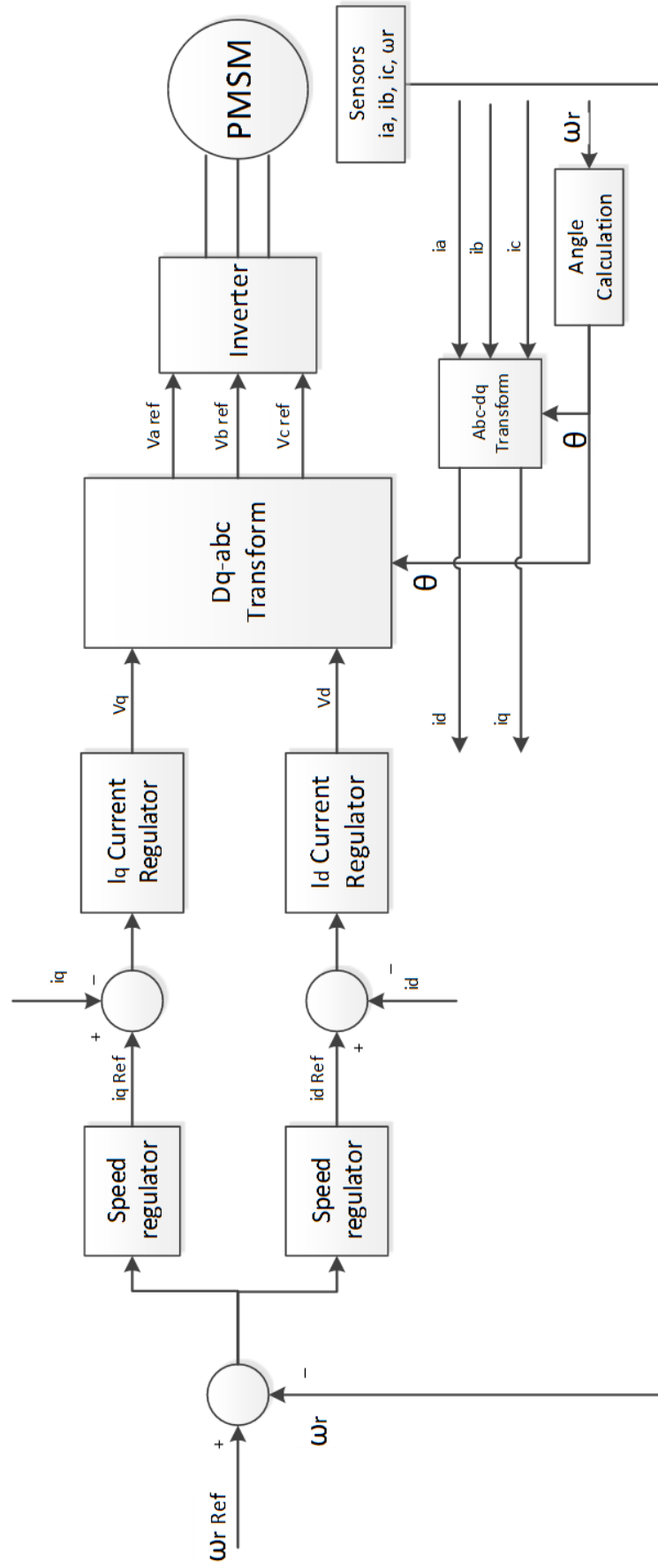
Figure 2.4: General control scheme of the Field Oriented Control.

In most controller designs related to FOC logic structure, control algorithms are embedded in the speed regulator portion of the speed loop. Thus, the design of the speed regulator could be simple or complex according to the various FOC algorithms. Notice that there is no reference torque that can be found in Figure 2.4. This does not mean that the torque is not controlled. In fact, a reference torque can be generated by the speed regulator. Then, current references can be obtained according to this commanded reference torque. Moreover, torque feedback can also be added into the speed regulator through a torque transducer, not shown in Figure 2.4. To avoid complexities, the general speed regulator can be decomposed into the speed regulator which gives the torque reference, and the torque regulator which produces the current reference. In general, the speed regulator is the main controller in most FOC logic structures. As to the inner-loop controller, the current regulator assures that the current follows its reference value which is the output of the speed regulator. The design of the current regulator usually depends on motor parameters. While, the design of the speed regulator is usually based on the nature of the control algorithms.

In conventional FOC categories, there are several control algorithms/strategies, which, namely, are the MTPA strategy, the FW strategy, unity power factor control, and optimal efficiency control, etc. [18-20]. For traction applications, the MTPA control is the most effective strategy in the low speed regions. While, the FW control is necessary in high speed applications. Although MTPA and FW employ different algorithms, they are FOC methods in their nature.

2.3.2 Maximum Torque Per Ampere (MTPA) Control Algorithm

In order to produce the maximum torque at a given current value, the torque expression for PM motors has to be analyzed. For SPM motors, which have no saliency,

the reluctance torque is zero. Thus, for SPM motors, the torque expression (2.29) can be rewritten as follows [25]:

$$T_e = \frac{3}{2}\frac{p}{2}\lambda_{pm}i_q \tag{2.33}$$

Keeping $i_q = \hat{I}_s$ and $i_d = 0$, it is the most convenient approach to control an inverter-fed SPM motor in order to produce the maximum torque.
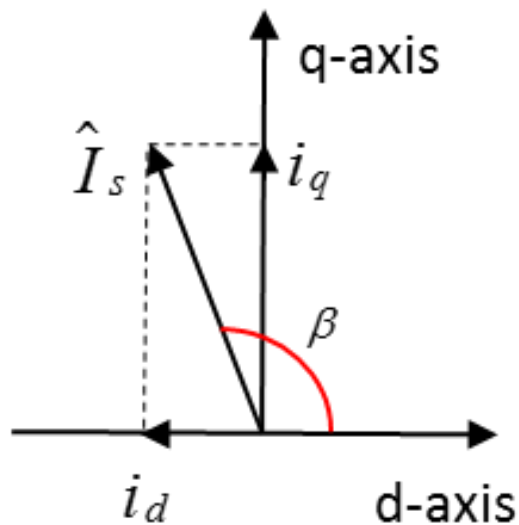
Figure 2.5: Torque angle.

Since IPM motors have larger q-axis reactance/inductance than d-axis reactance/inductance, that is, $L_q > L_d$, the reluctance torque is present. Therefore, the maximum torque becomes a combination of the magnet excitation torque and the reluctance torque. From the Figure 2.5, we can write:

$$i_d = \hat{I}_s\cos\beta \tag{2.34}$$

$$i_q = \hat{I}_s\sin\beta \tag{2.35}$$

where, $\hat{I}_s$ is the amplitude of the stator phase current of an IPM motor, and β ($180^\circ > \beta \geq 0^\circ$) is defined as the "torque angle", which is the angle between the stator phase current vector and the positive direction of the d-axis as shown in Figure 2.5.

By substituting (2.34) and (2.35) into (2.29), one can obtain the following:

$$T_e = \frac{3}{2}\frac{p}{2}\left(\lambda_{pm}\hat{I}_s\sin\beta + (L_d - L_q)\hat{I}_s\cos\beta\,\hat{I}_s\sin\beta\right)$$

or
$$T_e = \frac{3}{2}\frac{p}{2}\left(\lambda_{pm}\hat{I}_s\sin\beta + (L_d - L_q)\hat{I}_s^2\frac{\sin 2\beta}{2}\right) \qquad (2.36)$$

As aforementioned earlier, the developed torque can be seen as a combination of the magnet excitation torque, T_{mag}, and the reluctance torque, T_{rel}, which can be expressed as follows:

$$T_e = T_{mag} + T_{rel} \qquad (2.37)$$

where,
$$T_{mag} = \frac{3}{2}\frac{p}{2}\lambda_{pm}\hat{I}_s\sin\beta \qquad (2.38)$$

$$T_{rel} = \frac{3}{2}\frac{p}{2}(L_d - L_q)\hat{I}_s^2\frac{\sin 2\beta}{2} \qquad (2.39)$$

As the torque angle, β, changes, the variation of the magnet excitation torque and the reluctance torque can be seen in Figure 2.6, which is obtained from the simulation results by substituting the parameters in Table 2.1 into the torque equations (2.38) and (2.39).

Motor Parameters	
$\hat{\lambda}_{pm}$	0.148wb
L_d	0.0054H
L_q	0.0105H
$\hat{I}_s$	10A
Number of poles (p)	6

Table 2.1: IPM motor parameters for MTPA simulation.
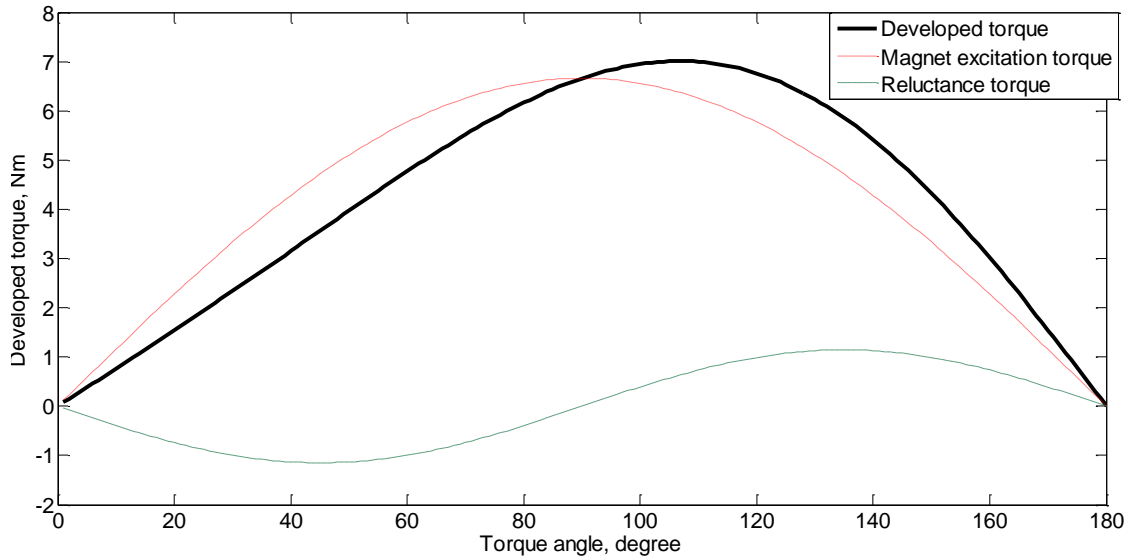
Figure 2.6: Developed torque vs. torque angle of IPM motors.

As shown in Figure 2.6, the torque angle corresponding to the maximum magnet excitation torque does not provide the maximum developed torque. Since SPM motors don't have any significant reluctance torque component, the magnet excitation torque and the developed torque are equal in SPM motors. Therefore, this also implies that IPM motors have higher maximum developed torque than SPM motors. The torque angle which results in the maximum torque of IPM motors can be derived by setting the derivative of the torque in (2.36) to zero, which can be expressed as follows:

$$\frac{dT_e}{d\beta} = \frac{3}{2}\frac{p}{2}\left(\lambda_{pm}\hat{I}_s\cos\beta + (L_d - L_q)\hat{I}_s^2\cos 2\beta\right) = 0 \qquad (2.40)$$

For further simplicity, (2.40) can be rewritten as follows:

$$\lambda_{pm}(\hat{I}_s\cos\beta) + (L_d - L_q)\left((\hat{I}_s\cos\beta)^2 - (\hat{I}_s\sin\beta)^2\right) = 0 \qquad (2.41)$$

By substituting (2.34) and (2.35) into (2.41), one can obtain:

$$\lambda_{pm}i_d + (L_d - L_q)(i_d^2 - i_q^2) = 0 \qquad (2.42)$$

Since $i_d^2 + i_q^2 = \hat{I}_s^2$, it follows that i_q can be expressed as follows:

$$i_q = \sqrt{\hat{I}_s^2 - i_d^2}$$ (2.43)

By substituting (2.43) into (2.42), a binominal equation of d-axis current can be written as follows:

$$2(L_d - L_q)i_d^2 + \lambda_{pm} i_d - (L_d - L_q)\hat{I}_s^2 = 0$$ (2.44)

From (2.44), two solutions can be obtained as follows:

$$i_{d1} = \frac{\lambda_{pm} + \sqrt{\lambda_{pm}^2 + 8(L_q - L_d)^2 \hat{I}_s^2}}{4(L_q - L_d)} > 0$$

$$i_{d2} = \frac{\lambda_{pm} - \sqrt{\lambda_{pm}^2 + 8(L_q - L_d)^2 \hat{I}_s^2}}{4(L_q - L_d)} < 0$$ (2.45)

Since IPM motors have larger L_q than L_d, to obtain a positive reluctance torque, one has to keep the torque angle larger than $90°$, which can be obtained from (2.39). Therefore, the projection of $\hat{I}_s$ on the d-axis should have a negative value due to such torque angle, which also indicates that i_{d2} in (2.45) is the expected useful solution.

From the above, the d- and q-axis currents for MTPA control of IPM motors can be expressed as follows:

$$i_{dm} = \frac{\lambda_{pm} - \sqrt{\lambda_{pm}^2 + 8(L_q - L_d)^2 \hat{I}_s^2}}{4(L_q - L_d)}$$ (2.46)

$$i_{qm} = \sqrt{\hat{I}_s^2 - i_{dm}^2}$$ (2.47)

Here, the torque angle, β, for this maximum torque condition is hence obtained as follows:

$$\beta_m = \arctan(\frac{i_{qm}}{i_{dm}})$$ (2.48)

Although voltage constraints are not taken into consideration in the MTPA control, the

developed torque is limited by supply current. For each supply current value, there is a

particular pair of d-axis current and q-axis current that results in the maximum torque

under that condition. Therefore, the torque angle for the MTPA operation is determined

not only by motor parameters but also by supply current value. For different supply

currents, there are different cross points between the current circles and the MTPA

trajectory as shown in Figure 2.7, which yields different torque angles for MTPA

operations.
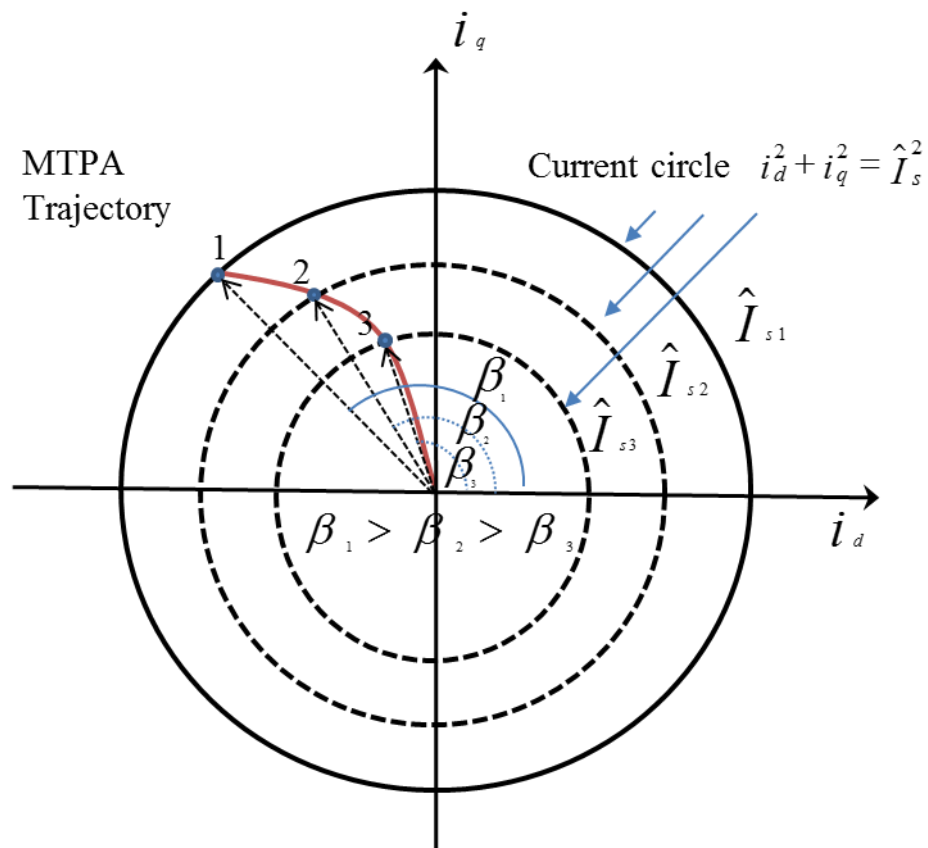
Figure 2.7: The MTPA trajectory for IPM motors

2.3.3 Flux-Weakening Control Algorithms

For traction applications in Evs, PMSM-drive systems normally require a wide

constant power speed range (CPSR). However, a specific power inverter cannot drive

PMSMs at high speeds because of the fact that the back-EMF is proportional to motor

speed and air gap flux, thus, leading to higher back-EMF values. Once the back-EMF becomes larger than the maximum output voltage of the drive, the PMSM will be incapable of drawing current and hence incapable of developing torque. Thus, when the back-EMF reaches the voltage threshold of a drive, the rotor speed of such a motor cannot be increased unless the air gap flux can be weakened. Considering that the rotor magnetic field generated by the PMs can only be weakened indirectly through armature MMF demagnetization of the PMs, and hence, an extended speed range can be achieved by means of FW control. During the FW operation region, a demagnetizing MMF is established by the stator currents and winding to counteract the "apparent" MMF established by PMs mounted on the rotor. As a result, the resultant air-gap flux is indirectly reduced/weakened and correspondingly the motor speed is increased [54].
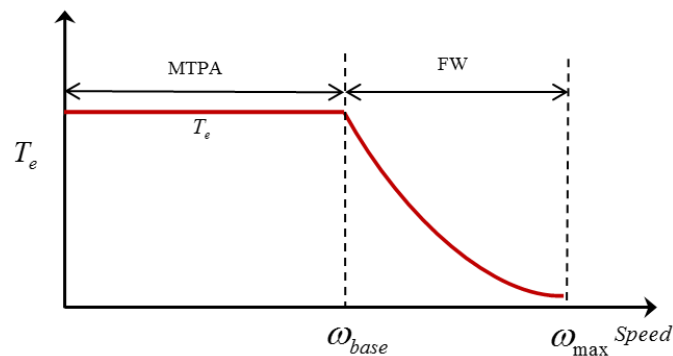
(a) Torque vs. speed
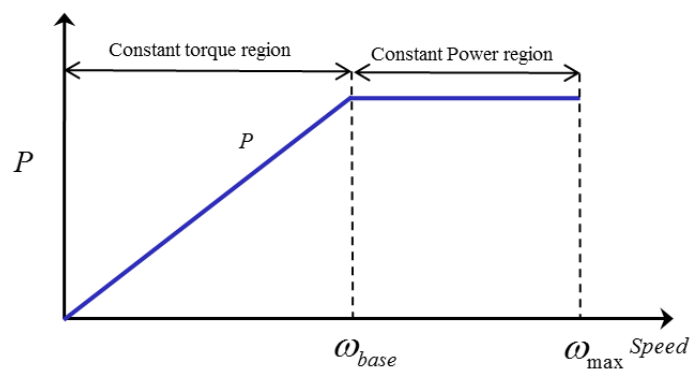
(b) Power vs. speed

Figure 2.8: Typical torque and power characteristics of PMSMs.

Without FW control, the back-EMF of a PM motor will keep increasing with speed. Therefore, the output voltage of the drive for such a PM motor has to be increased to keep desired phase currents. In the constant torque region as shown in Figure 2.8, a motor can be accelerated by the maximum torque until the terminal voltage of such motor reaches its limit value at $\omega_e = \omega_{base}$, which is defined as the base speed or corner speed. Such base speed is the highest speed of a PM motor controlled by the aforementioned MTPA method.

Substituting (2.22) and (2.23) into (2.21), one can obtain the following for the space vector of the stator terminal voltage, $\hat{V}_s$:

$$\hat{V}_s = \sqrt{\left(\omega_e L_q i_q\right)^2 + \left(\omega_e (L_d i_d + \lambda_{pm})\right)^2} \tag{2.49}$$

Thus, from (2.49) the electrical speed, ω_e, has to satisfy the following expression:

$$\omega_e = \frac{V_s}{\sqrt{(L_d i_d + \lambda_{pm})^2 + (L_q i_q)^2}} \tag{2.50}$$

Hence, the base speed, ω_{base}, can be obtained as follows:

$$\omega_{base} = \frac{V_{max}}{\sqrt{(L_d i_{dm} + \lambda_{pm})^2 + (L_q i_{qm})^2}} \tag{2.51}$$

where, $\hat{V}_{max}$ is the amplitude of the maximum output voltage space vector of a drive, and i_{dm}/i_{qm} are the d/q axes currents for the MTPA operation condition.

Normally, for all the FW control algorithms, there are two constraints that should be considered: namely the maximum current and the maximum voltage. Unlike the aforementioned MTPA control, the torque capability in the FW region is determined by both current and voltage limitations. In a motor-drive system, the current limitation is usually decided by the motor side, which depends on a motor's thermal dissipation and cooling means. However, the maximum voltage is typically decided by the drive

side, which has a limited dc bus voltage.

The current limitation, $\hat{I}_{max}$, which is the amplitude of the maximum phase current, can be drawn as a circle in the d-q frame as shown in Figure 2.9, which can be formulated in the following fashion:

$$i_d^2 + i_q^2 = \hat{I}_s^2 \leq \hat{I}_{max}^2 \qquad (2.52)$$
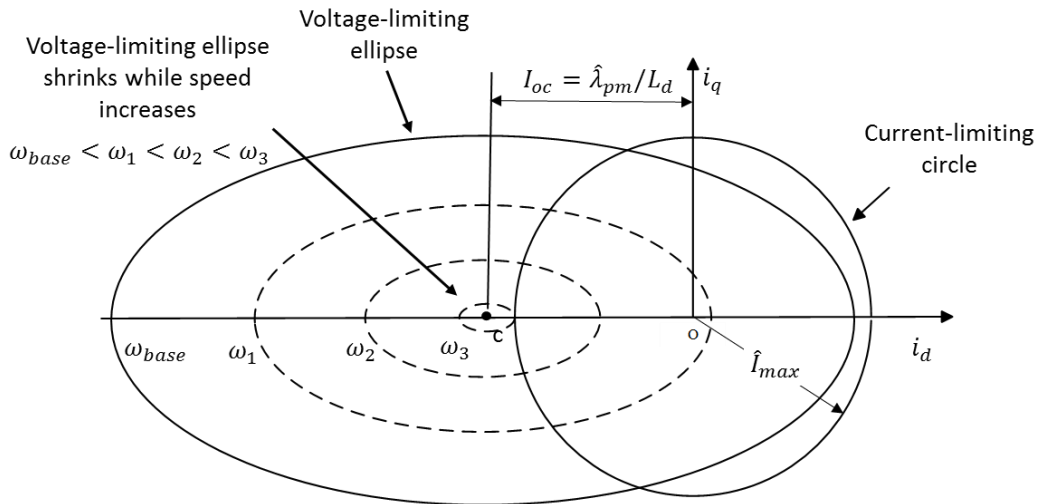
(a) Current-limiting circle and voltage-limiting ellipse for IPM motors
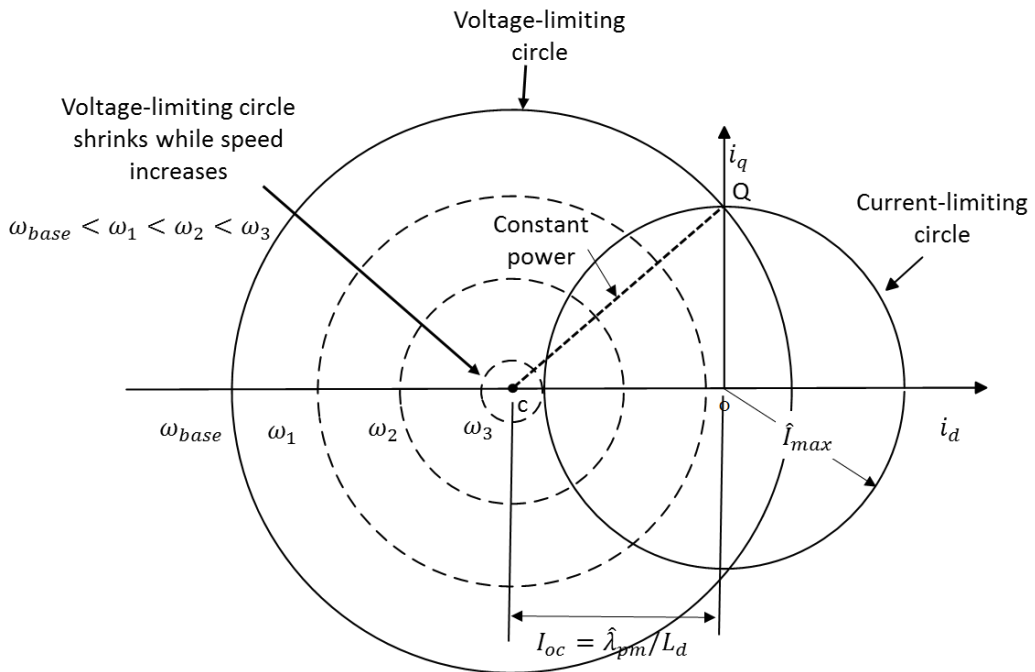
(b) Current-limiting circle and voltage-limiting circle for SPM motors

Figure 2.9: Current-limiting and voltage-limiting characteristics of PMSMs.

While, the voltage limitation is an ellipse for IPM motors in the d-q frame as shown in Figure 2.9 (a), which can be derived form (2.49) as follows:

$$\frac{\left((\lambda_{pm}/L_d)+(i_d)\right)^2}{V_s^2/(\omega_e L_d)^2} + \frac{(i_q)^2}{V_s^2/(\omega_e L_q)^2} = 1 \tag{2.53}$$

where, $\hat{V}_s \leq \hat{V}_{max}$, and $\hat{V}_{max}$ represents the amplitude of the maximum allowable phase voltage. However, for SPM motors, the voltage limitation becomes a circle due to the fact that $L_d = L_q$, as shown in Figure 2.9 (b).

In the FW control category, there are several strategies used for SPM motors and IPM motors. The three commonly used FW control strategies for SPM motors are [49]:

- constant-voltage-constant-power (CVCP) control
- constant-current-constant-power (CCCP) control
- voltage and current limited maximum torque (VCLMT) control

Among the three control strategies above, the VCLMT control is widely used FW control strategy for IPM motors. However, the CVCP control and CCCP control are more suitable for SPM motors.

> **Constant-voltage-constant-power (CVCP) control for SPM motors**

Among the three commonly used FW methods for SPM motors, the CVCP control is the most widely used method because of its simplicity and low requirement for additional hardware in drives. This method keeps a constant voltage and constant power by keeping the current vector following the constant power trajectory which is line QC in Figure 2.9 (b).

As a constant power operation, the rated power is defined as the output power, P_b, at base speed, ω_{base}, as shown in Figure 2.8 (b). Thus, one can obtain the following

for P_b:

$$P_b = \frac{\omega_{base}}{(p/2)} T_{max} \qquad (2.54)$$

where, T_{max} is the maximum torque for the MTPA operation. Since the output power

is constant, the output power, P_b, can be rewritten as follows:

$$P = \frac{\omega_e}{(p/2)} T_e = P_b = \text{constant} \qquad (2.55)$$

From (2.54) and (2.55), one can obtain the following:

$$\omega_e T_e = \omega_{base} T_{max} = \text{constant} \qquad (2.56)$$

For SPM motors, the torque expression as previously obtained in (2.33) is: $T_e =$

$\frac{3}{2}\frac{p}{2}\hat{\lambda}_{pm}i_q$. As aforementioned in the MTPA control section, the maximum torque for

SPM motors can be obtained by keeping $i_q = \hat{I}_s$. Thus, the maximum torque, T_{max}, can

be represented as follows:

$$T_{max} = \frac{3}{2}\frac{p}{2}\lambda_{pm}\hat{I}_s \qquad (2.57)$$

Substituting (2.33) and (2.57) into (2.56) and rearranging, one can obtain the following:

$$\omega_e i_q = \omega_{base}\hat{I}_s = \text{constant} \qquad (2.58)$$

From (2.58), the d-axis voltage equation (2.22) can be rewritten as follows:

$$v_d = -\omega_e L_q i_q = -L_q(\omega_{base}\hat{I}_s) = \text{constant} \qquad (2.59)$$

Since the d-axis voltage is a constant value, in order to keep a constant phase voltage,

the q-axis voltage has to be constant too. Moreover, since the d-axis voltage component

keeps its value at the base speed, the q-axis voltage component should keep its value at

the same base speed as well, which can be represented as follows:

$$v_q = v_{qb} = \text{constant} \qquad (2.60)$$

where, v_{qb} is the q-axis voltage component at the base speed. Due to the zero d-axis current in MTPA operation for SPM motors, v_{qb} can be written as follows:

$$v_{qb} = \omega_{base} \lambda_{pm} \tag{2.61}$$

Substituting (2.23), which is $v_q = \omega_e(\hat{\lambda}_{pm} + L_d i_d)$, and (2.61) into (2.60), one can obtain the following:

$$\omega_e(\lambda_{pm} + L_d i_d) = \omega_{base} \lambda_{pm} = \text{constant} \tag{2.62}$$

From (2.58) and (2.62), the d, q current components for the CVCP control can be obtained as follows:

$$i_d = \frac{\omega_{base}}{\omega_e} \frac{\lambda_{pm}}{L_d} - \frac{\lambda_{pm}}{L_d} \tag{2.63}$$

$$i_q = \frac{\omega_{base}}{\omega_e} \hat{I}_s \tag{2.64}$$

It is obvious that the d, q current components are linearly related to each other. This relationship can be expressed as follows:

$$i_q = \hat{I}_s \frac{L_d}{\lambda_{pm}} i_d + \hat{I}_s \tag{2.65}$$

From (2.65), the CVCP trajectory can be drown as depicted in Figure 2.10, which is the line QC.

It should be noticed that the intersection point, M, between the line QC and the current-limiting circle, represents the boundary of the CVCP control. Any operation along line section MC violates the current limitation. Thus, the valid CVCP control trajectory is within the line QM in Figure 2.10.
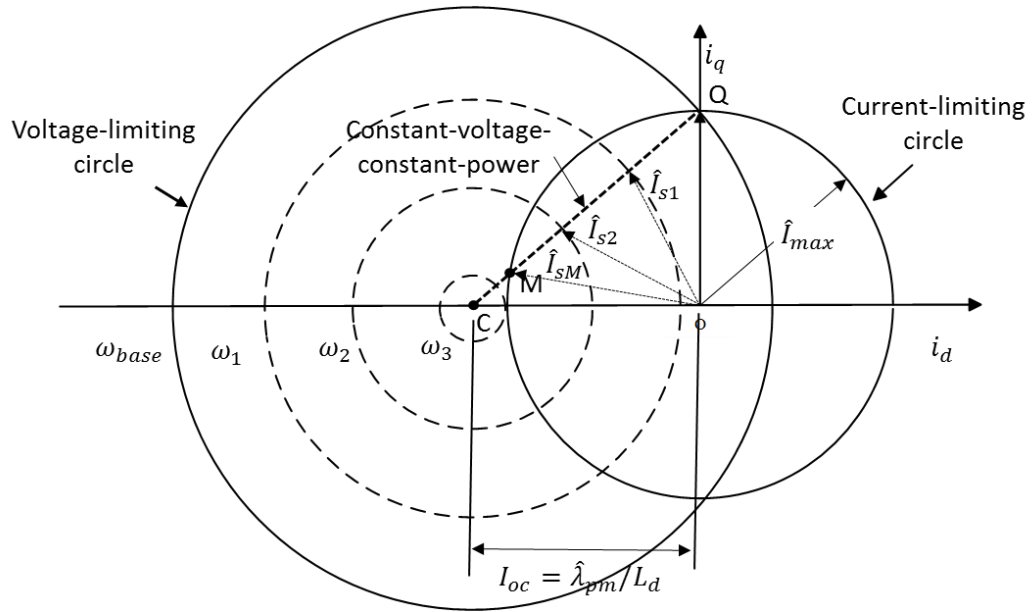
Figure 2.10: Constant-voltage-constant power control of SPM motors.

> **Constant-current-constant-power (CCCP) control for SPM motors**

The CCCP control keeps a constant current and constant power by changing the q-axis voltage component. The control principle of the CCCP control is similar to the CVCP control. However, this method normally requires voltage boost capability of drives to achieve a desired voltage. Thus, it has very limited utilization.

Since the CCCP control has a constant output power as the CVCP control, the CCCP control also has a constant d-axis voltage as was previously derived in (2.59), which can be restated as follows:

$$v_d = -\omega_e L_q i_q = -L_q(\omega_{base}\hat{I}_s) = \text{constant} \tag{2.66}$$

Thus, the q-axis current can be expressed as in (2.64), which yields the following:

$$i_q = \frac{\omega_{base}}{\omega_e}\hat{I}_s \tag{2.67}$$

Since the CCCP control keeps a constant phase current value, by substituting (2.67) into (2.20), the d-axis current can be written as follows:

$$i_d = -\sqrt{\hat{I}_s^2 - i_q^2} = -\frac{\hat{I}_s}{\omega_e}\sqrt{\omega_e^2 - \omega_{base}^2} \qquad (2.68)$$

Substituting (2.68) into the q-axis voltage equation (2.23), one can obtain the following:

$$v_q = \omega_e(\lambda_{pm} + L_d i_d) = \omega_e \lambda_{pm} - L_d \hat{I}_s \sqrt{\omega_e^2 - \omega_{base}^2} \qquad (2.69)$$

As the speed, ω_e, keeps increasing, the q-axis voltage value, v_q, experiences a slight drop and then it keeps increasing as shown in Figure 2.11. Since the d-axis voltage is constant, the phase voltage value in the CCCP control depends on the q-axis voltage component. As shown in Figure 2.12, the current trajectory of the CCCP control follows its current-limiting circle. While, the voltage trajectory changes according to the q-axis voltage.
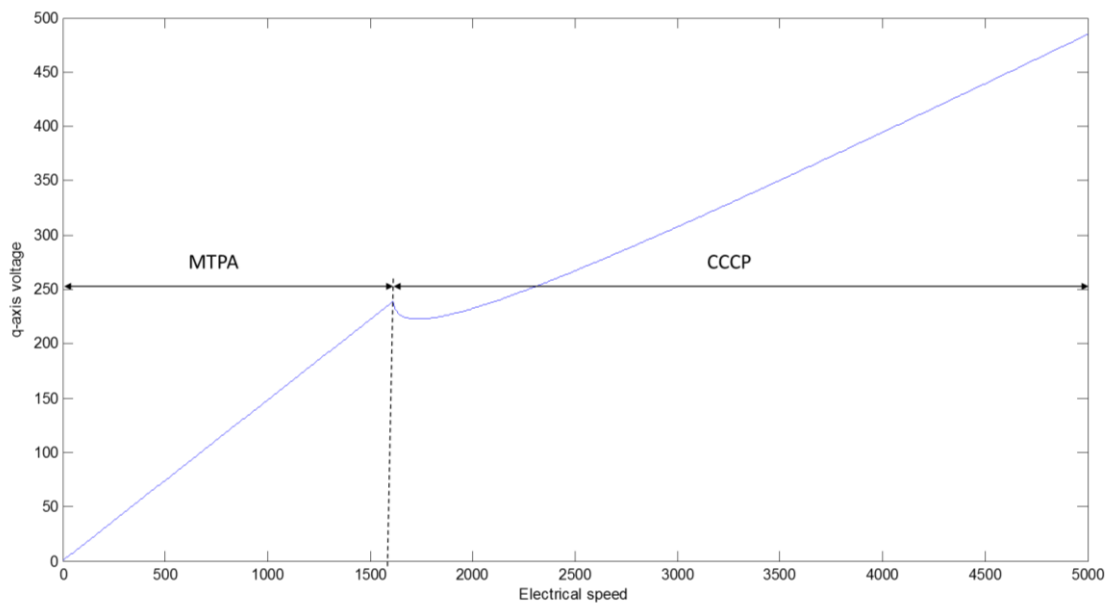
Figure 2.11: The q-axis voltage trajectory of the CCCP control.
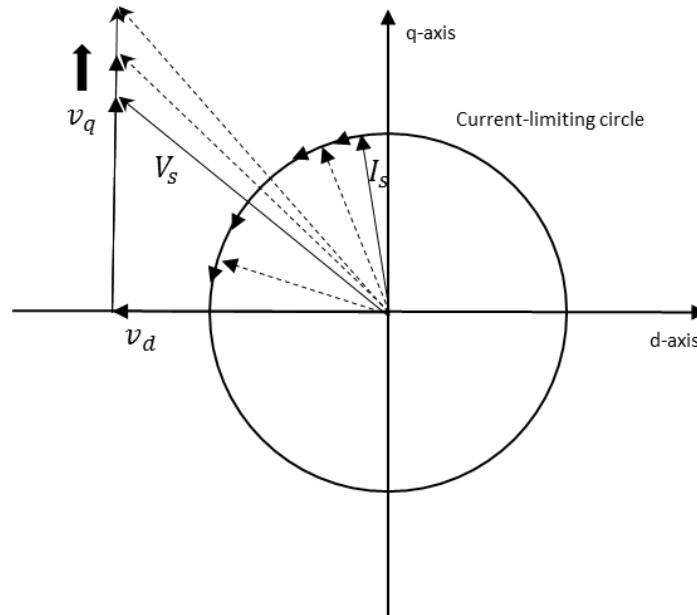
Figure 2.12: Constant-current-constant power control of SPM motors.

> **Voltage and current limited maximum torque (VCLMT) control for IPM motors**

The VCLMT control can be employed for both SPM and IPM motors with the same operation principle. There is only a slight difference in calculations of d, q current components between the two types of PM motors. For simplicity, this section only gives the analysis of the VCLMT control for IPM motors.

As one FW strategy for IPM motors, VCLMT control follows two constraints which are the current-limiting circle and the voltage-limiting ellipse, as shown in Figure 2.9 (a). As the speed increases, with the center of the ellipse remaining the same, the voltage-limiting ellipse becomes smaller and smaller as shown in Figure 2.9 (a). The i_{dm} and i_{qm} for MTPA control cannot satisfy the voltage constraint above the base speed. Therefore, new d, q current components are required to keep the maximum phase voltage, $\hat{V}_{max}$, in the FW region. Such d, q current components can be obtained from the voltage constraint equation (2.53) as follows:

$$(L_q i_q)^2 + (L_d i_d + \lambda_{pm})^2 = \frac{V_{max}^2}{\omega_e^2} \tag{2.70}$$

From the current-limiting circle, Figure 2.9, and (2.52), one can obtain the following:

$$i_q = \sqrt{\hat{I}_{max}^2 - i_d^2} \tag{2.71}$$

By substituting (2.71) into (2.70) and rearranging, a binominal equation of the d-axis

current can be written as follows:

$$(L_d^2 - L_q^2) i_d^2 + 2\lambda_{pm} L_d i_d + \lambda_{pm}^2 + L_q^2 \hat{I}_{max}^2 - (V_{max}^2 / \omega_e^2) = 0 \tag{2.72}$$

From (2.72), two solution can be obtained as follows:

$$i_{d1} = \frac{-\lambda_{pm} L_d + \sqrt{(\lambda_{pm} L_d)^2 - (L_d^2 - L_q^2)\left(\lambda_{pm}^2 + L_q^2 \hat{I}_{max}^2 - (V_{max} / \omega_e)^2\right)}}{(L_q^2 - L_q^2)} < 0$$

$$i_{d2} = \frac{-\lambda_{pm} L_d - \sqrt{(\lambda_{pm} L_d)^2 - (L_d^2 - L_q^2)\left(\lambda_{pm}^2 + L_q^2 \hat{I}_{max}^2 - (V_{max} / \omega_e)^2\right)}}{(L_q^2 - L_q^2)} > 0 \tag{2.73}$$

Since the demagnetizing current should be a negative value, the root i_{d1} in (2.73) is the

expected useful solution for the FW operation. From the above analysis of the VCLMT

strategy, the d- and q-axis currents for the FW control of IPM motors can be expressed

as follows:

$$i_{d,VCL} = \frac{-\lambda_{pm} L_d + \sqrt{(\lambda_{pm} L_d)^2 - (L_d^2 - L_q^2)\left(\lambda_{pm}^2 + L_q^2 \hat{I}_{max}^2 - (V_{max} / \omega_e)^2\right)}}{(L_q^2 - L_q^2)} \tag{2.74}$$

$$i_{q,VCL} = \sqrt{\hat{I}_{max}^2 - i_{d,VCL}^2} \tag{2.75}$$

For the whole speed range of operation, a recommended control strategy for

IPM motor is the combination of the MTPA control and FW control. The optimal

current vector trajectory for the MTPA control and the FW control is shown in Figure

2.13. This strategy implements the MTPA control in the low speed region, which is

region OA as shown in Figure 2.13, until the base speed. Then, it employs the FW

control at region AB, when the speed is above base speed.
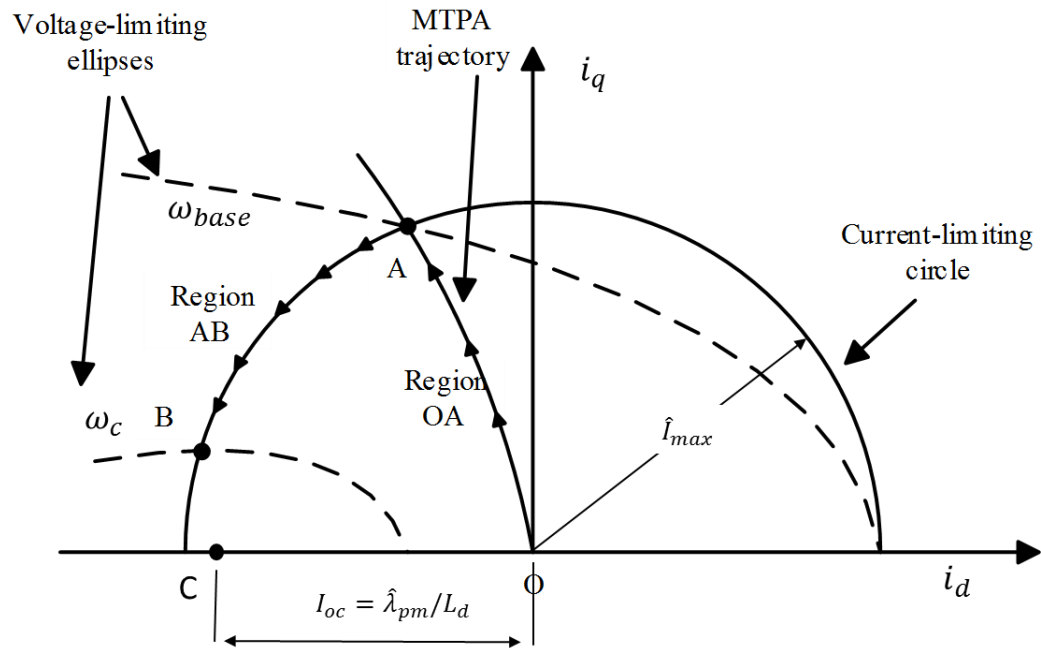
(a) $\hat{\lambda}_{pm}/L_d < \hat{I}_{max}$
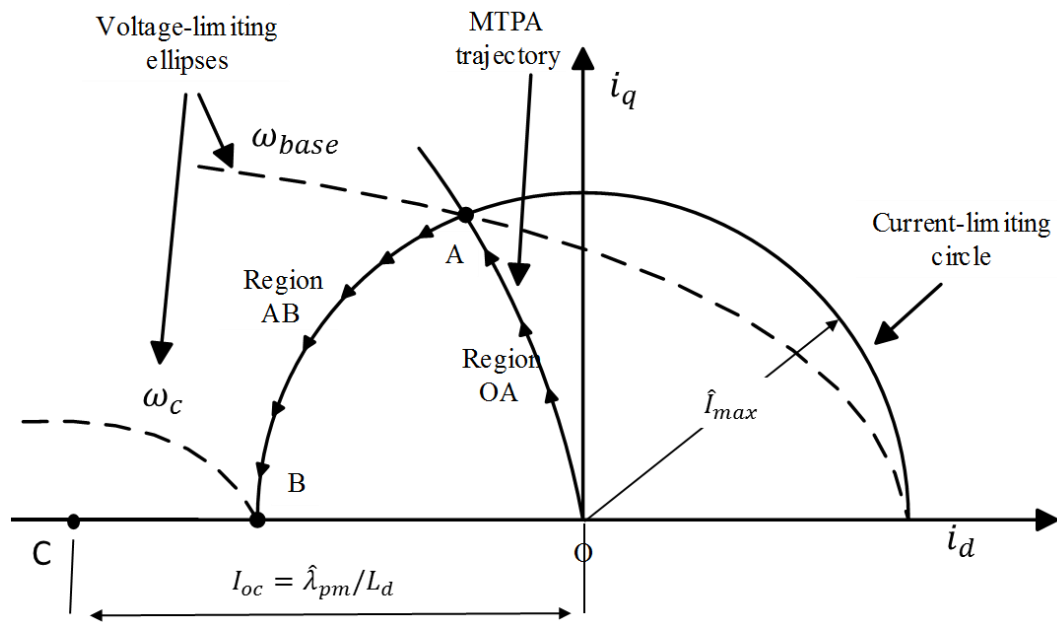
(b) $\hat{\lambda}_{pm}/L_d > \hat{I}_{max}$

Figure 2.13: Optimum current vector trajectory in the d, q frame for IPM motors.

From the voltage ellipse equation (2.53), the center of the voltage ellipse is located at a point C $(-\hat{\lambda}_{pm}/L_d, 0)$, as shown in Figure 2.9 and 2.13. Notice that λ_{pm}/L_d is usually defined as the short-circuit current. Once the maximum inverter current, I_{max}, becomes equal to or larger than the short-circuit current, the permanent magnet can be fully demagnetized. In another word, the permanent magnet flux, λ_{pm}, can be fully cancelled/eliminated.

With a large size inverter which has $\hat{I}_{max} > (\hat{\lambda}_{pm}/L_d)$ as shown in Figure 2.13 (a), the lossless machine is capable of attaining infinite speed. Above a certain speed at point B, the maximum torque becomes only voltage limited. Then the current trajectory follows the voltage ellipse rather than the current circle for the maximum torque.

With a small size inverter which has $\hat{I}_{max} < (\hat{\lambda}_{pm}/L_d)$ as shown in Figure 2.13 (b), the maximum speed at point B is finite. The maximum torque can be found at the intersection between the voltage-limiting ellipse for that speed and the current-limiting circle. In most design cases, we only have $\hat{I}_{max} < (\hat{\lambda}_{pm}/L_d)$, which means that the permanent magnet is too strong to be fully demagnetized.

Since the more demagnetizing current in the negative d-axis direction the deeper the flux weakening, the maximum speed of the VCLMT control can be obtained by substituting $i_d = -\hat{I}_{max}$ and $i_q = 0$ into (2.70) as follows:

$$(-L_d \hat{I}_{max} + \lambda_{pm})^2 = \frac{V_{max}^2}{\omega_e^2} \tag{2.76}$$

or

$$\omega_e = \frac{V_{max}/L_d}{(\lambda_{pm}/L_d - \hat{I}_{max})} = \omega_{max} \tag{2.77}$$

For a large size inverter, the denominator in (2.77) could be zero. Therefore, the theoretical speed is infinite.

Chapter 3

Z-Source Inverters

Inverters are absolutely necessary components on realizing any modern ac motor control applications. This chapter presents details of a unique inverter which is the Z-source inverter, including its topologies, operation principles and control methods.

3.1 Introduction

The process of converting dc to ac power is called inversion and it is the inverter which creates the variable frequency from the dc source which is used to drive an ac motor at variable speed [51]. As a new invention, the Z-source inverter (ZSI) was first proposed by [32]. The most significant characteristic of such ZSI is its ac voltage boost capability, which is not available in conventional inverters. In many applications such as photovoltaic power generation, electric/hybrid vehicles, machine tools, etc., the voltage was boosted by additional dc/dc converters or transformers which can now be replaced by ZSIs. The ZSI also has the same function as conventional inverters. Therefore, such inverter topology can be used in various industrial applications.

The ZSI, shown in Fig. 3.1, is a buck-boost converter which employs a unique impedance network to couple the inverter main circuit to the dc link/ dc bus. The name "Z-source" also stems from this impedance network preceding the inverter switches bridge. Figure 3.2 shows the conventional three-phase voltage-source inverter structure, which uses a dc voltage source supported by a relatively large capacitor to feed the three-phase bridge. Compared to the conventional inverter topology in Figure 3.2, the ZSI has an extra impedance network which consists of two inductors and two capacitors.
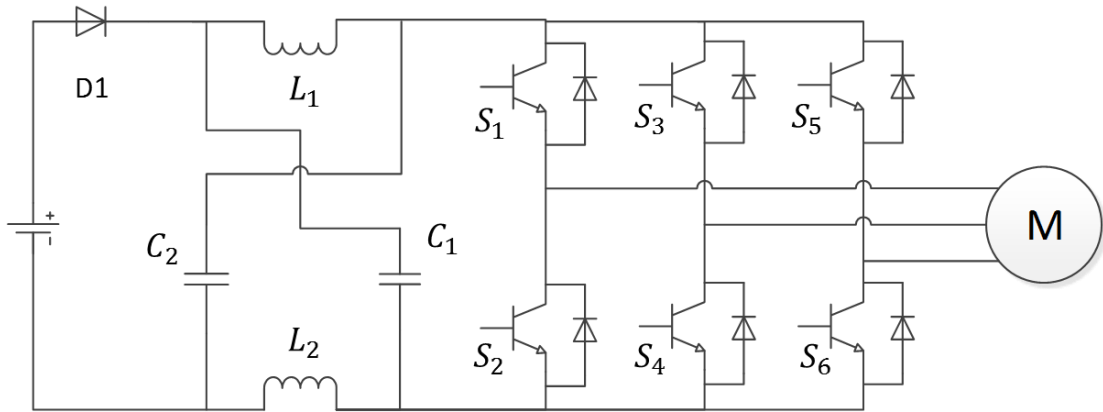
Figure 3.1: Voltage fed Z-source inverter.
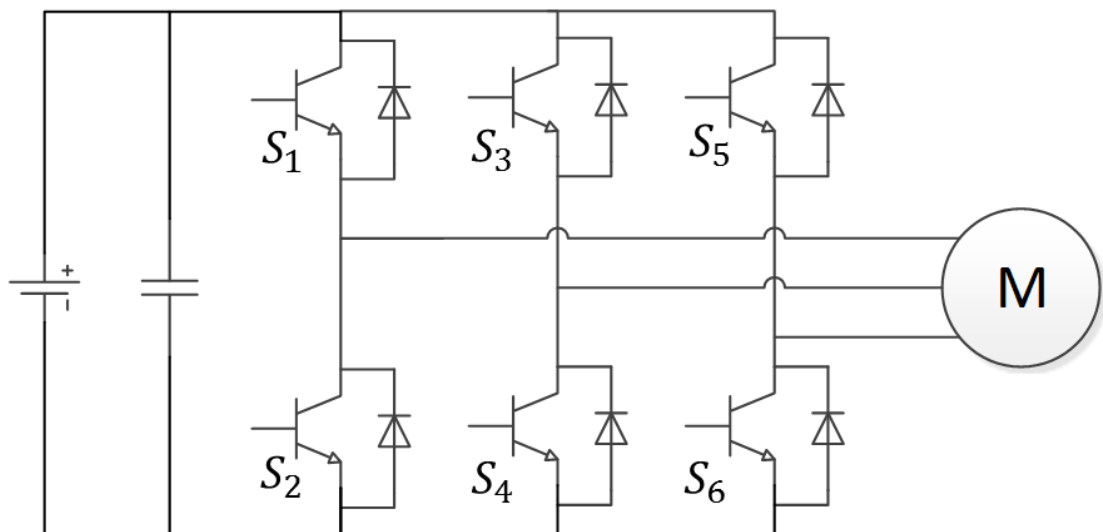
Figure 3.2: Traditional voltage-source inverter.

The unique feature of the ZSI is that the output ac voltage in theory can be any nonnegative value regardless of the dc source voltage. Such an inverter has many other advantages that can be listed as follows [32, 36]:

- Provide ride-through during voltage sags.

- Improve power factor.

- Eliminate dead time and reduce harmonics in current waveforms and common-mode voltage.

- The shoot-through switching state will no more cause catastrophic damage.

Compared to conventional inverters, the major drawback of the ZSI is the impedance network which requires extra cost and large space due to the associated bulky inductors and capacitors. However, compared to conventional two-stage power conversions for boosting ac voltage, the ZSI has fewer semiconductor switches, lower price, and higher efficiency [55]. For instance, Figure 3.3 shows the traditional two-stage voltage boost structure for fuel-cell applications. The dc-dc boost converter and the three phase inverter can be replaced by a ZSI as shown in Figure 3.4.
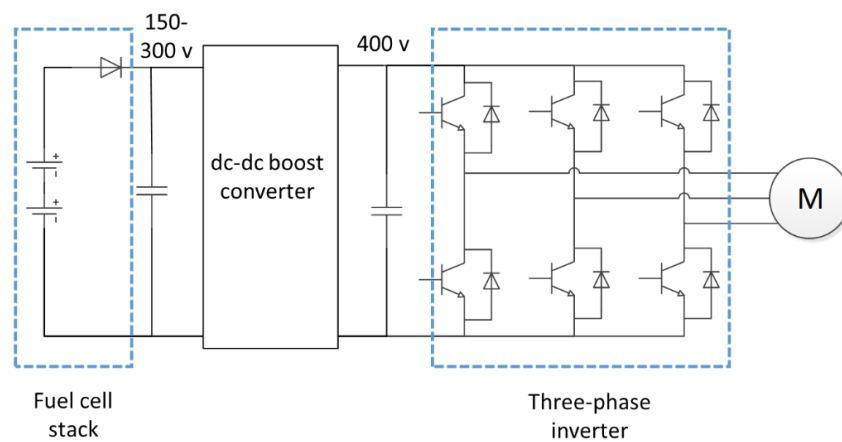
Figure 3.3: Traditional two-stage power conversion for fuel-cell applications.
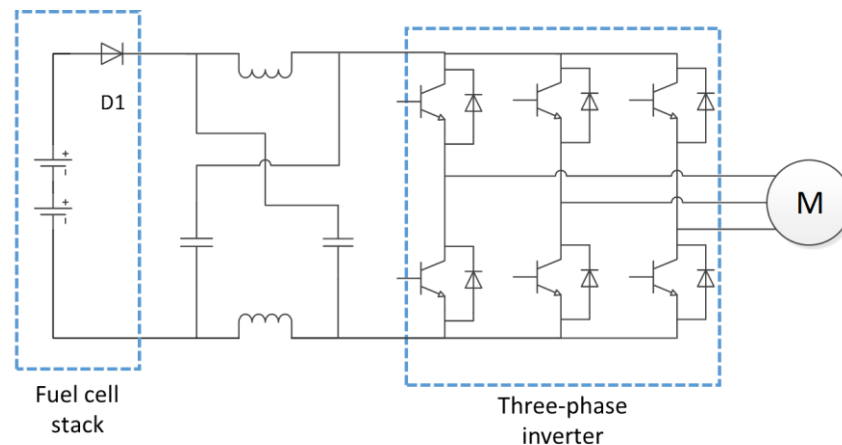
Figure 3.4: Z-source inverter for fuel-cell applications.

Conventional voltage source inverters (VSIs) and current source inverters (CSIs) suffer from similar problems when used in many applications. Specifically, VSIs must have a dc bus voltage which is greater than the peak value of the line-to-line output voltage of such inverters. Similarly, the input voltage of CSIs has to be less than the output voltage. Thus, they are either buck converters or boost converters. However, the output voltage of such converters can be varied as desired by coupling the Z-impedance network with conventional VSI or CSI topologies. Since the ZSI was introduced in 2003, many improved topologies based on the original ZSI design have been developed and presented. In order to achieve bidirectional power flow, the diode, D1, shown in Figure 3.1 can be replaced with a bidirectionally-conducting unidirectionally-blocking switch. In addition to the voltage fed ZSI shown in Figure 3.1, a current fed ZSI is also feasible, as shown in Figure 3.5 [56]. To reduce the passive component ratings, other topologies such as quasi-Z-source inverters (qZSIs) were introduced as shown in Figure 3.6 (a through d) [33].
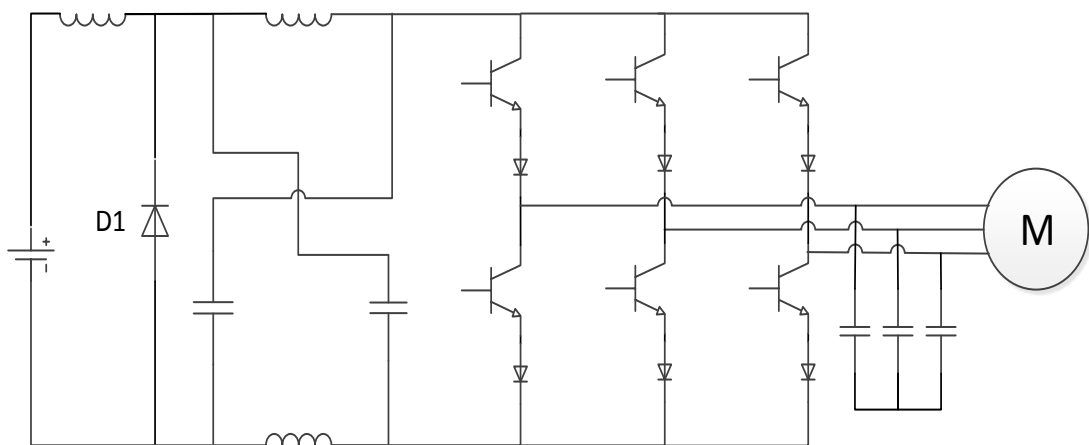
Figure 3.5: Current source Z-source inverter.
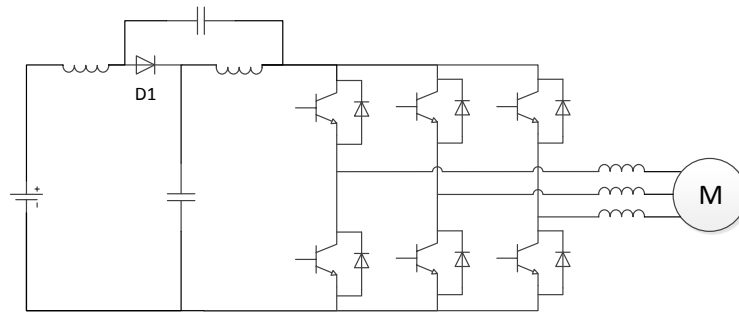
(a) Voltage source Qzsi with continuous input current
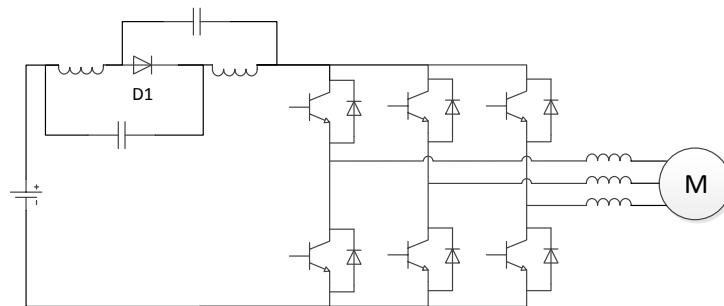
(b) Voltage source Qzsi with discontinuous input current
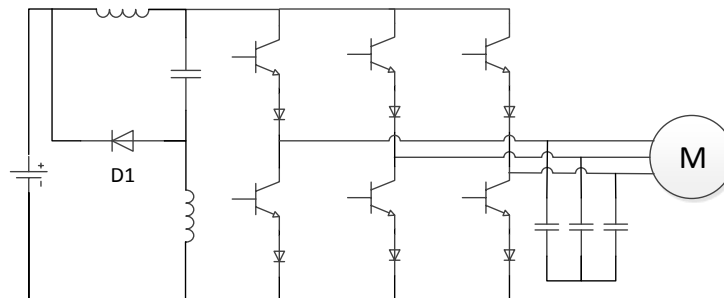
(c) Current source Qzsi with discontinuous input current
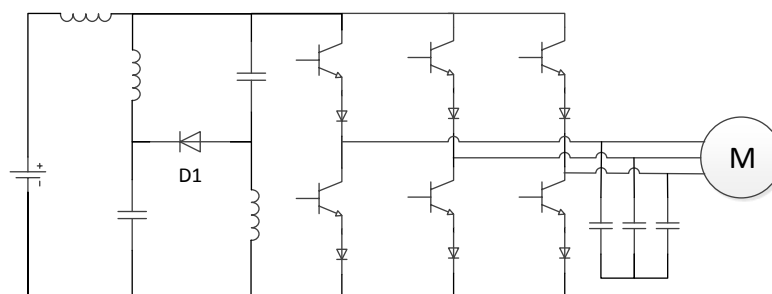
(d) Current source Qzsi with continuous input current

Figure 3.6: Quasi-Z-source inverters.

The Z-source concept can be applied to all circuits of dc-to-ac, ac-to-dc, ac-to-ac, and dc-to-dc power conversion. The Z-impedance network can be coupled with many conventional topologies, such as Z-source matrix converters [57, 58], Z-source multilevel inverters [59, 60], Z-source rectifiers [61, 62], etc. Therefore, the Z-source concept can be used in various industrial applications, such as photovoltaic power generation systems [63], adjustable speed drives [36], dc power supplies [64], etc. In order to describe the operating principle and control methods for the Z-source converters, this chapter focuses on the analysis of the original ZSI.

3.2 Operation Principle and Passive Components Design

The essential operation principle of a ZSI is similar to a dc-to-dc boost converter which utilizes a charged inductor, L, to boost the output voltage and utilizes a capacitor, C, to sustain a constant output voltage as shown in Figure 3.7. Notice the reversal of the voltage polarity across the inductor from the charging mode to the active mode in Figure 3.7.

(a) Charging mode

(b) Active mode
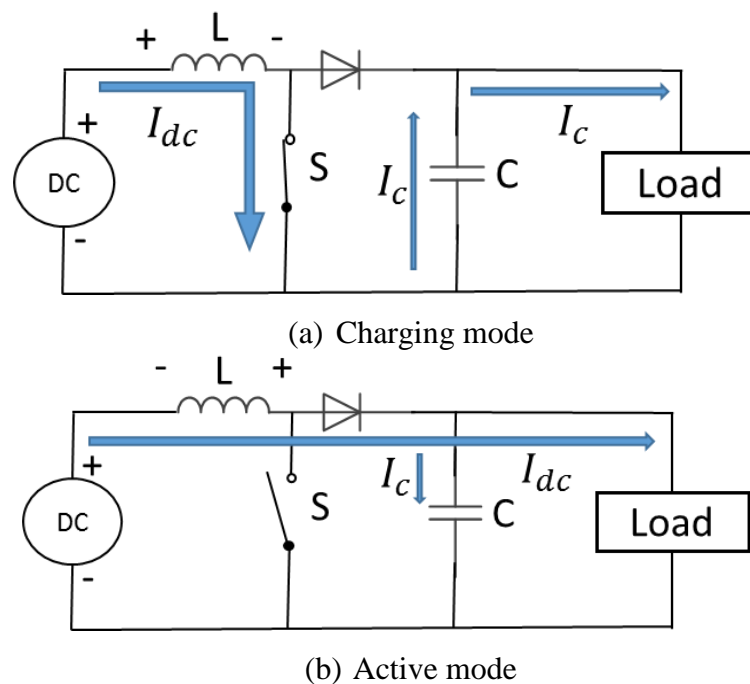
Figure 3.7: A dc-dc boost converter.

In the charging mode of a dc-dc converter as shown in Figure 3.7 (a), the inductor current keeps increasing and the diode is not conducting. The output voltage across the load is sustained by the capacitor, C. In the active mode as shown in Figure 3.7 (b), once the switch, S, is opened, the inductor, L, starts to discharge and the diode is conducting. Once again, notice the reversal of voltage polarity across the inductor. Since the inductor current is on the decline in the discharge operation, the voltage across the inductor changes polarity to the direction that supports the dc current, I_{dc}. Therefore, the output voltage/capacitor voltage become higher than the dc supply voltage. Suppose the capacitor is relatively large and hence, its voltage is sustained as in the active mode, the output voltage of the dc-to-dc boost converter can be seen as a constant which is higher than the dc supply voltage.

From the analysis of the traditional dc-to-dc boost converter, a charged inductor is required to achieve the voltage boost capability. Therefore, a special switching mode on the inverter bridge is employed, which is turning on both the upper switch and the lower switch in one phase leg at the same time as in a shoot-through switching mode. Once the two switches in one phase leg are turned on, the load is shorted and the two inductors in the ZSI start to be charged. This shoot-through zero state (shoot-through state) is forbidden in traditional voltage source inverters, because it would cause a near total short circuit across the dc bus.

Since the shoot-through zero state is required for ZSIs, the total permissible switching states are nine for a three-phase ZSI, which includes six active states, two zero states, and one shoot-through zero state. While, conventional three-phase voltage source inverters only have eight permissible switching states. Table 3.1 presents the nine switching states of a ZSI shown in Figure 3.8. Notice that the shoot-through zero state can be generated by seven different ways: shoot-through via one phase leg,

combinations of any two phase legs, and all three phase legs. For practical applications,

shoot-through via all three phase legs yields the least loss on the six switching devices.

State Switch	Active state						Zero state		Shoot-through zero state (generated by seven different ways)						
S1	1	1	0	0	0	1	0	1	1	0	0	1	1	0	1
S2	0	0	1	1	1	0	1	0	1	0	0	1	1	0	1
S3	0	1	1	1	0	0	0	1	0	1	0	1	0	1	1
S4	1	0	0	0	1	1	1	0	0	1	0	1	0	1	1
S5	0	0	0	1	1	1	0	1	0	0	1	0	1	1	1
S6	1	1	1	0	0	0	1	0	0	0	1	0	1	1	1

Table 3.1: Nine permissible switching states of ZSIs (1=closed, 0=open.).
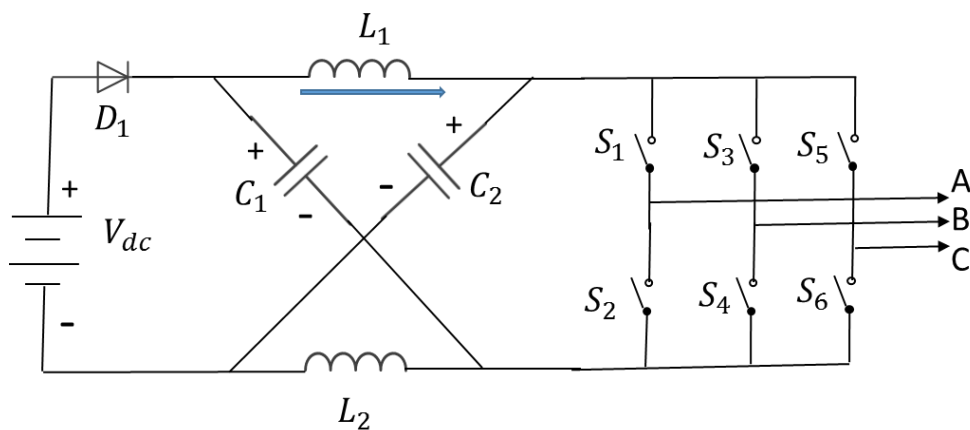
Figure 3.8: A three-phase ZSI.

Assuming that the inductors, L_1 and L_2, have the same inductance, and the

capacitors, C_1 and C_2, have the same capacitance, the Z-source network becomes

symmetrical. Figure 3.9 presents the equivalent circuits of the ZSI in the three different

states, namely the active, the zero, the shoot-through zero states of Table 3.1. From the

symmetry and the equivalent circuits of Figure 3.9, one can obtain the following:

$$V_{c1} = V_{c2} \qquad V_{l1} = V_{l2} \qquad (3.1)$$
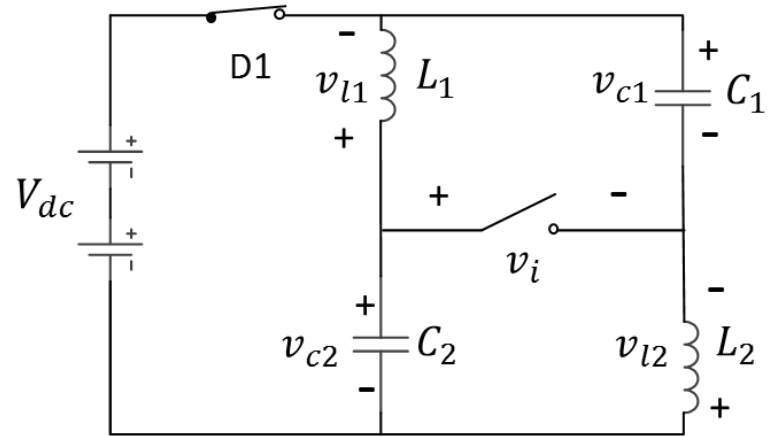
(a) Zero state
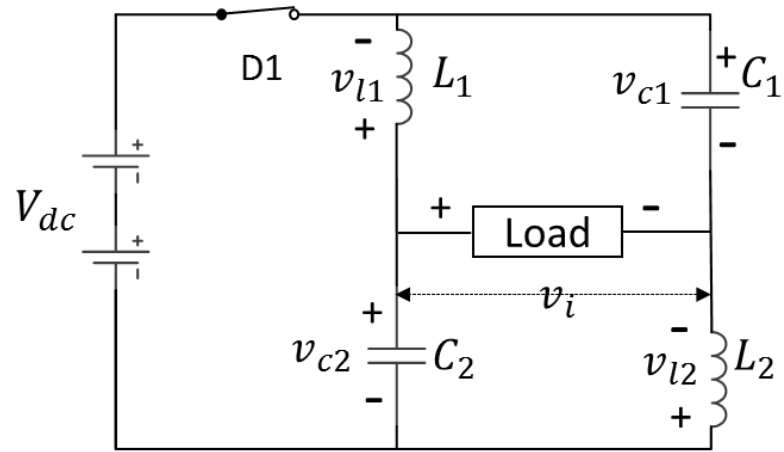
(b) Active state
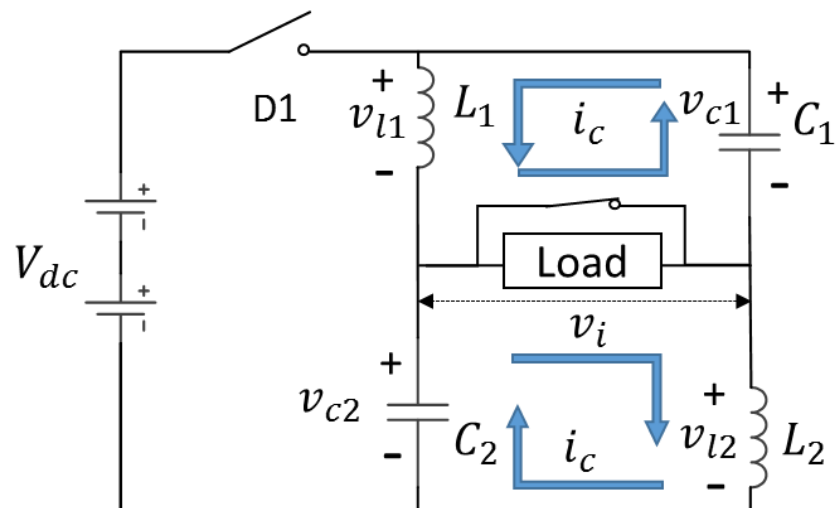
(c) Shoot-through zero state

Figure 3.9: Equivalent circuits of the ZSI.

In the zero state, shown in Figure 3.9 (a), the ZSI works in the open circuit mode. The output current of the inverter during the zero state will drop to zero in the steady state. Therefore, the current through the two inductors, L_1 and L_2, will drops to zero as well, which means the inductors are discharging during the zero state. It also indicates that the capacitors, C_1 and C_2, will be charged during the zero state. The diode, D_1, will keep conducting until the current drops to zero, which means that the capacitors are fully charged and achieve their peak voltage value at that time.

In the active state as shown in Figure 3.9 (b), the diode, D_1, is conducting and the two inductors, L_1 and L_2, keep discharging. Since the current through the two inductors keeps decreasing during their discharging, the two inductors become voltage sources, v_{l1} and v_{l2}, to support the current through them. Therefore, one can obtain the output voltage of the Z-impedance network, v_i, which is also the voltage across the inverter bridge as follows:

$$v_i = V_{dc} + v_{l1} + v_{l2} \tag{3.2}$$

From (3.2), it is obvious that the output voltage during the active state becomes higher than the dc bus voltage. Due to the symmetry of the Z-impedance network, the voltage across the passive components can be obtained as follows:

$$v_{l1} = v_{l2} = v_{la} \qquad v_{c1} = v_{c2} = v_{ca} \tag{3.3}$$

where, v_{la} and v_{ca} are voltages across the inductors and capacitors during the active state of the ZSI, respectively. From Kirchhoff's voltage law, the relationship between the inductor voltage, v_{la}, and the capacitor voltage, v_{ca}, can be written as follows:

$$v_{la} = v_{ca} - V_{dc} \tag{3.4}$$

By substituting (3.3) and (3.4) into (3.2), one can obtain the following:

$$v_i = V_{dc} + 2v_{la} = 2v_{ca} - V_{dc} \tag{3.5}$$

In the shoot-through zero state as shown in Figure 3.9 I, the diode, D_1, is not

conducting and the two inductors, L_1 and L_2, keep charging by the two capacitors, C_1 and C_2 respectively. Figure 3.9 I also shows two current loops that indicate the direction of the power transmission. If only one phase-leg is shorted, the current through this phase-leg is two times the charging current, i_c, in the shoot-through zero state. However, the voltage across the inverter bridge, v_i, is zero, which can be expressed as follows:

$$v_i = 0 \tag{3.6}$$

Due to the symmetry, one can obtain the follows:

$$V_{l1} = V_{c1} \qquad V_{l2} = V_{c2} \qquad V_{l1} = V_{l2} = V_{ls} \qquad V_{c1} = V_{c2} = V_{cs} \tag{3.7}$$

where, v_{ls} and v_{cs} are voltages across the inductors and capacitors during the shoot-through zero state of the ZSI, respectively.

Assuming the two capacitors, C_1 and C_2, are large enough to sustain a constant voltage during a switching cycle, the voltages, v_{ca} and v_{cs}, across the two capacitors in different states can be rewritten as follows:

$$v_{ca} = v_{cs} = V_c \tag{3.8}$$

The average voltage of the inductors, $\langle v_l \rangle$, over one switching period, T, should be zero in the steady state. Thus, one can write the following:

$$\langle v_l \rangle = \frac{T_s \cdot v_{ls} + T_a \cdot v_{la}}{T} = 0 \tag{3.9}$$

where, T_s and T_a, are the time intervals for the shoot-through zero state and the active state during one switching period, respectively. Notice that the zero state is not considered during the steady state operation. Therefore, the switching period, T, can be expressed as follows:

$$T = T_s + T_a \tag{3.10}$$

By substituting (3.8) into (3.4) and (3.7), one can obtain the following:

$$v_{la} = V_c - V_{dc} \qquad v_{ls} = V_c \tag{3.11}$$

Then by substituting (3.11) into (3.9), the equation (3.9) can be rewritten as follows:

$$\langle v_l \rangle = \frac{T_s \cdot V_{dc} + T_a \cdot (V_c - V_{dc})}{T} = 0 \tag{3.12}$$

or

$$\frac{V_c}{V_{dc}} = \frac{T_a}{T_a - T_s} \tag{3.13}$$

Similarly, the average dc-link voltage across the inverter bridge, $\langle v_i \rangle$, can be obtained as follows:

$$\langle v_i \rangle = \frac{T_s \cdot \langle v_{is} \rangle + T_a \cdot \langle v_{ia} \rangle}{T} \tag{3.14}$$

where, $\langle v_{is} \rangle$ is the average voltage across the inverter bridge during the shoot-through zero state and $\langle v_{ia} \rangle$ is the average voltage across inverter bridge during the active state. From (3.5), (3.6) and (3.8), one can obtain the following:

$$\langle v_{is} \rangle = v_{is} = 0 \qquad \langle v_{ia} \rangle = 2v_{ca} - V_{dc} = 2V_c - V_{dc} \tag{3.15}$$

By substituting (3.15) into (3.14), the average dc-link voltage across the inverter bridge, $\langle v_i \rangle$, can be rewritten as follows:

$$\langle v_i \rangle = \frac{T_s \cdot 0 + T_a \cdot (2V_c - V_{dc})}{T} = \frac{T_a \cdot (2V_c - V_{dc})}{T} \tag{3.16}$$

By substituting (3.10) and (3.13) into (3.16), one obtains the following:

$$\langle v_i \rangle = \frac{T_a \cdot \left(2V_c - \dfrac{T_a - T_s}{T_a} V_c \right)}{T_a + T_s} = V_c = \frac{T_a}{T_a - T_s} V_{dc} \tag{3.17}$$

Since $T_a - T_s < T_a$, it is obvious that the average voltage across the inverter bridge, $\langle v_i \rangle$, is higher than the dc supply voltage, V_{dc}. From (3.15), the peak value of v_i is v_{ia}. By substituting (3.13) into the v_{ia} expression in (3.15), one can rewrite the peak value of v_i as follows:

$$\hat{v}_i = v_{ia} = 2V_c - V_{dc} = 2\frac{T_a}{T_a - T_s}V_{dc} - V_{dc} = \frac{T_a + T_s}{T_a - T_s}V_{dc} = B \cdot V_{dc} \qquad (3.18)$$

where, B is defined as the boost factor which is resulting from the shoot-through zero state. Since $T = T_s + T_a$, the boost factor, B, can be simplified as follows:

$$B = \frac{T}{T_a - T_s} = \frac{1}{1 - 2\dfrac{T_s}{T}} \geq 1 \qquad (3.19)$$

Notice that if the shoot-through time, T_s, is zero, which means no shoot-through zero state, from (3.17), the average voltage across the inverter bridge, $\langle v_i \rangle$, is equal to the dc supply voltage, V_{dc}. Moreover, from (3.13), the two capacitors will have the same voltage as the dc supply. Once the shoot-through time, T_s, is set to zero, the boost factor, B, is equal to 1, which can be obtained from (3.19). Therefore, in such a condition, the inverter works as a conventional three-phase full-bridge inverter without the voltage boost capability. It should also be noticed that according to [65] the shoot-though duty ratio, T_s/T, cannot exceed 0.5 or the system becomes unstable. Therefore, the shoot-through duty ratio, T_s/T, ranges from 0 to 0.5 and the boost factor, B, is from 1 to infinity.

The peak voltage across the inverter bridge, $\hat{v}_i$, is the equivalent dc-link voltage of the inverter. The output peak phase voltage, $\hat{v}_a$, from the inverter can be expressed as follows:

$$\hat{v}_a = M \cdot \frac{\hat{v}_i}{2} \qquad (3.20)$$

where, M, is the modulation index. By substituting (3.18) into (3.20), one can obtain the following:

$$\hat{v}_a = M \cdot B \cdot \frac{V_{dc}}{2} = G \cdot \frac{V_{dc}}{2} \qquad (3.21)$$

where, G is defined as the voltage gain, which has a range that $0 < G < \infty$.

In practical applications, the two capacitors in the Z-impedance network are limited by cost and space. Therefore, they cannot be too large and the voltage ripples have to be considered. The actual capacitor voltage waveform and inductor current waveform during the active state and the shoot-through state can be schematically presented as shown in Figure 3.10 [66].
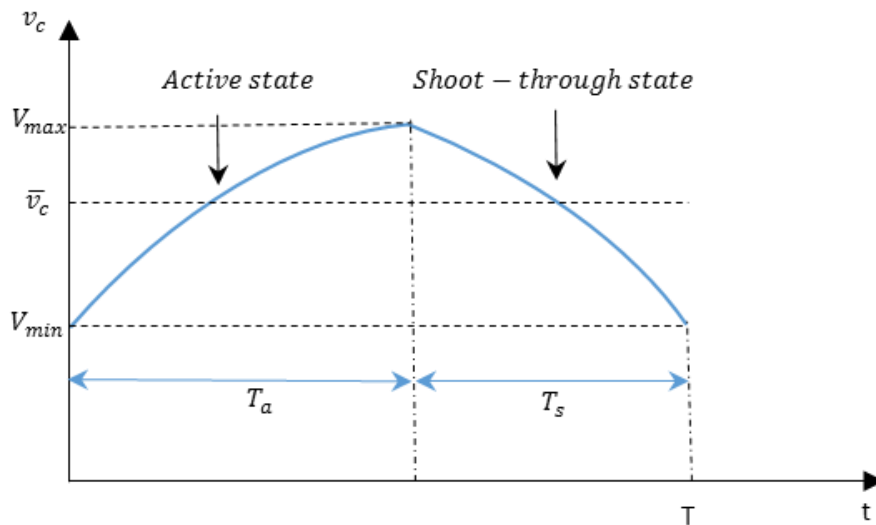
(a) Capacitor voltage
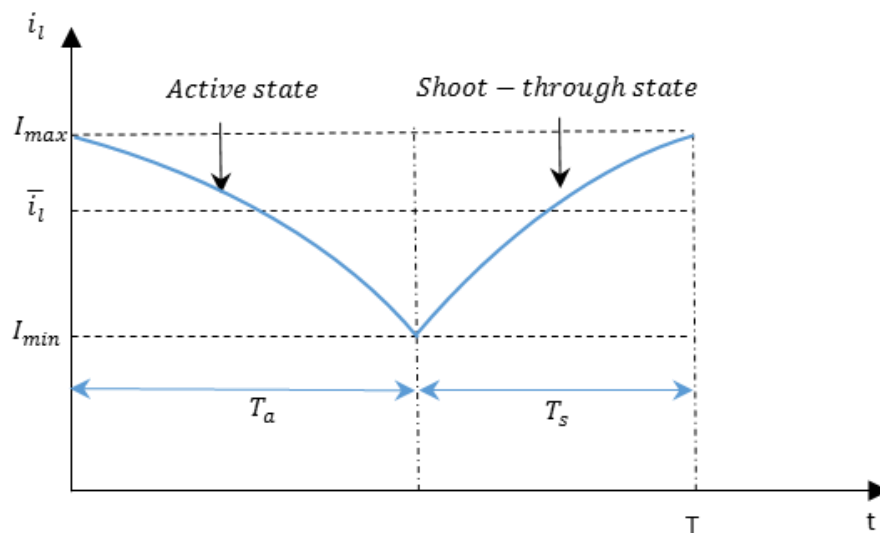
(b) Inductor current

Figure 3.10: Steady state waveforms of Z-network passive components.

In order to design the capacitors and inductors for the Z-impedance network, a linear approximation to the voltage and current waveforms of Figure 3.10 can be represented as shown in Figure 3.11.
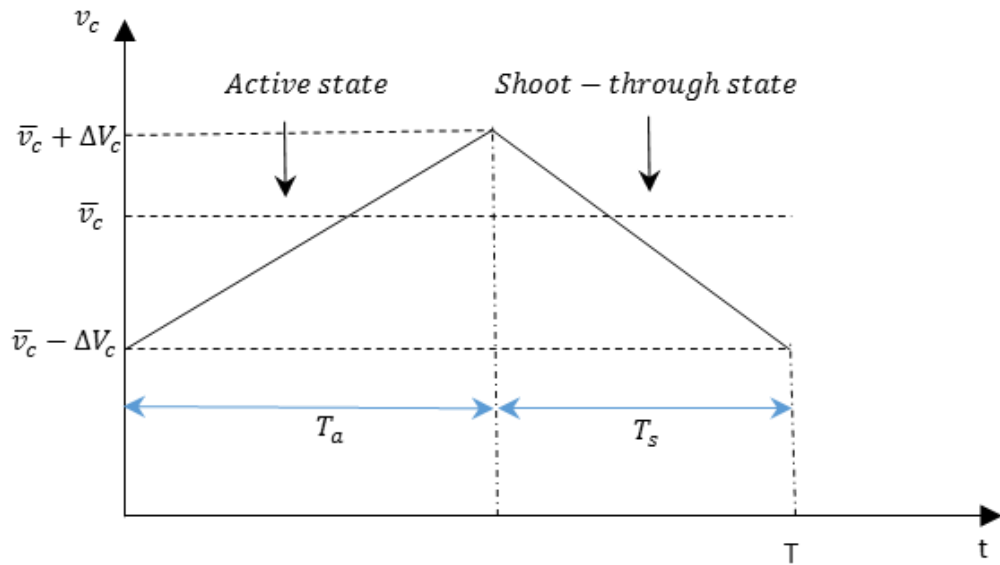
(a) Capacitor voltage
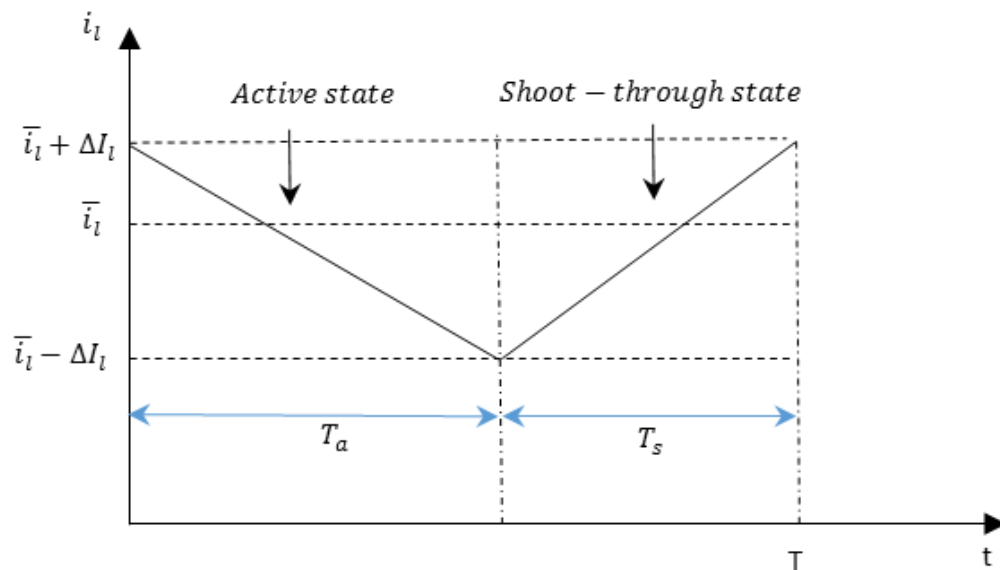
(b) Inductor current

Figure 3.11: A linear approach for capacitor voltage and inductor current.

Accordingly, the voltage equation of the inductors and the current equation of the capacitors can be expressed as follows:

$$v_l = L\frac{di_l}{dt} \qquad\qquad i_c = C\frac{dv_c}{dt} \tag{3.22}$$

where, L, is the inductance value, C, is the capacitance value, i_l and i_c are inductor current and capacitor current, respectively. With linear variations of the waveforms shown in Figure 3.11, (3.22) can be rewritten as follows:

$$\langle v_l \rangle = L\frac{\Delta I_l}{\Delta t} \qquad\qquad \langle i_c \rangle = C\frac{\Delta V_c}{\Delta t} \tag{3.23}$$

Considering the shoot-through state which has $\Delta t = T_s$, the inductance and capacitance values can be obtained from (3.23) as follows:

$$L = (\langle v_{ls} \rangle T_s)/(2\Delta I_l) \qquad C = (\langle i_{cs} \rangle T_s)/(2\Delta V_c) \tag{3.24}$$

where, $\langle v_{ls} \rangle$ is the average inductor voltage during the shoot-through state, and $\langle i_{cs} \rangle$ is the average capacitor current during the shoot-through state. From (3.7) and (3.13), one can obtain the following:

$$\langle v_{ls} \rangle = V_c = \frac{T_a}{T_a - T_s} V_{dc} \tag{3.25}$$

Since the average capacitor current over a complete switching cycle in the steady state is zero, the average capacitor current can be presented as follows:

$$\langle i_c \rangle = \frac{T_s \cdot \langle i_{cs} \rangle + T_a \cdot \langle i_{ca} \rangle}{T} = 0 \tag{3.26}$$

where, $\langle i_{cs} \rangle$ is the average capacitor current in the shoot-through state and $\langle i_{ca} \rangle$ is the average capacitor current in the active state. Assuming the average inductor current can be held to a constant value, $\langle i_l \rangle$, one can obtain the following from Figure 3.9:

$$\langle i_{cs} \rangle = \langle i_l \rangle \qquad\qquad \langle i_{ca} \rangle = I_{out} - \langle i_l \rangle \tag{3.27}$$

where, I_{out} is the output current to the inverter bridge during the active state. By substituting (3.27) into (3.26) and rearranging, the average inductor current, $\langle i_l \rangle$, can

be obtained as follows:

$$\langle i_l \rangle = \frac{T_a}{T_a - T_s} I_{out} = \langle i_{cs} \rangle \tag{3.28}$$

Substituting (3.25) and (3.28) into (3.24), the inductance and capacitance can be rewritten as follows:

$$L = (\frac{T_a}{T_a - T_s} V_{dc} \cdot T_s) / (2\Delta I_l) \qquad C = (\frac{T_a}{T_a - T_s} I_{out} T_s) / (2\Delta V_c) \tag{3.29}$$

or

$$L = (\frac{1 - T_s / T}{1 - 2T_s / T} V_{dc} \cdot T_s) / (2\Delta I_l) \quad C = (\frac{1 - T_s / T}{1 - 2T_s / T} I_{out} T_s) / (2\Delta V_c) \tag{3.30}$$

Therefore, the inductance and capacitance for the impedance network can be calculated according to these parameters including the desired voltage ripple and current ripple, as well as shoot-through time, shoot-through duty ratio, dc supply voltage, and output current.

3.3 Control Methods for Z-Source Inverters and Simulation Results

Since the ZSI has a special shoot-through state, the control methods for ZSIs are different from any other method for conventional inverters. In order to control ZSIs, there are three commonly used methods based on the various PWM techniques:

- Simple boost control [32]

- Maximum boost control [42]

- Maximum constant boost control [43]

> **Simple Boost Control**

In the simple boost control, there are two additional reference waves, which are two straight lines. The upper line has a reference value which equals the amplitude of

the sinusoidal wave as shown in Figure 3.12. Similarly, the lower line has a value which

equals the negative amplitude of the sinusoidal wave as shown in Figure 3.12. Once the

value of the carrier wave (triangular wave) becomes either larger than the upper line or

smaller than the lower line, the shoot-through operation will be implemented. However,

between the two straight lines, the operation follows the conventional PWM technique

as shown in Figure 3.12.
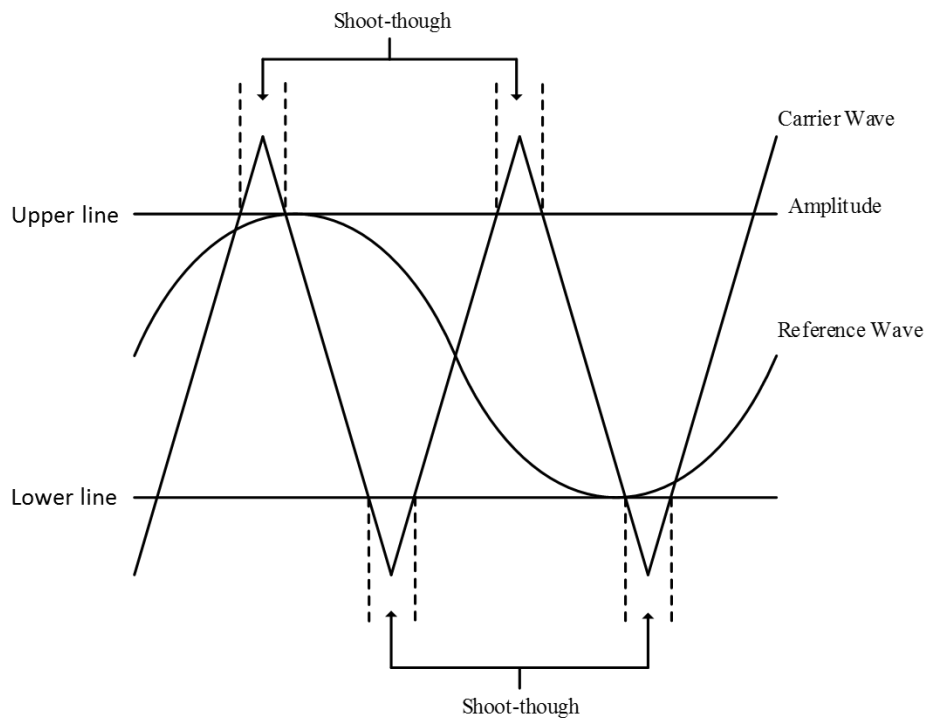
Figure 3.12: Simple boost control waveforms.

The modulation index, M, in the PWM technique is defined as follows:

$$M = \frac{Amplitude\ of\ the\ reference\ wave}{Amplitude\ of\ the\ carrier\ wave}$$

From Figure 3.12, it is obviously that the longer the shoot-thought time, the lower the

modulation index. Therefore, in the simple boost control, the relationship between the

modulation index, M, and the shoot-through duty ratio, T_S/T, can be written as follows:

$$M + \frac{T_s}{T} = 1 \tag{3.31}$$

From (3.19) and (3.21), one can obtain the following:

$$G = MB = M\frac{1}{1-2\dfrac{T_s}{T}}$$

(3.32)

By substituting (3.31) into (3.32), the voltage gain, G, can be written as a function of modulation index, M, as follows:

$$G = \frac{M}{2M-1}$$

(3.33)

where, $0.5 < M \leq 1$. From (3.32) and (3.33), the boost factor, B, can be obtained as follows:

$$B = \frac{G}{M} = \frac{1}{2M-1} = 2G-1$$

(3.34)

> **Maximum Boost Control**

The principle for the maximum boost control can best be explained through the schematic of Figure 3.13. Once the value of the carrier wave (triangle wave) becomes larger than the maximum value of all the three reference waves (sinusoidal waves) at that time, the shoot-through operation is implemented. Similarly, when the value of the carrier wave becomes smaller than the minimum value of all the three reference waves at that time, the shoot-through operation is implemented.

Assuming that the frequency of the carrier wave is much higher than the frequency of the reference wave, the shoot-through duty ratio in the interval ($\pi/6 < \theta < \pi/2$) can be expressed as follows [42]:

$$\frac{T_s(\theta)}{T} = \frac{2 - \left(M \cdot \sin\theta - M \cdot \sin(\theta - \frac{2\pi}{3}) \right)}{2}$$

(3.35)
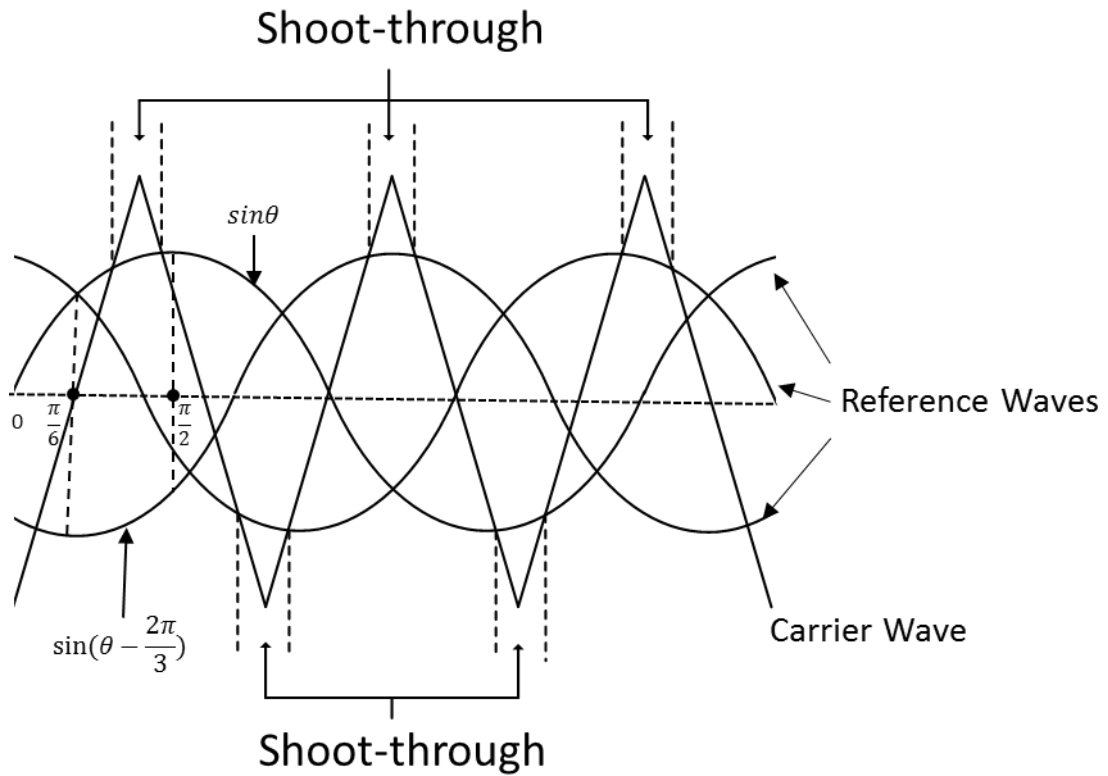
Figure 3.13: Maximum boost control waveforms.

The average duty ratio of the shoot-through, $\langle T_s \rangle / T$, can be calculated by integrating (3.35) which yields the following [42]:

$$\frac{\langle T_s \rangle}{T} = \int_{\pi/6}^{\pi/2} \frac{2 - (M \cdot \sin \theta - M \cdot \sin(\theta - 2\pi/3))}{2} d\theta = \frac{2\pi - 3\sqrt{3}M}{2\pi} \tag{3.36}$$

From (3.36), the boost factor, B, can be obtained as follows:

$$B = \frac{1}{1 - 2\frac{\overline{T_s}}{T}} = \frac{\pi}{3\sqrt{3}M - \pi} \tag{3.37}$$

where, $\sqrt{3}\pi/9 < M \leq 1$. From (3.32), the voltage gain, G, can be expressed by the following:

$$G = MB = \frac{\pi M}{3\sqrt{3}M - \pi} \tag{3.38}$$

➢ **Maximum Constant Boost Control**

In order to reduce the volume and cost of the Z-source network in the ZSI, one needs to eliminate the low-frequency current ripple by using a constant shoot-through duty ratio [43]. Because the boost factor is determined by the shoot-through duty cycle, as expressed in (3.19), the shoot-through duty cycle must be kept the same from switching cycle to switching cycle in order to maintain a constant boost. The principle for the maximum boost control is to get the maximum boost factor, B, while keeping it constant at all times. As shown in Figure 3.14, the upper envelope curve, V_p, and lower envelope curve, V_n, are periodical and have a frequency which is three times the output frequency. Once the value of the carrier wave becomes either larger than the upper envelope, V_p, or smaller than the lower envelope, V_n, the shoot-through operation is implemented. For other conditions, the control follows the conventional PWM technique.
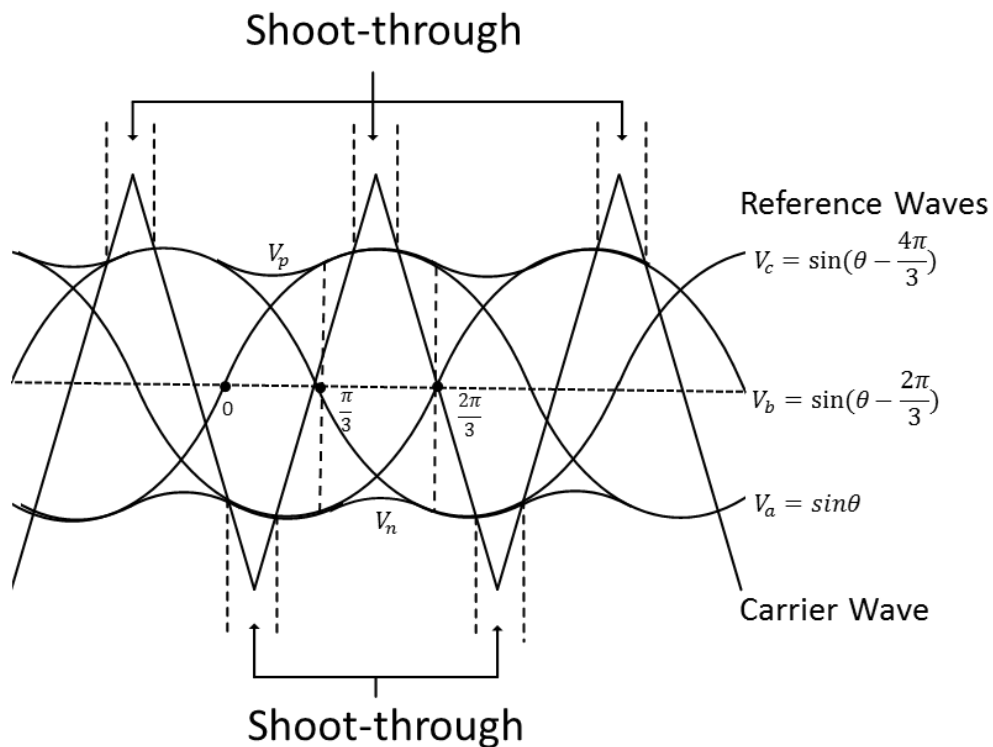
Figure 3.14: Maximum constant boost control waveforms.

For the period $0 \leq \theta \leq \pi/3$ in Figure 3.14, the upper envelope and the lower envelope can be expressed as follows [43]:

$$V_{p1} = M \sin(\theta - \frac{2\pi}{3}) + \sqrt{3}M \tag{3.39}$$

$$V_{n1} = M \sin(\theta - \frac{2\pi}{3}) \tag{3.40}$$

For the period $\pi/3 \leq \theta \leq 2\pi/3$ in Figure 3.14, the upper envelope and the lower envelope can be expressed as follows [43]:

$$V_{p2} = M \sin(\theta) \tag{3.41}$$

$$V_{n1} = M \sin(\theta) - \sqrt{3}M \tag{3.42}$$

Of course, the distance between the upper envelope and the lower envelope is always a constant value, which is $\sqrt{3}M$. Since the distance between the two envelopes determines the shoot-through operation, the shoot-through duty ratio is constant as well, which can be presented as follows [43]:

$$\frac{T_s}{T} = \frac{2 - \sqrt{3}M}{2} \tag{3.43}$$

By substituting (3.43) into (3.19), the boost factor, B, can be obtained as follows:

$$B = \frac{1}{1 - 2\frac{T_s}{T}} = \frac{1}{\sqrt{3}M - 1} \tag{3.44}$$

where, $\sqrt{3}/3 < M \leq 1$. From (3.44), the voltage gain, G, can be expressed as follows:

$$G = MB = \frac{M}{\sqrt{3}M - 1} \tag{3.45}$$

For a specific ZSI, the difference between the three control methods stems from the different voltage stress value on the switching devices and the different voltage gains with the same modulation index. Figure 3.15 shows the maximum obtainable

voltage gain, G, versus the modulation index, M. It is obvious that the maximum boost control has the highest voltage gain and the simple boost control has the lowest voltage gain for the same modulation index.
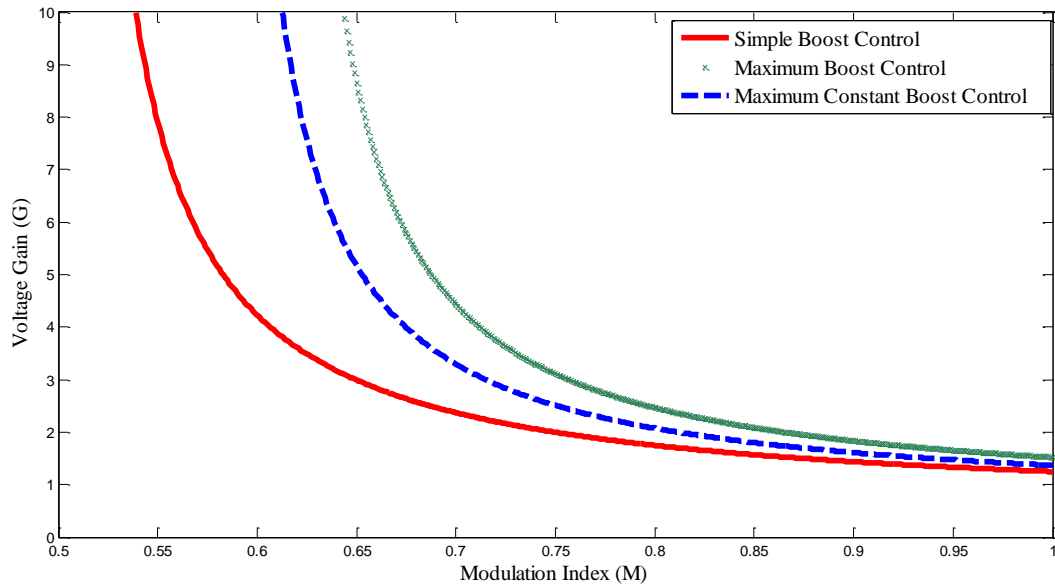
Figure 3.15: Voltage gain versus modulation index.

The voltage stress on the inverter bridge/phase-legs of a ZSI can be expressed as the following:

$$V_{stress} = BV_{dc} \tag{3.46}$$

For the three methods with the same output voltage value, the voltage stress characteristic value on the inverter bridge are different as shown in Figure 3.16. Obviously, the simple boost control has the highest voltage stress on the inverter bridge. While, the maximum boost control has the lowest voltage stress. The maximum constant boost control has slightly higher voltage stress than the maximum boost control.
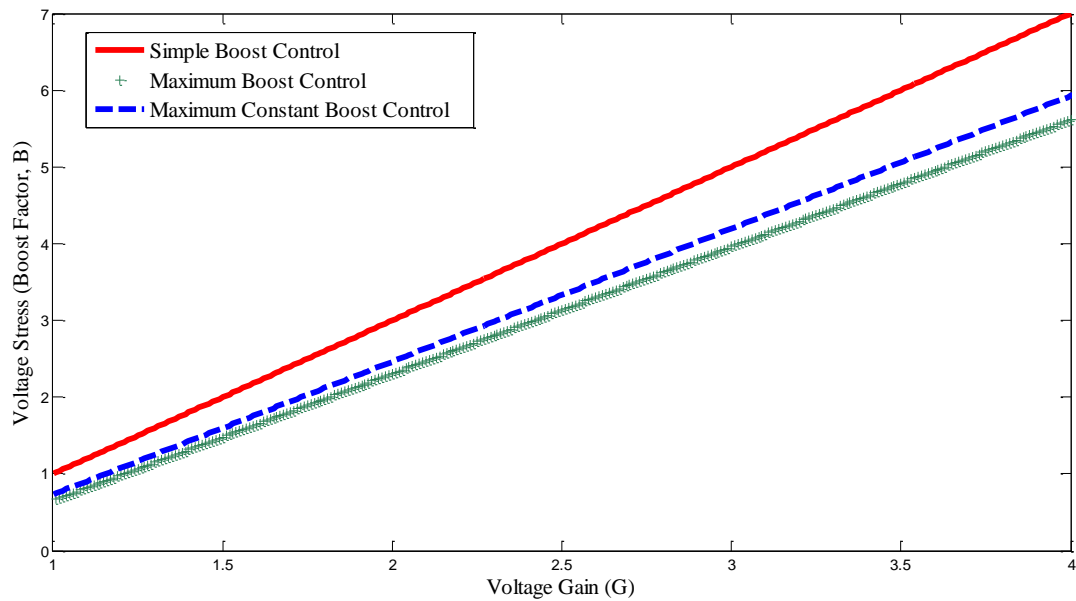
Figure 3.16: Voltage stress on the inverter bridge versus voltage gain.

In order to observe and analyze the output voltages and currents of ZSIs, a ZSI model energizing a three-phase balanced resistive and inductive load was simulated in ANSYS Simplorer as shown in Figure 3.17. The simulation parameters are as follows: the Z-impedance network: $L_1 = L_2 = 500\mu H$, and $C_1 = C_2 = 3000\mu F$; the dc bus voltage: 310 V; the R-L load: $R = 1\Omega$ and $L = 3$mH. The carrier/switching frequency was set to 5 kHz, while the power frequency was set to 60 Hz.
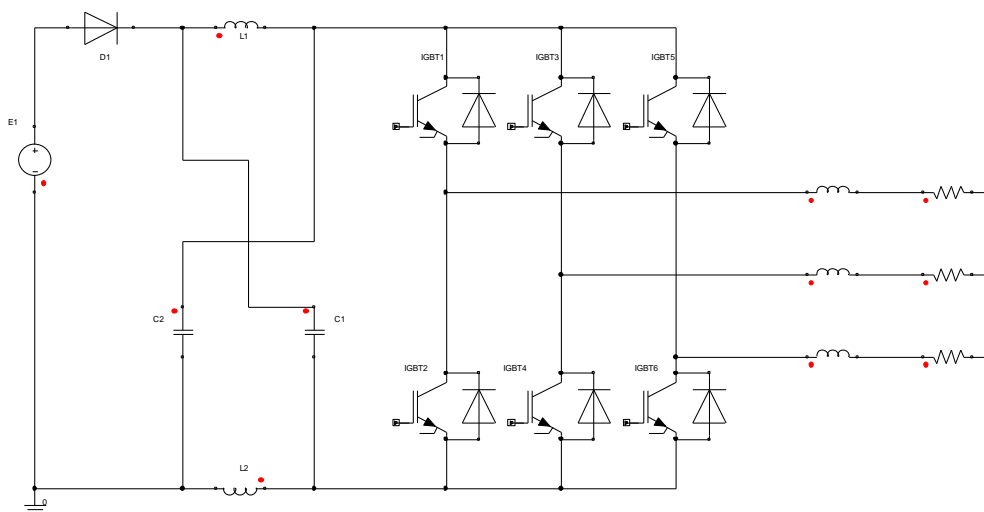
Figure 3.17: ZSI with three-phase balanced RL load.

For the simple boost control, Figure 3.18 shows (a) the line-to-line voltage, (b) the phase voltage, and (c) the phase current, with a modulation index, M=0.8, respectively. It is obvious that the peak value of the line-to-line voltage which is about 570 V is higher than the dc bus voltage which is 310 V.
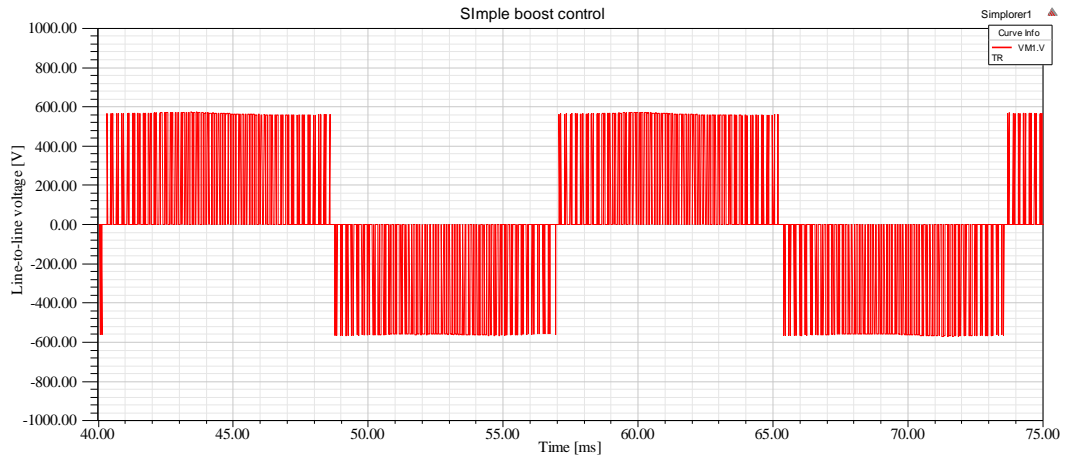
(a) Line-to-line voltage with M=0.8
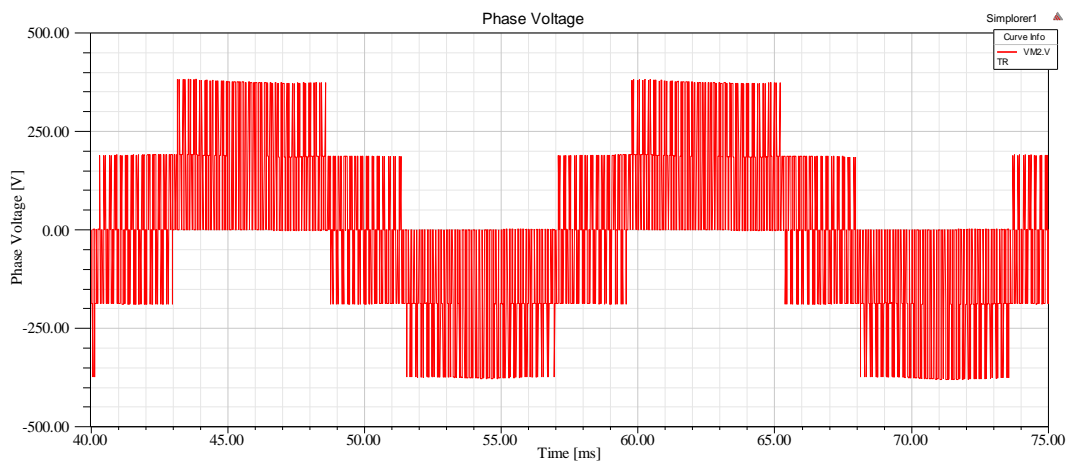
(b) Phase voltage with M=0.8
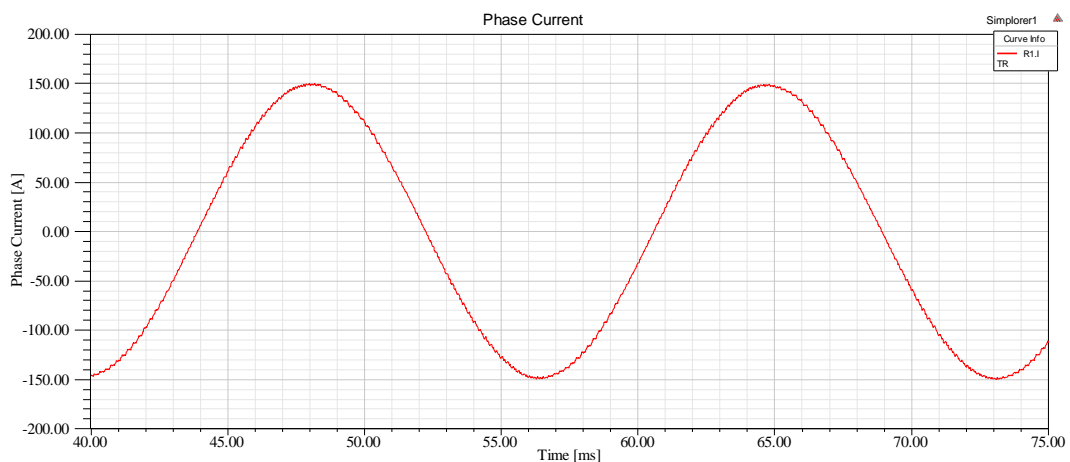
(c) Phase current with M=0.8

Figure 3.18: Output waveforms of the ZSI with the simple boost control.

For different modulation indices, the lower the modulation index the higher the boost factor and the higher the voltage gain. Figure 3.19 shows the line-to-line voltage of the simple boost control with different modulation indices of 0.9, 0.8, and 0.7, respectively.
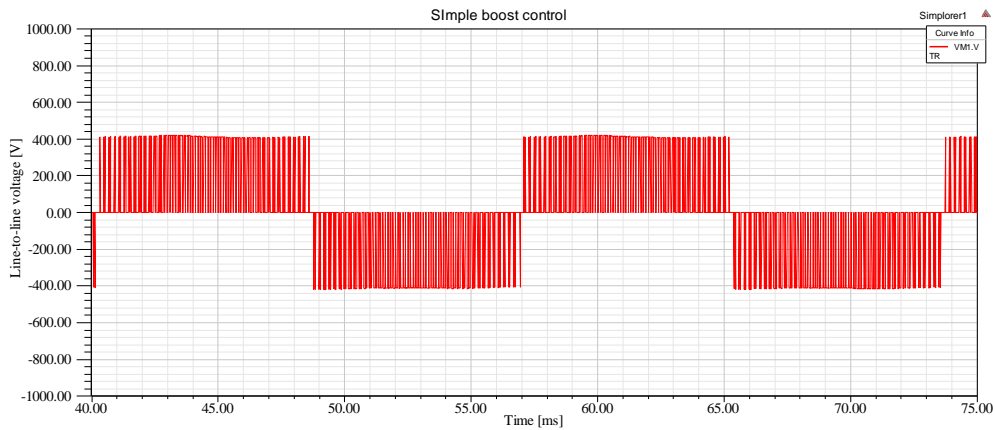
(a) Line-to-line voltage with M=0.9
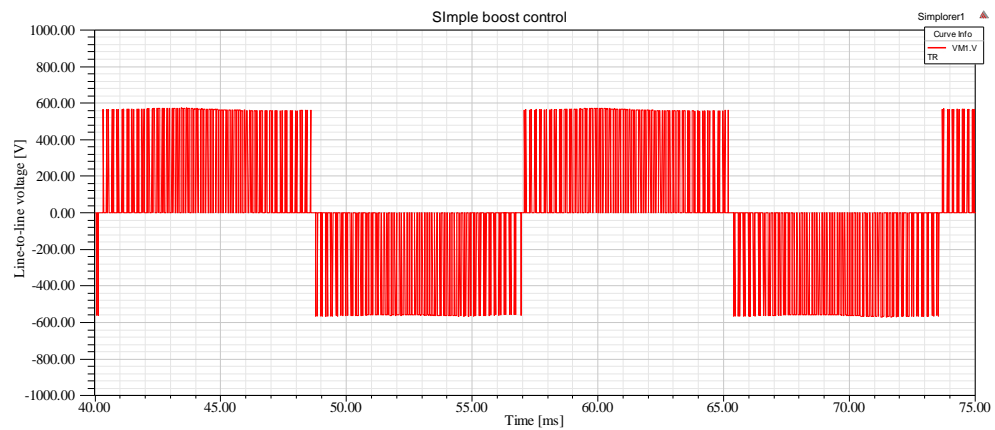
(b) Line-to-line voltage with M=0.8
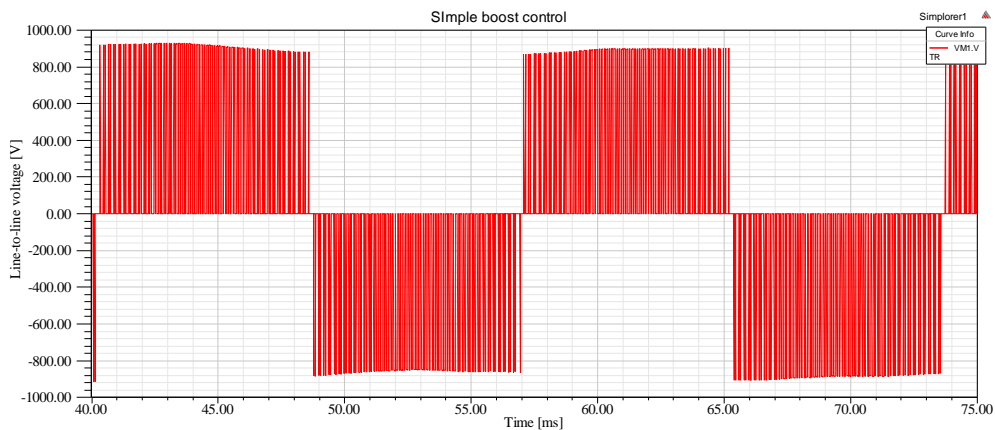
(c) Line-to-line voltage with M=0.7

Figure 3.19: Line-to-line voltages of the simple boost control with different modulation indices.

For different control methods, Figure 3.20 shows the output line-to-line voltages with the same modulation index of 0.8, for (a) simple boost control, (b) maximum boost control, and (c) maximum constant boost control, respectively. It is obvious that the maximum boost control has the highest peak value of line-to-line voltage which is about 996 V and the simple boost control has the lowest peak value of line-to-line voltage which is about 570 V. This is in comparison to a dc bus voltage of 310 V.
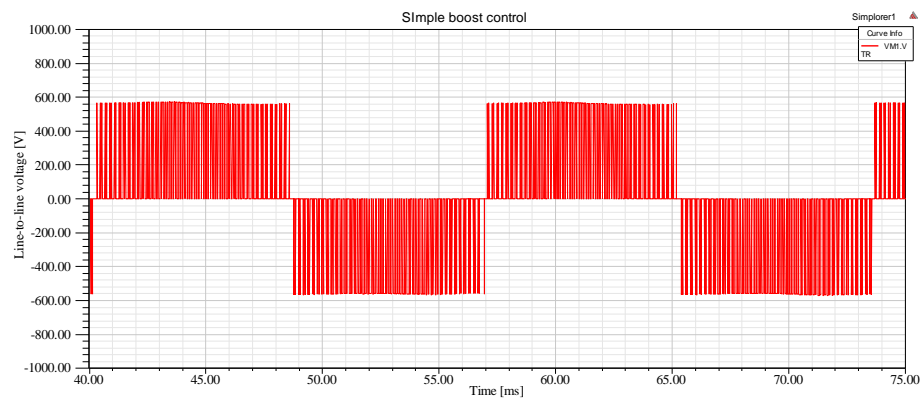
(a) Simple boost control with M=0.8
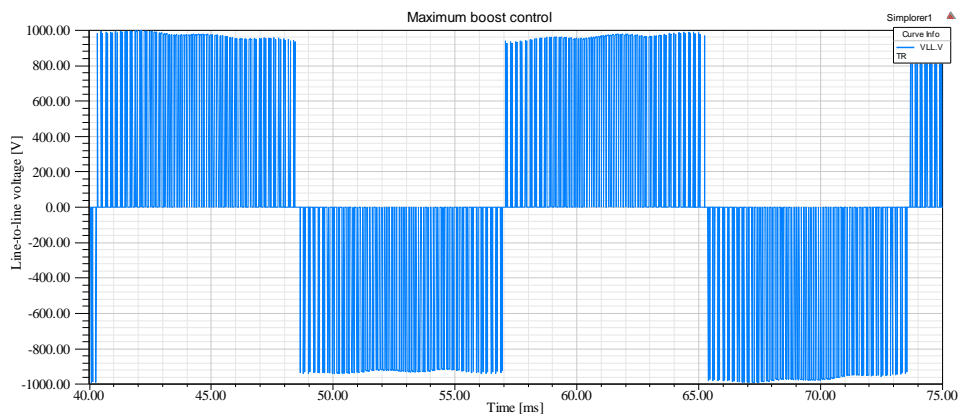
(b) Maximum boost control with M=0.8
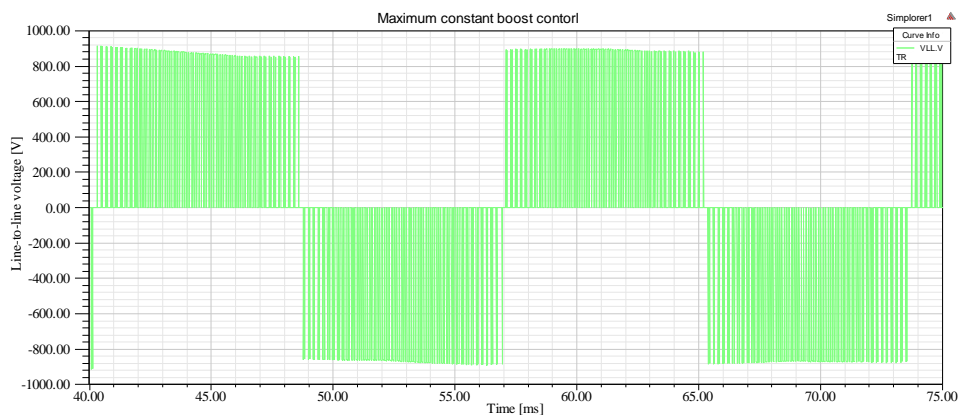
(c) Maximum constant boost control with M=0.8

Figure 3.20: Line-to-line voltages of different control methods.

Chapter 4

Flux-Weakening Control of IPMSMs Driven by Z-source Inverters

In order to drive a motor at desired torque and/or speed, a suitable control loop has to be developed and imbedded into a digital controller or microprocessor, which is the core of a motor-drive. This chapter presents a new flux-weakening (FW) algorithm by employing the voltage boost capability of Z-source inverters. Meanwhile, a new control scheme is designed for IPMSMs driven by Z-source inverters with MTPA control at low speeds and FW control at high speeds. Simulation results are given at the end of this chapter to verify the presented control algorithm and control scheme.

4.1 Introduction

Interior permanent magnet synchronous motors (IPMSM) have gained an increasing popularity in recent years for a wide variety of industrial drive applications including hybrid and electric vehicles. In order to obtain high performance of IPMSMs, various control strategies and algorithms for such IPMSMs have been developed over the past 30 years. A widely used control strategy for IPMSMs is implementing the MTPA control during constant torque (low speeds) region and the FW control during constant power region (high speeds) [22-24, 28] as depicted schematically in Figure 4.1.

The most widely used the FW control method for IPMSMs is the voltage and current limited maximum torque control. With a conventional motor-drive, the FW operation of IPMSMs is still limited by the voltage constraint from the drive side. Moreover, as presented earlier in (2.77), the maximum motor speed is directly impacted by the maximum voltage of the drive. Therefore, with a ZSI which has an adequate voltage boost capability, the speed range of IPMs can be further extended.
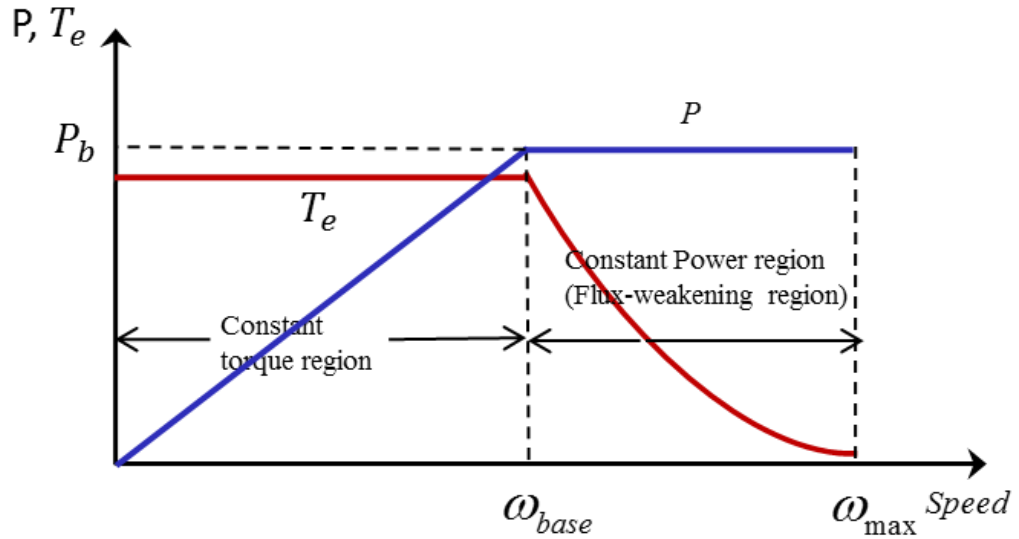
Figure 4.1: Typical characteristic curves of torque/power vs. speed of IPMSMs.

In this chapter, a new approach utilizing ZSIs for the FW control is presented. Due to the voltage boost capability of ZSIs, a new FW control algorithm is developed for such ZSI-based drives. For a full speed range operation, the control strategy developed in this thesis implements the MTPA control at the low speed region up to the base speed, and this strategy changes to boosted-voltage FW control when the speed becomes higher than the base speed. Subsequent to the development of this control strategy, a corresponding control scheme was also developed for simulations of its performance throughout the full speed range of operation. In the end, to verify the new FW control method, a motor-drive system based on a ZSI was developed and simulated with this control strategy throughout full speed range.

4.2 Boosted-Voltage Constant-Power Flux-Weakening Control Algorithm

In practical applications, the FW operation can be achieved through various approaches. In [12], a d-axis current component was used as a feedback to control a FW regulator. One popular FW control approach using a speed feedback to generate a demagnetizing current was presented in [24, 48]. Another popular approach employs

an inverter voltage as a feedback for the FW control [22, 23, and 67]. In all the published FW approaches, the speed range of an IPM motor is limited by the maximum inverter voltage. The reason for this limitation stems from the fact that maximum speeds of IPM motors are proportional to maximum inverter output voltages, as formulated earlier in (2.77), which is repeated here for convenience as follows:

$$\omega_{\max} = \frac{V_{\max} / L_d}{(\lambda_{pm} / L_d - \hat{I}_{\max})} \tag{4.1}$$

where, $\hat{V}_{max}$ is the amplitude of the maximum inverter voltage and $\hat{I}_{max}$ is the amplitude of the maximum inverter current. No matter how the demagnetizing current is generated, the employed control algorithm has to follow the voltage and current limitation which was also introduced earlier in Chapter 2 as the voltage and current limited maximum torque (VCLMT) control.

With the help of ZSIs, motor-drives can provide boosted voltages which are controlled by special methods. From (4.1), it is obvious that the speed range can be further extended with such a boosted inverter output voltage. Since the output voltages of ZSIs can be boosted and are controllable, the voltage limitation is eliminated. However, the current limitation has to be followed due to a motor's thermal dissipation and cooling method. In order to follow typical characteristics of IPMSMs as shown in Figure 4.1, the output power of such motors is desired to remain constant during the FW operation region. Therefore, considering all the new conditions, a boosted-voltage constant-power FW control algorithm was developed, which will be referred to here in this thesis for simplicity as the boosted-voltage FW (BVFW) control approach. The details of this new FW control algorithm are given next.

The output power equation of such motors can be written as follows:

$$P = T_e \omega_m \tag{4.2}$$

where, T_e is the developed torque, and ω_m is the motor's mechanical speed. At speeds greater than or equal to the base speed, ω_{base}, the output power remains constant at the motor's rated output power, P_b. Meanwhile, at speeds lower than the base speed the torque remains constant at maximum torque per ampere, while the output power is defined by (4.2). Here, the developed torque, T_e, can be expressed as in (2.29), and is repeated for convenience as follows:

$$T_e = \frac{3}{2}\frac{p}{2}\left(\lambda_{pm}i_q + (L_d - L_q)i_d i_q\right) \tag{4.3}$$

where, $\hat{\lambda}_{pm}$ is the amplitude of the flux linkage due to the flux associated with permanent magnets, L_d is the d-axis inductance, and L_q is the q-axis inductance. From (2.27), mechanical speeds of motors, ω_m, can be expressed in terms of the electrical angular frequency, ω_e, as follows:

$$\omega_m = \omega_e / \frac{p}{2} \tag{4.4}$$

where, p is the number of poles. By substituting (4.3) and (4.4) into (4.2), one can obtain the following:

$$P_b = \frac{3}{2}\left(\lambda_{pm}i_q + (L_d - L_q)i_d i_q\right)\omega_e \tag{4.5}$$

By enforcing the current limit, $\hat{I}_{max}$, one can express the q-axis component of the current, i_q, as follows:

$$i_q = \sqrt{\hat{I}_{max}^2 - i_d^2} \tag{4.6}$$

where, $\hat{I}_{max}$ represents the amplitude of the maximum phase current which is the current limitation for a given motor. Then, by substituting (4.6) into (4.5), one can obtain the following:

$$P_b = \frac{3}{2}\left[\lambda_{pm}\sqrt{\hat{I}_{max}^2 - i_d^2} + \left(L_d - L_q\right)i_d\sqrt{\hat{I}_{max}^2 - i_d^2}\right]\omega_e \tag{4.7}$$

Notice that the rated output power, P_b, is a motor parameter so as the maximum current, $\hat{I}_{max}$. Assuming that all the motor parameters are known in (4.7), only the d-axis current component becomes the dependent variable function of speed. Therefore, the d-axis current component can be obtained from the solution of a quartic equation in i_d, which is further simplified from (4.7) as follows:

$$ai_d^4 + bi_d^3 + ci_d^2 + di_d + e = 0 \tag{4.8}$$

where,

$$a = \left(L_d - L_q\right)^2 \qquad\qquad b = 2\lambda_{pm}\left(L_d - L_q\right)$$

$$c = \lambda_{pm}^2 - \left(L_d - L_q\right)^2 \hat{I}_{max}^2 \qquad d = -2\lambda_{pm}\left(L_d - L_q\right)^2 \hat{I}_{max}^2$$

$$e = 4P_b^2 / 9\omega_e^2 - \lambda_{pm}^2 \hat{I}_{max}^2$$

From the quartic equation (4.8), four roots, i_{d1}, i_{d2}, i_{d3}, and i_{d4}, can be obtained according to the general root formulas, x_1, x_2, x_3, and x_4, for quartic equations in Appendix I, respectively. In order to verify the validity of each root, the four general root formulas in Appendix I had been simulated and calculated many times according to different IPM motors. It was found out that only the second general root, x_2, which yields the d-axis current component, i_{d2}, is the desired solution. Because only the second root, x_2, is a negative real value. Once the quartic equation (4.8) is solved, the d-axis current component, i_d, can be obtained. Then the q-axis current component, i_q, can be obtained by substituting such i_d into (4.6). Meanwhile, the peak value of phase voltages can be obtained through (2.49) which is repeated here for convenience as follows:

$$\hat{V}_s = \sqrt{(\omega_e L_q i_q)^2 + \left(\omega_e(L_d i_d + \lambda_{pm})\right)^2} \tag{4.9}$$

For ZSIs, the peak value of phase voltages, which was presented in (3.21), is

also repeated here for convenience as follows:

$$\hat{v}_a = M \cdot B \cdot \frac{V_{dc}}{2} = G \cdot \frac{V_{dc}}{2} \tag{4.10}$$

From (4.9) and (4.10), the required voltage gain, G, can be obtained by the following:

$$G = 2\frac{\hat{v}_a}{V_{dc}} = 2\frac{V_s}{V_{dc}} = \frac{2}{V_{dc}}\sqrt{(\omega_e L_q i_q)^2 + \left(\omega_e (L_d i_d + \lambda_{pm})\right)^2} \tag{4.11}$$

Then, the modulation index and shoot-through duty ratio are determined by the chosen control method for ZSIs.

In order to verify the validity of this BVFW method, simulation results of this algorithm are presented in this section as well. The control algorithm used during the low speed region is the MTPA control, and after the base speed, the FW control algorithms are implemented. The machine parameters used are listed in Table 4.1. Figure 4.2 depicts the output power of this motor over the entire operating speed range. The comparison between the introduced VCLMT control in Chapter 2 and the new BVFW control is also depicted in Figure 4.2. In the low speed region, the output power is proportional to the motor speed due to the MTPA control. On the other hand, it is obvious that the VCLMT control cannot sustain a constant output power as the BVFW control takes place during the FW region. Therefore, one of the advantages of this BVFW control is the constant output power during the FW operation.

$\hat{\lambda}_{pm}$	0.148 wb
L_d	0.0054 H
L_d	0.0105 H
Resistance per phase	0.45 ohm
Rated Current	10 A
Amplitude of maximum phase current, $\hat{I}_{max}$	$10\sqrt{2}$ A
Rated Line-to-Line Voltage	240 V
DC bus voltage	400 V
Amplitude of maximum phase voltage, $\hat{V}_{max}$	200 V
Rated Speed	3450 r/min
Rated Torque	7.25 N·m
Rated Power	3.5 hp (2610 watts)
Number of poles	6

Table 4.1: IPM motor parameters for simulation.
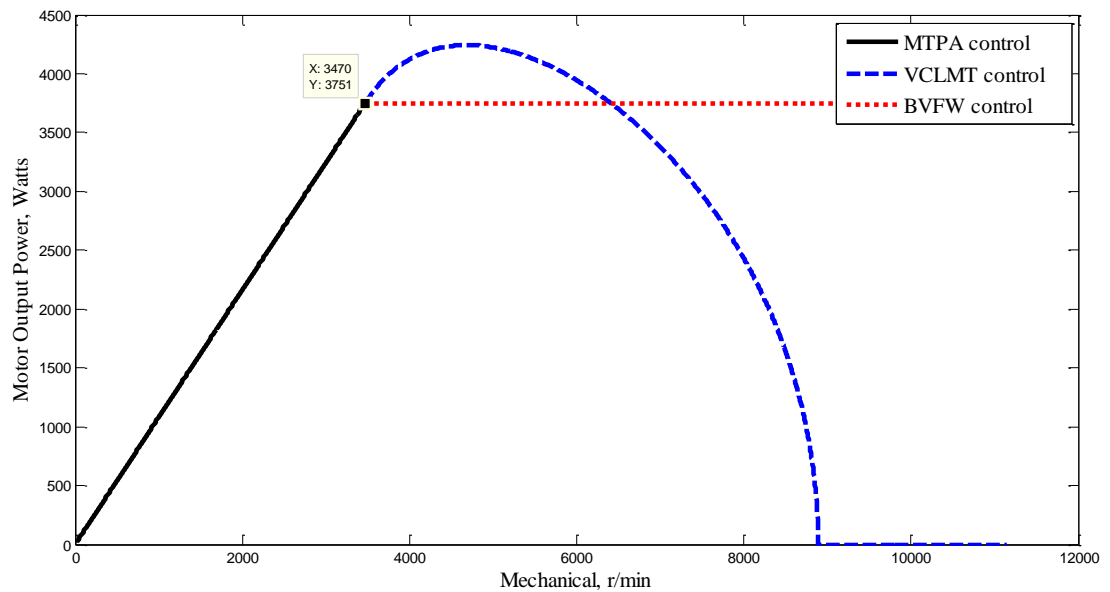
Figure 4.2: Comparison of output power between VCLMT control and BVFW control.

Other simulation result as shown in Figure 4.3 presents the comparison between the developed torque for under the VCLMT control and the BVFW control, respectively.

In the low speed region, the torque remained at a constant value until the base speed. Such base speed can be obtained from (2.51) which is repeated here for convenience as follows:

$$\omega_{base} = \frac{V_{max}}{\sqrt{(L_d \cdot i_{dm} + \lambda_{pm})^2 + (L_q \cdot i_{qm})^2}} \tag{4.12}$$

In the FW region, the developed torque keeps decreasing as shown in Figure 4.3. From this simulation result, one merit of the BVFW control is that this method can provide high output torque in the high speed region without increasing motor's current rating, which also indicates that this algorithm can control an IPM motor for operating at a higher speed range than the VCLMT control.
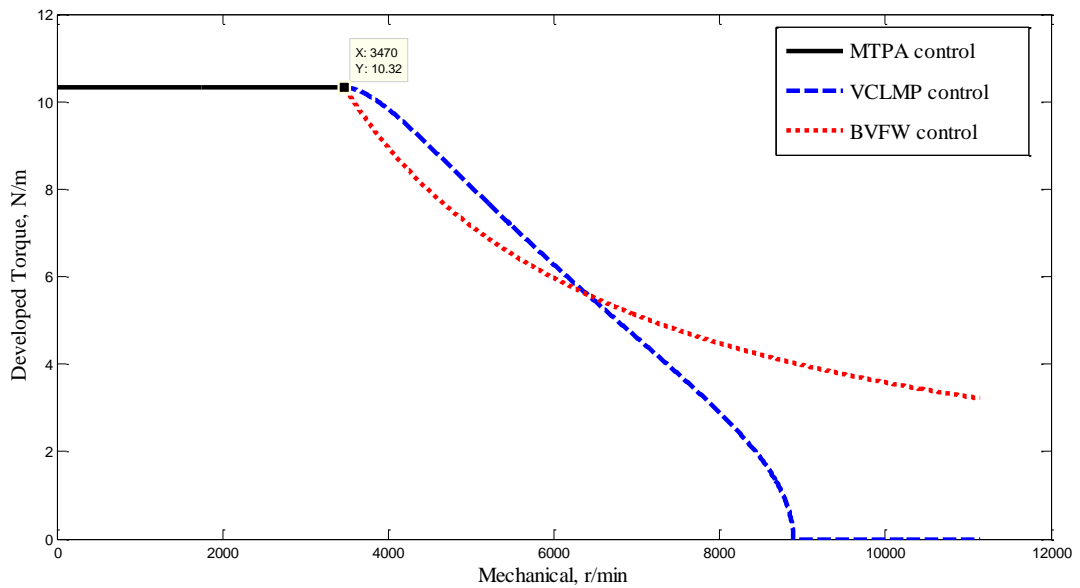
Figure 4.3: Comparison of developed torque between the VCLMT control and the BVFW control.

To verify the validity of the BVFW method, the d- and q-axis current trajectories versus speed are presented in Figure 4.4. During the constant torque region, the MTPA control is implemented, which yields constant d- and q-axis current components. Meanwhile, after the BVFW control is implemented, the d-axis current

component keeps increasing in the negative direction and the q-axis current keeps decreasing in the positive direction.
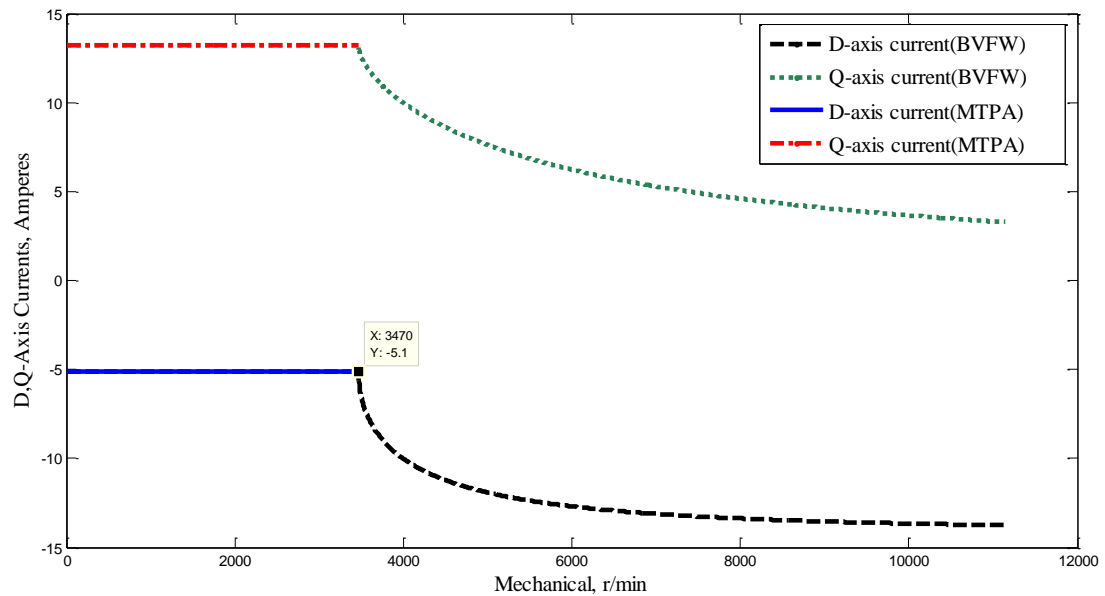
Figure 4.4: D, q-axis current components versus speed of the BVFW control.

The most significant feature of this BVFW control is the boosted voltage as shown in Figure 4.5. With the MTPA control during the low speed region, both the d- and q-axis voltage components are proportional to motor speed. While, with the BVFW control at high speeds, a slight drop can be observed in the phase voltages and q-axis voltage component at the beginning of the FW operation. Then, the phase voltage and q-axis voltage component keep increasing as the speed is increased. While, the amplitude of the d-axis voltage component does not increase with the motor speed during the whole FW region.
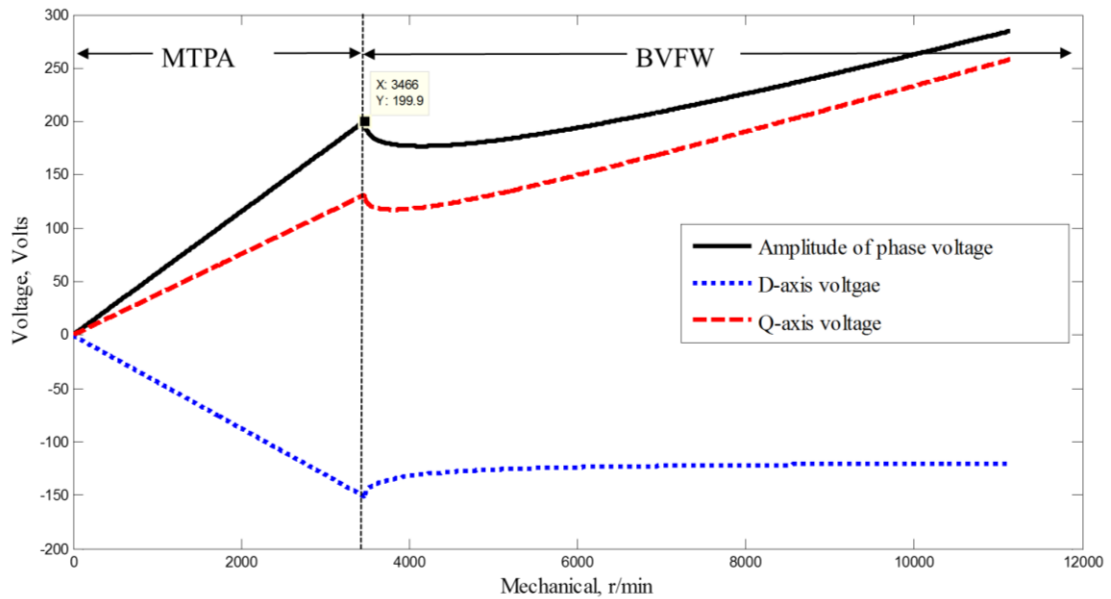
Figure 4.5: D, q-axis voltage components versus speed of the BVFW control.

4.3 Control Scheme Design for IPMSMs Driven by Z-source Inverters

In order to control the speed of an IPM motor, a logical control scheme has to be developed to control the motor-drive for such motors. For a full speed range of operation, the desired control scheme should be able to fully utilize the controlled motor on both low speed region and high speed region of the operating range . Therefore, a widely used control strategy for this control scheme utilizes implementing the MTPA control in the constant torque region, and the FW control in the constant power region as shown in Figure 4.1.

There are many control schemes published in the literatures that combines the MTPA control and the FW control [22-24]. Figure 4.6 shows the specially designed control scheme for IPMSMs driven by ZSIs, which is based on speed control schemes presented in [22-24]. The proposed control scheme in FIGURE 4.6 consists of three major controllers, namely, the speed regulator in Part A, the current regulator in Part B, and the BVFW regulator in Part C.
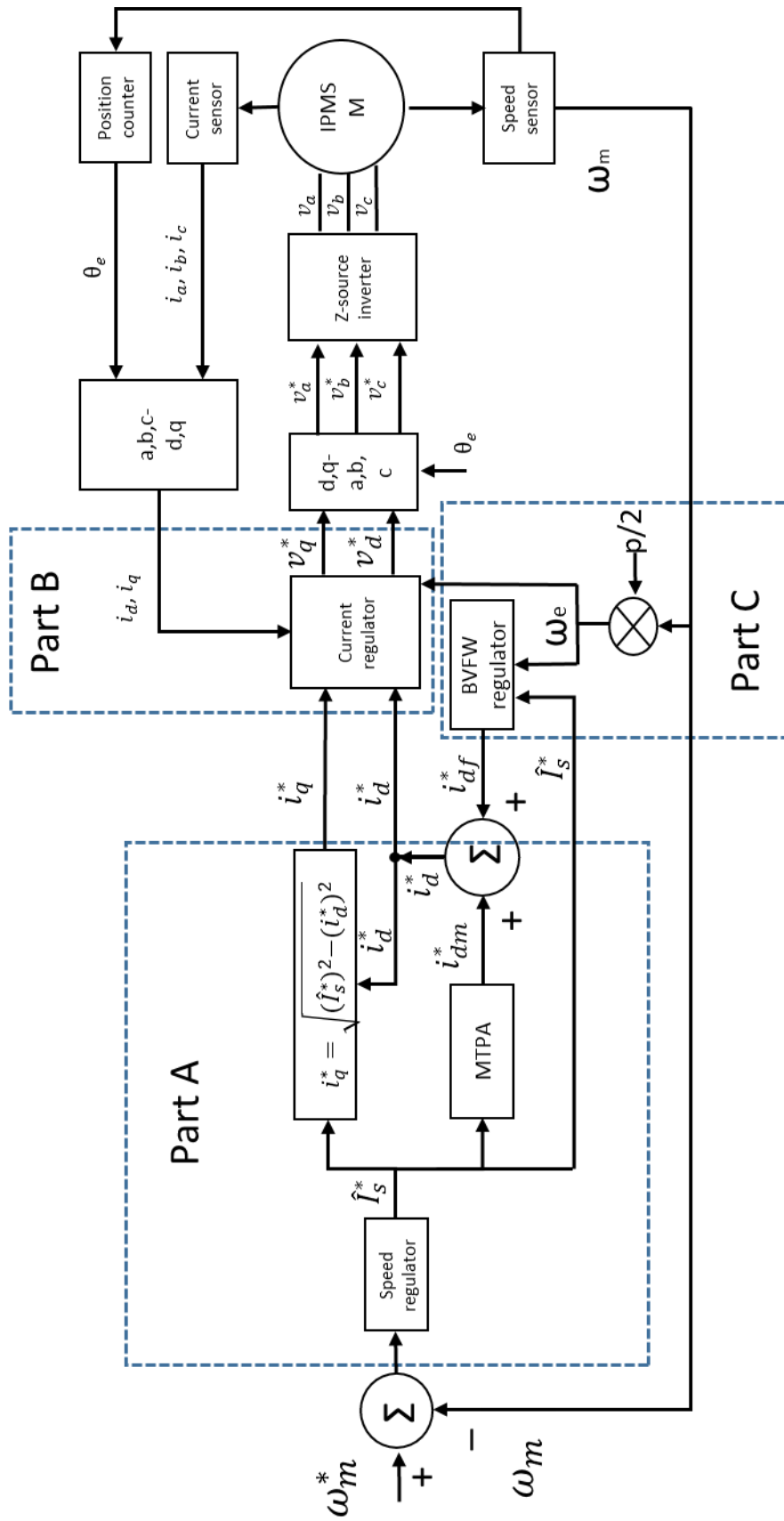
Figure 4.6: Control scheme of the MTPA control and the BVFW control.

Assuming the controlled motor is in the stop or standby state, a commanded speed /reference speed, ω_m^*, is first sent into the control loop and compared to the feedback speed, ω_m, which is the motor's real speed obtained from an encoder. Then the error difference between the reference speed and the real speed is sent into the speed controller in Part A. According to this speed error, a reference value of the amplitude of the phase currents, $\hat{I}_s^*$, is generated by the speed regulator. Notice that in this speed control scheme, there is no reference torque. In order to obtain the maximum torque during the full speed range, the reference phase current during the MTPA control and the BVFW control is set to its maximum value, which means $\hat{I}_s^* = \hat{I}_{max}^*$. Such $\hat{I}_s^*$ will be send into the MTPA block which yields the reference d-axis current component, i_{dm}^*, for the MTPA control according to (2.46). It has to be emphasized that the BVFW regulator has zero output before the speed reaches the base speed, ω_b. Therefore, during the constant torque region, the reference demagnetizing current, i_{df}^*, for the BVFW control is zero. Since the reference d-axis current, $i_d^* = i_{dm}^* + i_{df}^*$, one can state that $i_d^* = i_{dm}^*$ during the constant torque region. Then the reference q-axis current can be obtained from (4.6). In the constant power region, where the speed is above the base value, all the components in Part A are still active. However, the BVFW regulator in Part C starts to yield an extra demagnetizing current, i_{df}^*, which can be written as follows:

$$i_{df}^* = i_{dB} - i_{dm}^* \qquad (4.13)$$

where, i_{dB} is the d-axis current component for BVFW control obtained from (4.8).

With the reference d- and q-axis current components, $i_d^* \; and \; i_q^*$, the two reference voltage components, $v_d^* \; and \; v_q^*$, can be obtained from the current regulator in Part B. Then using an inverse Park's transformation, the reference d- and q-axis

voltage components can be transformed to the three-phase voltages, which are v_a^*, v_b^*, and v_c^* in Figure 4.6. Notice that the three reference voltages, v_a^*, v_b^*, and v_c^*, are instantaneous values. Therefore, they can be written as follow:

$$v_a^* = \hat{v}\sin(\omega t) \quad v_b^* = \hat{v}\sin(\omega t - \frac{2\pi}{3}) \quad v_c^* = \hat{v}\sin(\omega t - \frac{4\pi}{3}) \tag{4.14}$$

where, $\hat{v}$ is the amplitude of the phase voltages. In the low speed constant torque region, the shoot-through duty ratio of the ZSI is zero, which means the ZSI works as a three-phase full-bridge inverter, which is controlled by a sinusoidal PWM method. In the high speed FW region, the shoot-through duty ratio can be obtained according to the motor speed and the ZSI provided boosted voltage. Since the inverter used here is a ZSI, one can obtain the following from (4.10):

$$M = 2\hat{v} / (BV_{dc}) \tag{4.15}$$

Then from (4.14) and (4.15), the reference phase-a voltage, v_a, for the sinusoidal PWM can be written as follows:

$$v_a = M\sin(\omega t) = 2\hat{v}\sin(\omega t) / (BV_{dc}) = 2v_a^* / (BV_{dc}) \tag{4.16}$$

For simplicity, the control method used for controlling the ZSI in this scheme is the simple boost control. The voltage gain, G, can be obtained by substituting i_d^*, i_q^*, and the speed feedback, ω_e into (4.11). Then the boost fact, B, can be obtained from (3.34), which is repeated here for convenience as follows:

$$B = 2G - 1 \tag{4.17}$$

By substituting (4.11) and (4.17) into (4.16), the phase-a reference waveform for the sinusoidal PWM technique can be written as follows

$$v_a = 2v_a^* / (BV_{dc}) = \frac{2v_a^*}{4\sqrt{(\omega_e L_q i_q)^2 + \left(\omega_e (L_d i_d + \lambda_{pm})\right)^2} - V_{dc}} \tag{4.18}$$

Similarly, the phase-b and phase-c reference waveforms can be obtained as follows:

$$v_b = 2v_b^* / (BV_{dc}) = \frac{2v_b^*}{4\sqrt{(\omega_e L_q i_q)^2 + \left(\omega_e (L_d i_d + \lambda_{pm})\right)^2} - V_{dc}} \tag{4.19}$$

$$v_c = 2v_c^* / (BV_{dc}) = \frac{2v_c^*}{4\sqrt{(\omega_e L_q i_q)^2 + \left(\omega_e (L_d i_d + \lambda_{pm})\right)^2} - V_{dc}} \tag{4.20}$$

Notice that v_a^*, v_b^*, and v_c^* are sinusoidal time-domain functions.

In general, the speed regulator is a regular PI controller. While, the current regulator usually has to be designed with a feed forward compensation. The reason stems from the fact that the d- and q- axis current components cannot be controlled independently by v_d and v_q because of the cross-coupling effects [24] such as $\omega_e L_d i_d$ and $\omega_e L_q i_q$ in v_d and v_q expressions. The cross-coupling effects in IPM motors are dominant because IPM motors have relatively large inductances. These effects will impact the current response as well as torque response in the high speed FW region. Figure 4.7 shows the decoupled current regulator with feed forward compensation [24] presented here to solve such a problem.
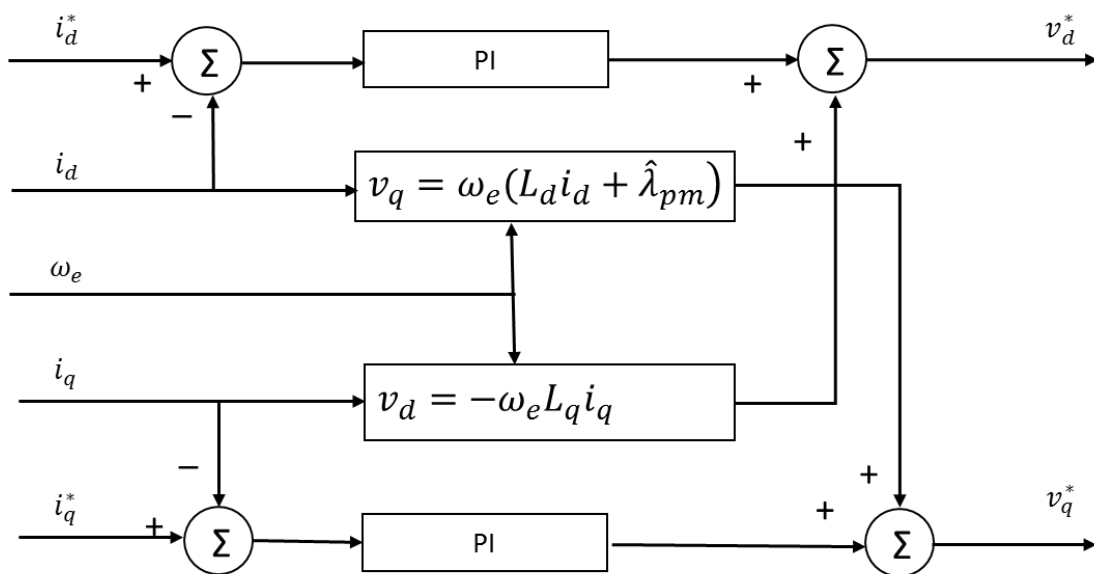
Figure 4.7: Current regulator with decoupled feedforward compensation.

4.4 Simulation Results

In order to verify the presented BVFW control algorithm and corresponding control scheme, a motor-drive system model with mechanical load was developed and simulated in ANSYS Simplorer. The simulated motor was an IPM motor with parameters listed earlier in Table 4.1. The drive side consisted a ZSI and a dc supply as shown in Figure 4.8. Other simulation parameters are as follows: the Z-impedance network consisting of two inductors $L_1 = L_2 = 500\mu H$, and two capacitors $C_1 = C_2 = 3000\mu F$; the dc bus voltage: 400 V; the carrier frequency: 10 kHz; the output LC filter: $L = 5\mu H$, and $C = 50\mu F$; the cable resistance: $R = 0.1\ \Omega$; the mechanical load: inertia $J = 0.02 kgm^2$ and friction torque $T_f = 0.1\ Nm$. Notice that the resistance for each inductor used in the Z-impedance network is $0.001\ \Omega$.

In Figure 4.9, a closed-loop speed control was developed in ANSYS Simplorer. The three major components of Figure 4.9, which are the speed regulator in Part A, current regulator in Part B, and FW regulator in Part C, are controllers designed according to an earlier figure, Figure 4.6.
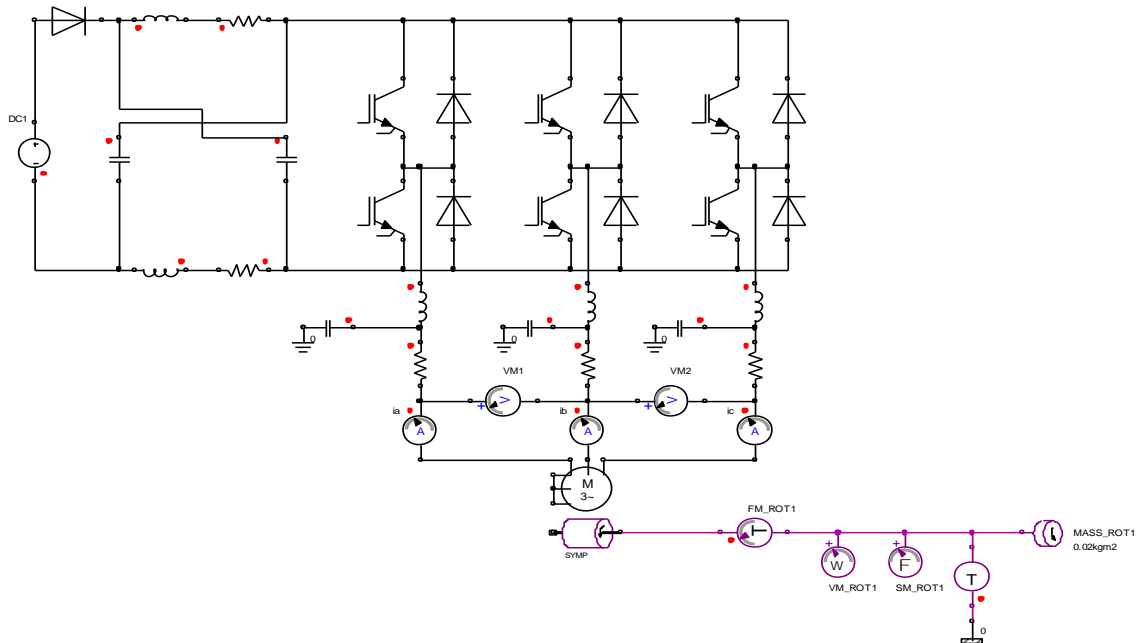
Figure 4.8: Simulation topology of an IPM motor driven by a ZSI.
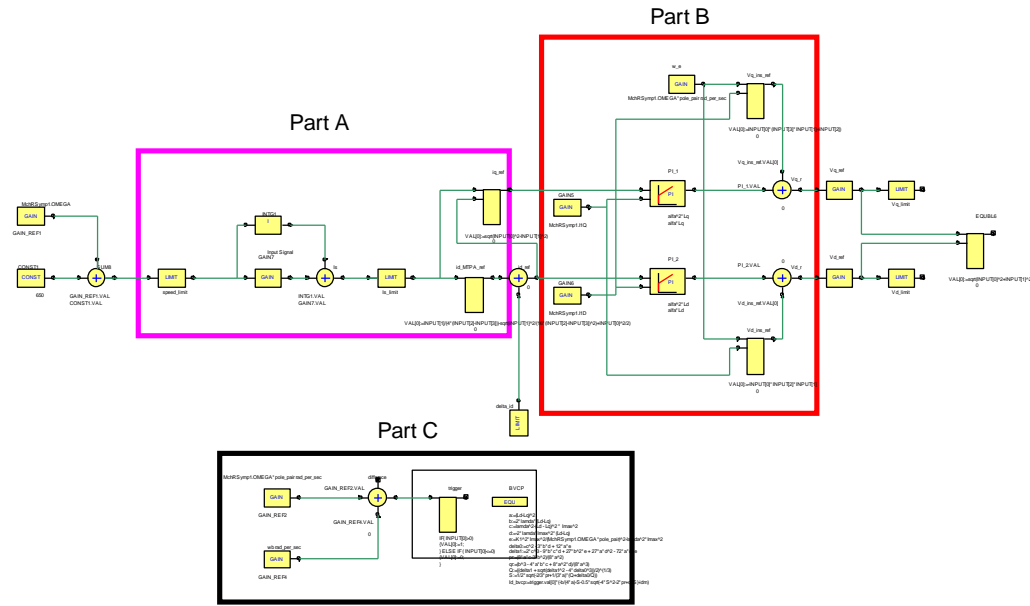
Figure 4.9: Control loops developed in ANSYS Simplorer.

To evaluate the performance of this simulation system in low speeds with the MTPA control, a commanded mechanical speed, which is $\omega_m^* = 300 \; rad/s$, was the assumed input signal to the control loop as show in Figure 4.9. Meanwhile, Figure 4.10 presents the motor's mechanical speed versus time, which shows that the motor's speed keeps increasing from zero until it reaches a steady state where $\omega_m = 289.8 \; rad/s$. The difference between the reference speed and the real speed is only 3.3%, which shows a reliable controller performance at low speeds.
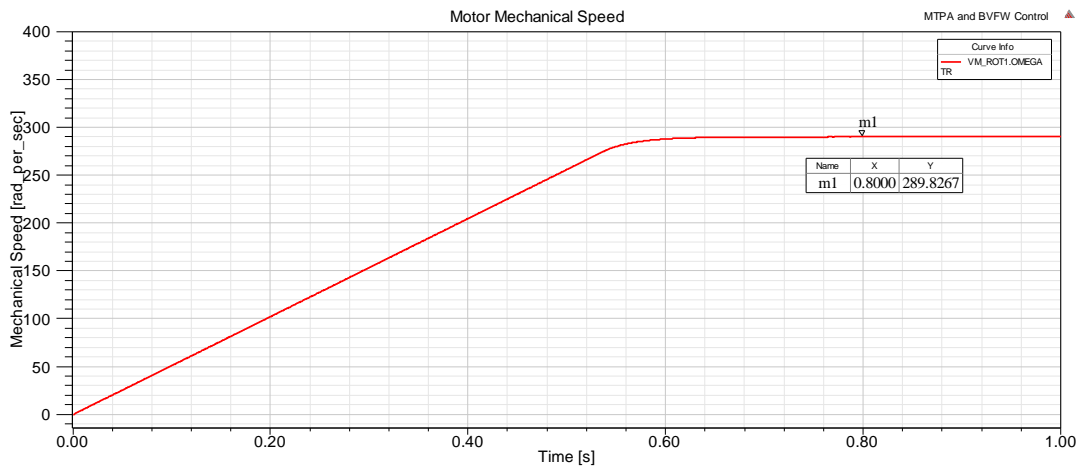
Figure 4.10: Mechanical speed versus time when $\omega_m^* = 300 \; rad/s$.

Figure 4.11 depicts the phase-a current waveform during the entire speed range up to $300\ rad/s$. As the speed increased, the frequency of this current waveform became higher and higher. Meanwhile, Figure 4.12 presents the developed torque, which shows a constant torque operation during this low speed region. Notice that after the speed reaches its reference value, the current and torque start to decrease. Because of the friction torque $T_f = 0.1\ Nm$, both the current and the torque cannot be zero.
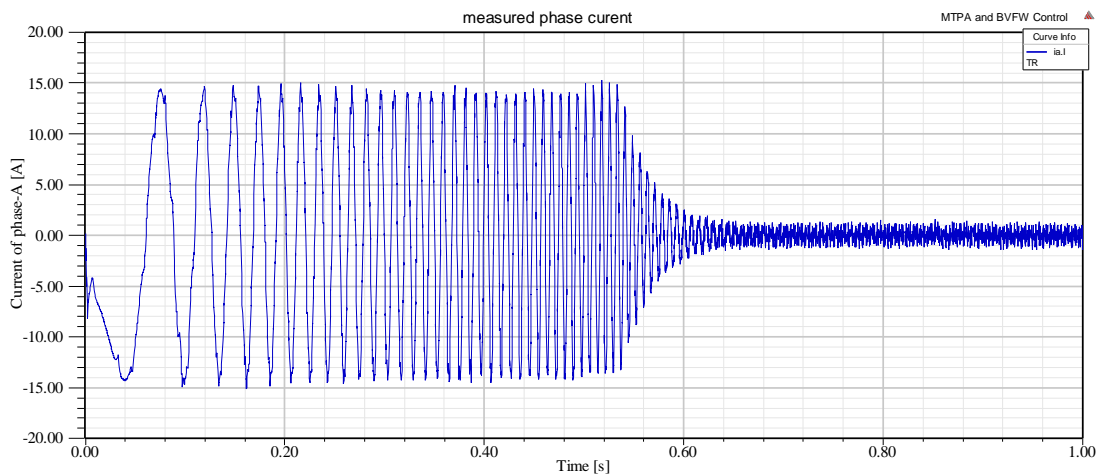
Figure 4.11: Current waveform of phase-a when $\omega_m^* = 300\ rad/s$.
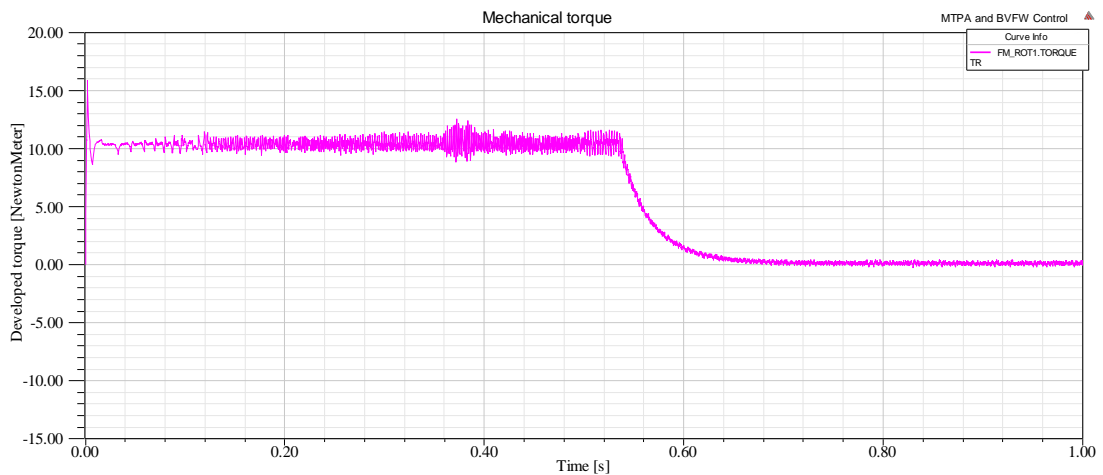
Figure 4.12: Developed torque when $\omega_m^* = 300\ rad/s$.

Figure 4.13 shows the real d- and q- axis current components. Meanwhile, Figure 4.14 depicts the reference current components for d-axis and q-axis. Although there are ripples in the real d- and q- axis current components, the trajectories of the two real current components are consistent with their reference values.
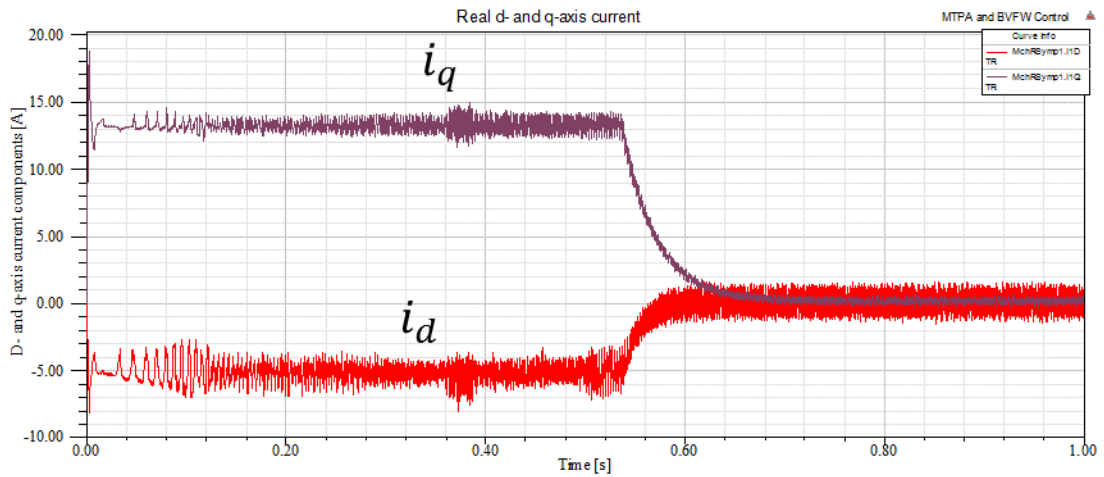
Figure 4.13: Real d- and q- axis current components when $\omega_m^* = 300 \; rad/s$.
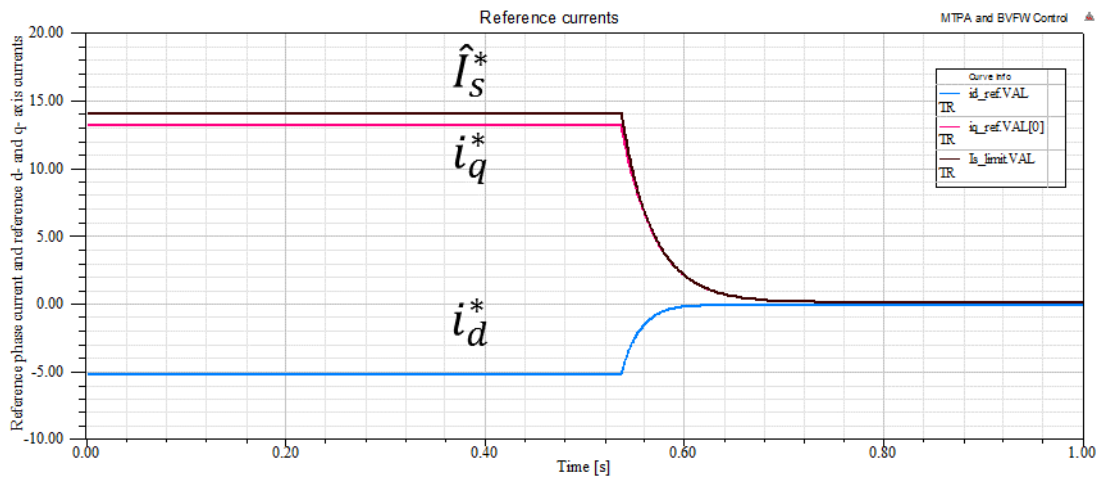
Figure 4.14: The reference phase current (I_{s_limit}), reference d-axis current (i_{d_ref}), and reference q- axis current (i_{q_ref}) when $\omega_m^* = 300 \; rad/s$.

To evaluate the performance of this simulation system in high speeds with the BVFW control, a commanded mechanical speed, which is $\omega_m^* = 700 \; rad/s$, was the

assumed input signal to the control loop as show in Figure 4.9. Here, Figure 4.15 presents the motor's electrical speed versus time. The dashed line represents the base speed of this motor. It is obvious that the motor was operating above base speed. Meanwhile, Figure 4.16 depicts the motor's mechanical speed versus time, which shows that the motor's speed keeps increasing form zero until it reaches a steady state, where $\omega_m = 677.3\ rad/s$. The difference between the reference speed and the real speed is only 3.2%, which shows a reliable controller performance at high speeds. Notice that the original IPM motor described in Table 4.1 is not designed for high speed applications. However, with the help of flux-weakening, such a motor can achieve extended speed range.
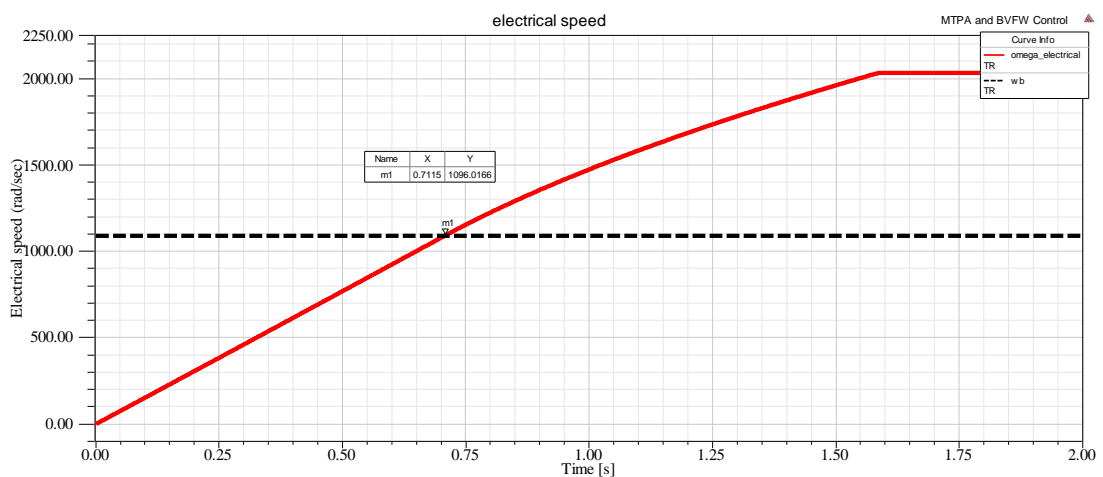
Figure 4.15: Electrical speed versus time when $\omega_m^* = 700\ rad/s$.
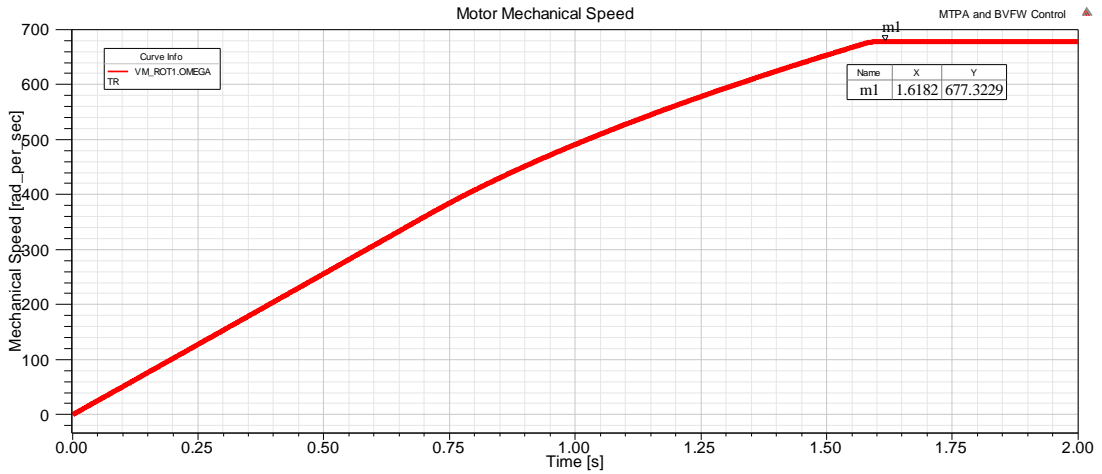
Figure 4.16: Mechanical speed versus time when $\omega_m^* = 700 \ rad/s$.

In Figure 4.17, the real d- and q- axis current components are presented. Compared to the reference d- and q- axis current components shown in Figure 4.18, the current trajectories in Figure 4.17 are consistent with their reference values. It is obvious that the demagnetizing current, i_d, is increasing in the negative direction during the FW region. Meanwhile the q-axis current, i_q is decreasing.
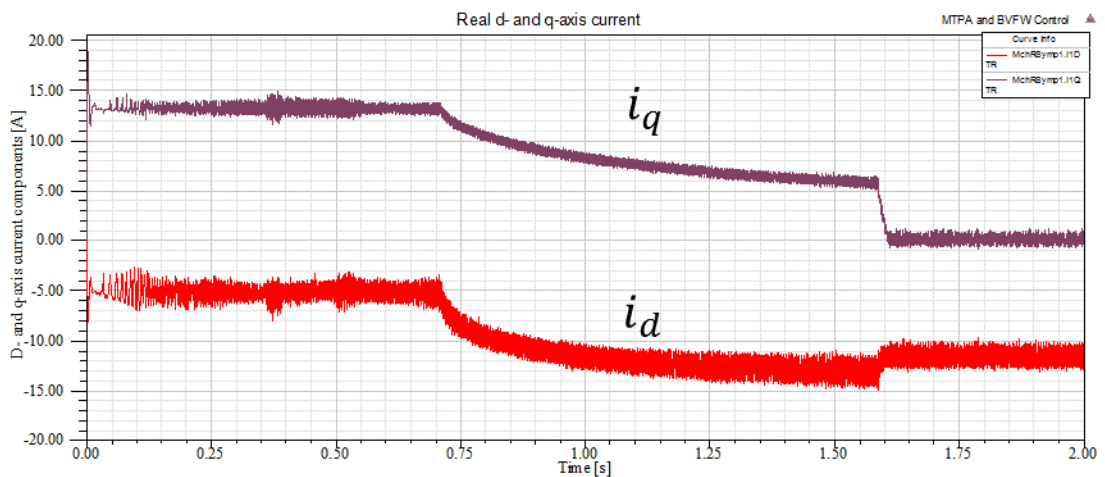
Figure 4.17: Real d- and q- axis current components when $\omega_m^* = 700 \ rad/s$.
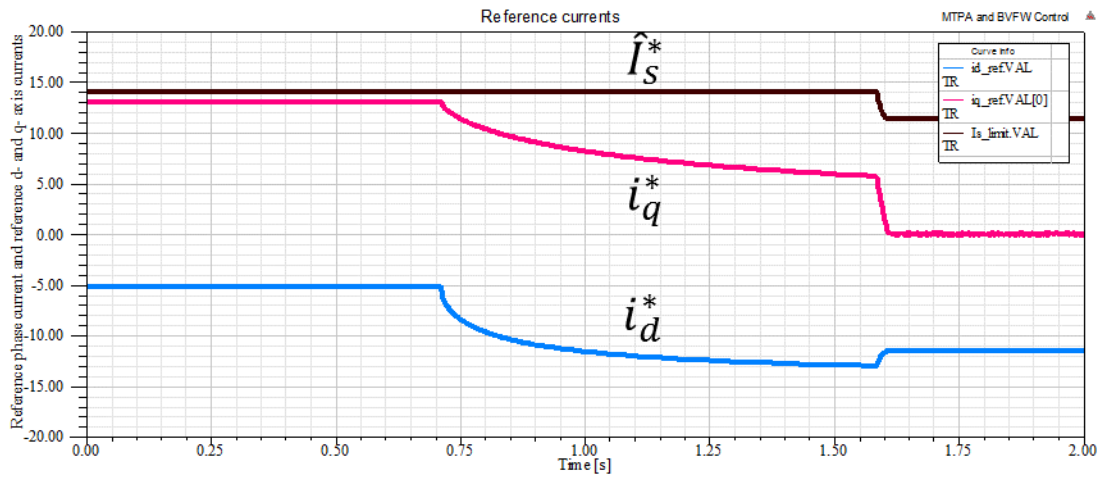
Figure 4.18: The reference phase current (I_{s_limit}), reference d-axis current (i_{d_ref}), and reference q- axis current (i_{q_ref}) hen $\omega_m^* = 700\ rad/s$.

In Figure 4.19, the developed torque during the constant torque region and the constant power region is presented. It is obvious that the developed torque keeps decreasing during the constant power region. Meanwhile, Figure 4.20 shows that the output power is constant during the FW region using the presented BVFW control.
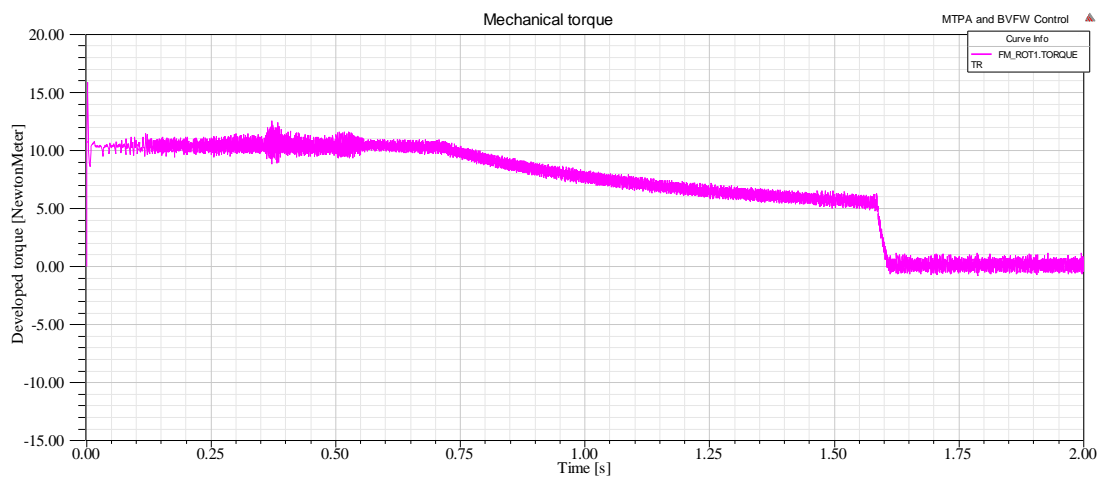
Figure 4.19: Developed torque when $\omega_m^* = 700\ rad/s$.
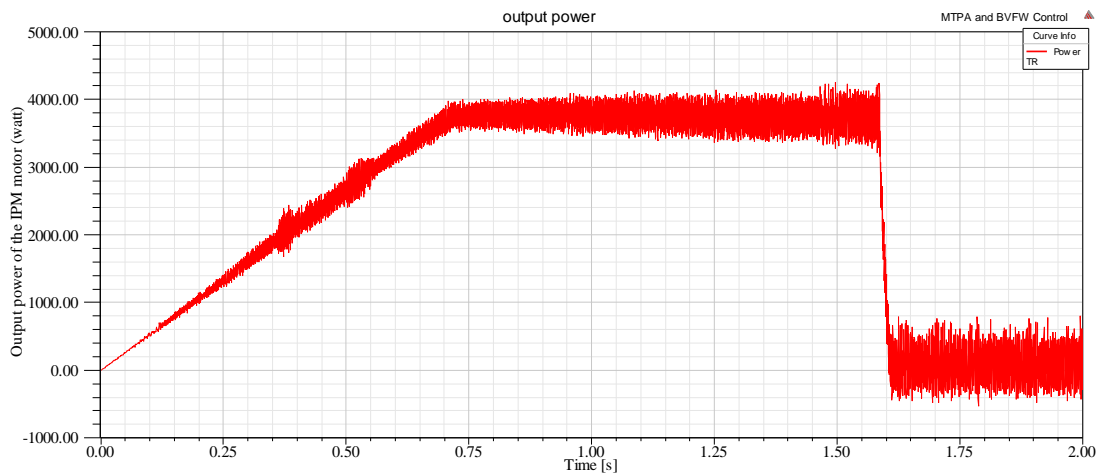
Figure 4.20: Output power when $\omega_m^* = 700\ rad/s$.

From the simulation results presented here, the implemented control system shows reliable performances during the low speed constant torque region and during the high speed constant power region. The error between the motor's final speed and the reference speed is small. Despite some torque ripples, the developed torque remains at a constant value at low speed with the MTPA control. While, the output power is roughly remaining at a constant value during FW region with the BVFW control. From these simulation results, one can arrive at a conclusion that this BVFW control algorithm is a valid flux-weakening control method.

Chapter 5

Summary, Conclusions and Suggested Future Work

5.1 Summary and Conclusions

First, in Chapter 1 of this thesis, a variety of conventional flux-weakening control methods for permanent magnet synchronous motors were reviewed. Then the issue regarding the presence of a high value of back-EMF in the flux-weakening region was discussed. Since the widely used three-phase full-bridge inverter is essentially a buck converter, the idea that utilizes the voltage boost capability of Z-source inverters to obtain better flux-weakening performance becomes very attractive.

Second, in Chapter 2 of this thesis, the mathematical model of permanent magnet synchronous motors is presented. Control algorithms for permanent magnet synchronous motors are presented in this chapter as well. For the operation at low speeds, maximum-torque-per-ampere control was introduced. Meanwhile, for the operation at high speeds, three commonly used flux-weakening algorithms were analyzed, including two methods for SPM motors and one method for both SPM and IPM motors.

Third, in Chapter 3 of this thesis, the Z-source inverter, including its operation principle, passive components design of the Z-impedance network, and three commonly used control methods were introduced. Details of the active state and shoot-through state of Z-source inverters were analyzed in order to have a better understanding of the charging and discharging between inductors and capacitors in the Z-impedance network. Simulation results were presented to verify the voltage boost capability of Z-source inverters in Chapter 3.

In Chapter 4 of this thesis, a special flux-weakening algorithm was developed

for IPM motors driven by Z-source inverters, namely, the boosted-voltage flux-weakening control. Meanwhile, a full speed range control scheme was developed which combined the maximum-torque-per-ampere control at low speeds and the boosted-voltage flux-weakening control at high speeds. Simulation results of a motor-drive system model based on Z-source inverters were presented to verify the validity of the presented flux-weakening control method.

In this thesis, a new approach for flux-weakening control, which is the boosted-voltage flux-weakening control, was developed and simulated. The main contribution of this thesis is in utilizing the voltage boost capability of Z-source inverters to overcome the high value of back-EMF of IPM motors at high speeds. This flux-weakening approach introduced here can further extend the speed range of IPM motors than conventional flux-weakening methods. Moreover, this method can provide high shaft torque at high speeds without increasing the phase currents, which indicates lower motor losses for the same desired torque at high speeds. Meanwhile, a constant output power can be sustained during the flux-weakening region. Simulation results were presented to verify the validity of the new flux-weakening method introduced in this thesis.

5.2 Recommendations for Future Work

Although several developments were presented in this thesis, there are many interesting investigations left for the future work. Some possible subjects are listed as follows:

➢ A prototype of the Z-source inverter can be designed and assembled for many studies, such as the losses on the passive components and semiconductor switches, inverter efficiency, harmonic distortions, voltage boost capabilities, voltage stress on each the components, impacts of different control methods, etc.

Notice that this Z-source inverter should be designed according to a proper IPM motor for possible experiments.

- ➢ With the prototype Z-source inverter and a proper IPM motor, experiments can be conducted to investigate the new flux-weakening method introduced in this thesis. Other significant investigations can be studied based on this motor-drive system, such as new motor control method development, new PWM technique development, efficiency study of the Z-source inverter and the motor at high speeds, control failure at high speeds during flux-weakening operation, etc.

- ➢ The motor model used in the simulations included in this thesis can be replaced with a finite element motor model. Further investigations on motor's efficiencies at different operating points and by different control methods can be conducted. These significant investigations can be used to design optimal motors for full speed range operation and improve control methods for motors.

BIBLIOGRAPHY

[1] Y. Zhang, L. Xu, M. Guven, S. Chi, and M. Illindala, "Experimental verification of deep field weakening operation of a 50-kW IPM machine by using single current regulator," *IEEE Trans. Ind. Appl.*, vol. 47, no. 1, pp. 128-133, 2011.

[2] J. F. Gieras and M. Wing, "Permanent magnet motor technology (Design and Application)," Marcel. Dekker, Inc., second edition, revised and expanded ed., 2002.

[3] S. Chi and L. Xu, "A special flux-weakening control scheme of PMSM - incorporating and adaptive to wide-range speed regulation," *Power Electronics and Motion Control Conference*, vol. 2, pp. 1-6, 2006.

[4] H. Mahmoudi, A. Lagrioui, "Flux-weakening control of permanent magnet synchronous machines," *Journal of Theoretical and Applied Information Technology*, ISSN: 1992-8645, 1992.

[5] L. Harnefors, K. Pietilainen, and L. Gertmar, "Torque-maximizing field-weakening control: design, analysis, and parameter selection," *IEEE Trans. Ind. Electron.*, vol. 48, no. 1, pp. 161-168, February 2001.

[6] N. Bianchi, S. Bolognani, and M. Zigliotto, "High-performance PM synchronous motor drive for an electrical scooter," *IEEE Trans. Ind. Appl.*, vol. 37, no. 5, pp. 1348-1355, Sep./Oct. 2001.

[7] G. Pellegrino, A. Vagati, and P. Guglielmi, "Design tradeoffs between constant power speed range, uncontrolled generator operation, and rated current of IPM motor drives," *IEEE Trans. Ind. Appl.*, vol. 47, no. 5, pp. 1995-2003, Sep./Oct. 2011.

[8] P. Pillay and R. Krisnan, "Modeling, simulation, and analysis of permanent magnet motor drives," *IEEE Trans. Ind. Appl.*, vol. IA-25, pp. 265–279, March/April 1989.

[9] G. Pellegrino, E. Armando, and P. Guglielmi, "Field oriented control of IPM drives for optimal constant power operation," *2007 European Conference on Power Electronics and Applications*, pp.1-10, Sept. 2007.

[10] J. Wai, T. M. Jahns, "A new control technique for achieving wide constant power speed operation with an interior PM alternator machine," *Industry Application Conference*, vol. 2, pp. 807-814, 2001.

[11] K. W. Lee and S. B. Lee, "MTPA operating point tracking control scheme for vector controlled PMSM drives," *International Symposium on Power Electronics Electrical Drives Automation and Motion*, pp. 24-28, June 2010.

[12] T. M. Jahns, "Flux-weakening regime operation of an interior permanent-magnet synchronous motor drive," *IEEE Trans. Ind. Appl.*, vol. IA-23, pp. 681-689, July/Aug. 1987.

[13] Q. Liu, "Analysis, design and control of permanent magnet synchronous motors for wide-speed operation," Ph. D. dissertation, National University of Singapore, 2005.

[14] P. Zhang, "A novel design optimization of a fault-tolerant AC permanent magnet machine-drive system," Ph. D. dissertation, Marquette University, Milwaukee, WI, Dec. 2013.

[15] G. Kohlrusz and D. Fodor, "Comparison of scalar and vector control strategies of induction motors," *Hungarian Journal of Industrial Chemistry*, vol., 39, pp. 265-270, 2011.

[16] C. Capitan, "Torque control in field weakening mode," Master Thesis, Aalborg University, Aalborg, Denmark, June 2009.

[17] H. Le-Huy, "Comparison of field-oriented control and direct torque control for induction motor drives," *Industry Application Conference*, thirty fourth IAS annual meeting, vol. 2, pp. 1245-1252, Oct. 1999.

[18] B. K. Bose, "Modern power electronics and AC drives," Prentice Hall, Inc., 2002.

[19] M.F. Moussa, A. Helal, Y. Gaber, and H.A. Youssef, "Unity power factor control of permanent magnet motor drive system," *12th International Middle-East Power System Conference*, pp 360-367, March 2008.

[20] C. Mademlis, I. Kioskeridis, and N. Margaris, "Optimal efficiency control strategy for interior permanent-magnet synchronous motor drives," *IEEE Transaction on Energy Conversion*, vol. 19, pp. 715-723, Dec. 2004.

[21] W. L. Soong and N. Ertugrul, "Field-weakening performance of interior permanent magnet motors," *IEEE Trans. Ind. Appl.*, vol. 38, no. 5, pp. 1251-1258, Sep. / Oct. 2002.

[22] V. R. Jevremovic and D. P. Marcetic, "Closed-loop flux-weakening for permanent magnet synchronous motors," *4th IET Conference on Power Electronics*, Machines and Drives, pp. 717-721, April 2008.

[23] J. M. Kim and S. K. Sul, "Speed control of interior permanent magnet synchronous motor drive for the flux weakening operation," *IEEE Trans. Ind. Appl.*, vol. 33, no. 1, pp. 43-48, Jan. /Feb. 1997.

[24] S. Morimoto, M. Sanada and Y. Takeda, "Wide-speed operation of interior permanent magnet synchronous motors with high-performance current regulator," *IEEE Trans. Ind. Appl.*, vol. 30, no. 4, pp. 920-926, July/August 1994.

[25] J. R. Hendershot and T.J.E. Miller, "Design of brushless permanent-magnet machines," Motor Design Books LLC, 2010.

[26] F. Giri, "AC electric motors control-advanced design techniques and applications," A John Wiley & Sons, Ltd., 2013.

[27] N. Mohan, "Advanced electric drive," MNPERE, 2001.

[28] B. K. Bose, "A high-performance inverter-fed drive system of an interior permanent magnet synchronous machine," *IEEE Trans. Ind. Appl.*, vol. 24, pp. 987-997, Sept./Oct. 1991.

[29] H. Wen, W. Xiao, H. Li, X. Wen, "Analysis and Minimisation of DC Bus Voltage for Electric Vehicle Applications," *IET Electrical Systems in Transportation*, vol. 2, pp. 68-76, June 2012.

[30] N. Mohan, T. M. Undeland, and W. P. Robbins, "Power Electronics," John Wiley & Sons, Inc., third edition, 2003.

[31] Oak Ridge National Laboratory, "Evaluation of 2004 Toyota Prius Hybrid Electric Drive System," May, 2005.

[32] F. Z. Peng, "Z-Source Inverter," *IEEE Trans. Ind. Appl.*, vol. 39, no. 2, pp. 504-510, March/April 2003.

[33] J. Anderson and F. Z. Peng, "Four Quasi-Z-Source Inverter," *Power Electronics Specialist Conference 2008*, pp. 2743-2749, June 2008.

[34] K. Holland and F. Z. Peng, "Control Strategy for Fuel Cell Vehicle Traction Drive Systems Using the Z-Source Inverter," Vehicle Power and Propulsion, *2005 IEEE Conference*, pp. 639-644, Sept. 2005.

[35] Q. Lei, S. Yang, F. Z. Peng, and R. Inoshita, "Application of Current-fed Quasi-Z-Source Inverter for Traction Drive of Hybrid Electric Vehicles," *Vehicle Power and Propulsion Conference*, pp. 754-760, Sept. 2009.

[36] F. Z. Peng, A. Joseph, J. Wang, M. Shen, L. Chen, Z. Pan, E. O. Rivera, and Y. Huang, "Z-Source Inverter for Motor Drives," *IEEE Trans. on Power Electron*, vol. 20, no. 4, pp. 857-863, July 2005.

[37] F. Z. Peng, X. Yuan, X. Fang and Z. Qian, "Z-Source Inverter for Adjustable Speed Drives," *IEEE Power Electronics Letters*, vol. 1 no. 2, pp. 33-35, June 2003.

[38] F. Gao, P. C. Loh, F. Blaabjerg and D. M. Vilathgamuwa, "Performance evaluation of three level Z-source inverters under semiconductor-failure conditions," *IEEE Trans. Ind. Appl.*, vol. 45, no. 3, pp. 971-981, May/ Jun. 2009.

[39] B. Ge, Q. Lei, W. Qian and F. Z. Peng, "A family of Z-source matrix converters," *IEEE Transactions on Industrial Electronics*, vol. 59, no. 1, pp.35-46, Jan. 2003.

[40] Y. Tang, S. Xie, C. Zhang, and Z. Xu, "Improved Z-source inverter with reduced Z-source capacitor voltage stress and soft-start capability", *IEEE Trans. on Power Electron.*, vol. 24, no. 2, pp. 409-415, Feb. 2009.

[41] M. Zhu, K. Yu, and F.L. Luo, "Switched inductor Z-source inverter", *IEEE Trans. on Power Electron.*, vol. 25, no. 8, pp. 2150-2158, Aug. 201

[42] F.Z. Peng, M. Shen, and Z. Qian, "Maximum boost control of the Z-source inverter", *IEEE Trans. on Power Electron.*, vol. 20, no. 4, pp. 833-838, Jul. 2005.

[43] M. Shen, J. Wang, A. Joseph, F.Z. Peng, L.M. Tolbert, and D.J. Adams, "Maximum constant boost control of the Z-source inverter," *IEEE Trans. Ind. Appl.*, vol. 42, no. 3, pp. 770-777, May/Jun. 2006.

[44] Q. Lei, D. Cao, and F. Z. Peng, "Novel loss and harmonic minimized vector modulation for a current-fed quasi-Z-source inverter in HEV motor drive application," *IEEE Trans. on Power Electron.*, vol. 29, no. 3, pp. 1344-1357, Mar. 2014.

[45] A. M. El-Refaie and T. M. Jahns, "Optimal flux weakening in surface PM machines using fractional-slot concentrated windings," *IEEE Trans. Ind. Appl.*, vol. 41, no. 3, pp. 790-800, May/Jun. 2005.

[46] A. Tessarolo, M. Mezzarobba, and R. Menis, "A novel interior permanent magnet motor design with a self-activated flux-weakening device for automotive applications," *2012 International Conference on Electrical Machines*, pp. 2603-2609, Sept. 2012.

[47] R. H. Park, "Two-reaction theory of synchronous machines. Generalized method analysis, part I and part II," *Transactions of the American Institute of Electrical Engineers*, vol. 48, pp. 716-730, 1929.

[48] M. E. Haque, L. Zhong, and M. F. Rahman, "Improved trajectory control for an interior permanent magnet synchronous motor drive with extended operating limit," *Journal of Electrical & Electronics Engineering, Australia*, vol. 22, no. 1, 2003.

[49] Z. Mihailovic, "Modeling and control design of VSI-fed PMSM drive system with active load," Master Thesis, Virginia Polytechnic Institute and State University, Blacksburg, Virginia, Jun. 1998.

[50] I. Boldea and S. A. Nasar, "Electric drives," CRC Press Inc., 1999.

[51] D. W. Novotny and T. A. Lipo, "Vector control and dynamics of ac drives," Oxford University Press Inc., 1996.

[52] M. Zelechowski, "Space vector modulated-direct torque controlled (DTC-SVM) inverter-fed induction motor drive," Ph.D. Dissertation, Warsaw University of Technology, 2005.

[53] M. Yano, S. Abe, and E. Ohno, "History of power electronics for motor drives in Japan," *IEEE Conference on the History of Electronics*, Buckinghamshire, U.K., 2004, pp. 1–11.

[54] M. Li, J. He, and N.A.O. Demerdash, "A flux-weakening control approach for interior permanent magnet synchronous motors based on Z-source inverters," *IEEE Transportation Electrification Conference and Expo (ITEC)*, pp. 1-6, Jun. 2014.

[55] Oka Ridge National Laboratory, "Z-source inverter for fuel cell vehicles," Sept. 2005.

[56] Oka Ridge National Laboratory, "Oak ridge national laboratory annual progress report for the power electronics and electric machinery program," Oct. 2011.

[57] B. Ge, Q. Lei, W. Qian, and F. Z. Peng, "A family of Z-source matrix converters," *IEEE Trans. Ind. Electron.*, vol. 59, no. 1, pp. 35-46, Jan. 2012.

[58] X. Liu, P. C. Loh, P. Wang, and X. Han, "Improved modulation schemes for indirect Z-source matrix converter with sinusoidal input and output waveforms," *IEEE Trans. Power. Electron.*, vol. 27, no. 9, pp. 4039-4050, Sep. 2012.

[59] Y. Zhou, L. Liu and H. Li, "A high-performance photovoltaic module-integrated converter based on cascaded quasi-Z-source inverter using eGaN FETs," *IEEE Trans. Power. Electron.*, vol. 28, no. 6, pp. 2727-2738, Jun. 2013.

[60] F. Gao, P. C. Loh, F. Blaabjerg, and D. M. Vilathgamuwa, "Performance evaluation of three-level Z-source inverters under semiconductor-failure conditions," *IEEE Trans. Ind. Appl.*, vol. 45, no. 3, pp. 971-981, May/Jun. 2009.

[61] Y. Xie, Z. Qian, X. Ding, and F. Peng, " A novel buck-boost Z-source rectifier," *IEEE Power Electronics Specialists Conference*, pp. 1-5, 2006.

[62] X. Ding, Z. Qian, Y. Xie, and Z. Lu, "Three phase Z-source rectifier," *IEEE Power Electronics Specialists Conference*, pp. 494-500, 2005.

[63] Y. Li, J. Anderson, F. Peng, and D. Liu, "Quasi-Z-source inverter for photovoltaic power generation systems," *IEEE Applied Power Electronics Conference and Exposition*, pp. 918-924, 2009.

[64] G. L. Calzo, A. Lidozzi, L. Solero, and F. Crescimbini, "Three-phase Z-source power supply design," *IET Power Electronics*, vol. 5, pp. 1270-1281, Nov. 2012.

[65] I. Roasto, D. Vinnikov, T. Jalakas, J. Zakis and S. Ott, "Experimental study of shoot-through control methods for qZSI-based dc/dc converters," *IEEE International Symposium on Power Electronics Electrical Drives Automation and Motion*, pp. 29-34, Jun. 2010.

[66] S. Rajakaruna and L. Jayawickrama, "Steady-state analysis and design impedance network of Z-source inverters," *IEEE Trans. Ind. Electron.*, vol. 57, no. 7, pp.2483-2491, Jul. 2010.

[67] S. Bolognani, S. Calligaro, R. Petrella, and F. Pogni, "Flux-weakening in IPM motor drives: comparison of state-of-art algorithms and a novel proposal for controller design," *Proceeding of the 2011-14th European Conference on Power Electronics and Applications*, pp. 1-11, 2011.

Appendix I

General Formula for Solving Quartic Equations

A quartic equation can be written in a general form as follows:

$$ax^4 + bx^3 + cx^2 + dx + e = 0 \tag{1}$$

Assuming $a \neq 0$, the general formula for roots can be written as follows:

$$x_1 = -b/4a - S + \frac{1}{2}\sqrt{-4S^2 - 2p + q/S} \tag{2}$$

$$x_2 = -b/4a - S - \frac{1}{2}\sqrt{-4S^2 - 2p + q/S} \tag{3}$$

$$x_3 = -b/4a + S + \frac{1}{2}\sqrt{-4S^2 - 2p - q/S} \tag{4}$$

$$x_4 = -b/4a + S - \frac{1}{2}\sqrt{-4S^2 - 2p - q/S} \tag{5}$$

where,

$$p = (8ac - 3b^2)/8a^2 \tag{6}$$

$$q = (b^3 - 4abc + 8a^2d)/8a^3 \tag{7}$$

$$S = \frac{1}{2}\sqrt{-\frac{2p}{3} + \frac{(Q + \Delta_0/Q)}{3a}} \tag{8}$$

In (8), the variable, Q, can be written as follows:

$$Q = \sqrt[3]{\frac{\left(\Delta_1 + \sqrt{\Delta_1^2 - 4\Delta_0^3}\right)}{2}} \tag{9}$$

where,

$$\Delta_0 = c^2 - 3bd + 12ae \tag{10}$$

$$\Delta_1 = 2c^3 - 9bcd + 27b^2e + 27ad^2 - 72ace \tag{11}$$